Investigation of Hot cracking behaviour based on thermo-mechanical aspects of Laser spot welded Advanced High strength steels

By

Aman Dixit

in partial fulfilment of the requirements for the degree of

Master of Science
in Material Science and Engineering

at the Delft University of Technology,
to be defended publicly on Friday September 28, 2018.

Supervisor:	Prof. dr. Marcel Hermans	
Thesis committee:	Prof. dr. Ian Richardson	TU Delft

To ma, papa and Suman

Acknowledgement

The master program at Delft University of Technology was an excellent opportunity to graft a career in the materials' world. I am giving my gratitude to all the people responsible to make sure I churn out the best in me for my final graduation project. Firstly, a big thank you to Professor Marcel Hermans (TU Delft) for this excellent opportunity of master thesis and being my personal supervisor right from the beginning. I have learnt a lot from professor and would remember all his teachings throughout my life. I couldn't miss out Mr. Gautam Agarwal for his immense support (both professional and personal). Thank you, Gautam Bhaiya, for being my guide.

I would also like to thank Mr. Jurriaan Van Slingerland and Mr. Remko Seijffers as they provided me with all their expertise and working knowledge for Laser welding and DIC mechanism. Besides, the social interaction with them was lively and quite interesting.

A special thanks to the Mr. Sander Van Asperen from for his support for all technical instructions for characterization of the welded samples.

To all the people in Material Sc. and Engineering, it was a huge learning experience and also a social platform for great interactions. I thank you all deeply from my heart for this two year experience.

Abstract

The mechanical properties of advanced high strength steels (AHSS) for automotive applications are sensitive to their multi-phase microstructures, which are carefully designed and produced by selection of the composition and production route. A combination of alloying elements and complex heat treatment generates microstructures with designed fractions, dimensions, compositions, morphologies and spatial distribution of phases. However, the high alloying content, required to stabilize the multi-phase microstructure of these steels, makes the material sensitive to hot cracking/solidification cracking. Hot cracking of laser welded components is a serious problem that is often reported by automotive manufacturers using AHSS. The increasing use of thinner gauge steels in order to reduce the weight of the automobile demands the application of laser welding at the edge of the steel flanges, which often leads to severe cracking. During the commercial steel making process, laser welding is applied to join steel coils. Therefore, in several industrial processes for advanced high strength steels, hot cracking can lead to serious disturbances, down time and production loss.

An experimental study was performed for the graduation project based exclusively on thermo-mechanical aspects. External tensile loading was applied during lase spot welding to relate the stress and strain based models designed specifically for hot cracking. In situ strain measurements were extracted, using digital imaging correlation (DIC). All the laser welds were made using Nd:YAG laser. The experimental study focused majorly on single pulsed spot welds with few bead-on-plate welds for comparison. Only two kinds of AHSS were investigated namely, Dual phase (DP) steels and Transformation induced plasticity (TRIP) steels, due to their high demands for laser weld automotive applications. The project includes welding with external tensile loading by using a modified version of controlled tensile weldability test (CTW) and characterization of welds to study hot cracking behaviour based on thermo-mechanical aspects. A 2-D finite element model was made by the modeling software, COMSOL multiphysics to depict the temperature profile.

Keywords: Nd:YAG laser welding, Dual phase and Transformation induced plasticity steels, Single pulsed laser spot welds, Hot cracking/weld solidification cracking, Thermal modeling, DIC measurements

Table of Contents

Chapter 1 Introduction

The use of laser welding in automotive manufacturing has increased dramatically over recent years. About 17% of all market revenue in lasers is generated in industrial production for welding [1]. Although, the lasers are preferred mainly for cutting applications, a significant and growing proportion of lasers are being applied to welding (figure 1). There has been an explosion of growth in welding applications, particularly involving steel manufacturers, for welded blank manufacture and in body-in-white welding applications. Laser welded blanks are composed of two or more sheets of similar or dissimilar materials, thicknesses and/or coating types welded together, which are formed to fabricate three-dimensional automotive body parts as seen in figure 2 [1]. Other applications of laser in the manufacture of components include engine parts, transmission parts, alternators, solenoids, fuel injectors, fuel filters, air conditioning equipment and air bags [1] [3].

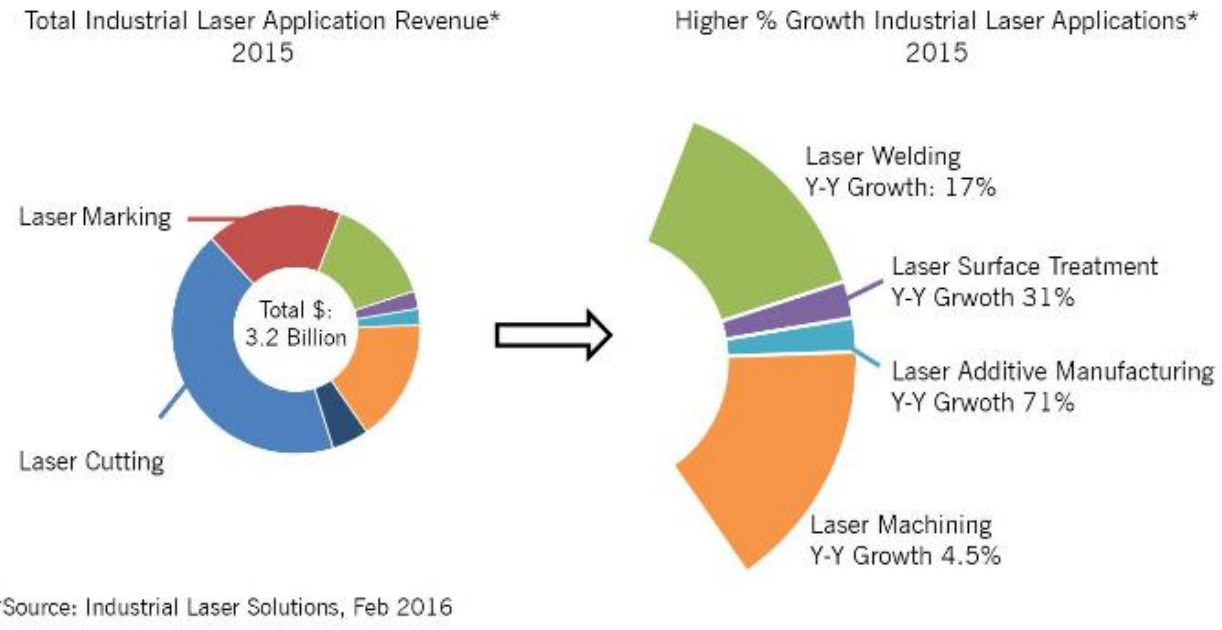

Figure 1 Representation of revenue generated by laser applications in 2015 [1]

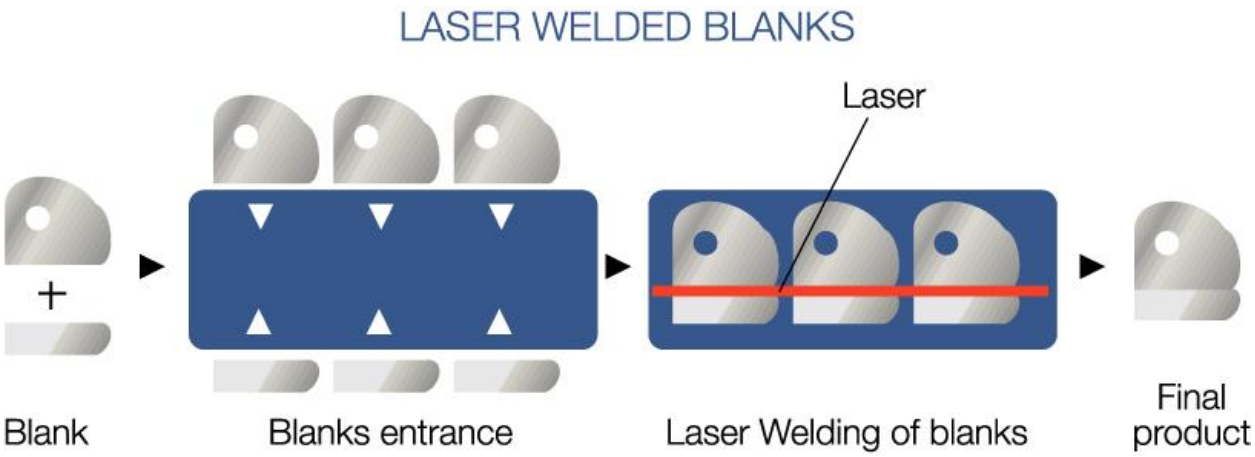

Figure 2 Schematic representation of manufacturing of laser welded blanks [2]

Potential benefits realised by the application of laser welding include reduced flange widths, increased structural strength and high speed automated processing. High welding speeds are achieved in laser welding along with high power density, which significantly increases the production rate. The combination of high power density and speed minimizes metallurgical heterogeneities at the fusion zone or heat-affected zone (HAZ). Lower heat input also reduces the thermal distortion of the work pieces, minimizing the machining requirements after welding [3].

1.1. Challenges faced by automakers

Over the last decade, automobile industries have faced other challenges regarding material selection [4]. The requirements of passenger safety, vehicle performance and fuel economy are the essential aspects while curbing those challenges. There is a strong competition between steel and low density metal industries [4]. Other requirements which have to be met include fuel efficiency, environmentalism, manufacturability, durability and quality. In this highly competitive automotive industry, cost is also extremely important in material selection. As the motivation to reduce the mass of the vehicles continues to intensify, automakers seek to maximize the efficiency of their material selection.

As noted in an article published in the New York Times in 1909 about American auto steel, automakers deduced that the secret is “to put the right steel in the right place” [4]. As new priorities emerged, such as decreased cost, and weight reduction for efficiency, so did the demand for new materials, including new steels. More projects followed to demonstrate and

communicate the capability of steel to meet the demands for increased safety and fuel efficiency through light weight vehicle structures [4]. In recent years the use of advanced high-strength steel (AHSS) has increased in popularity in the automotive industry because of its excellent combination of high strength and ductility. Automakers can conveniently tailor the design of automotive parts through the combination of strength, formability and crashworthiness by incorporating AHSS in laser welded blanks [2].

Although, laser welding exhibit several advantages over conventional fusion welding processes, laser welds in structural steels can contain defects. Without proper preparation of materials and selection of welding parameters, certain defects can be more likely. One such defect is the weld solidification cracking during the laser welding process.

Weld solidification cracking is refer to the formation of shrinkage cracks during the solidification of weld metal leading to rupture of liquid films present at grain boundaries in the mushy zone trailing the weld pool. During the solidification process, the thermally induced deformation due to solidification shrinkage from phase transition and thermal contraction from temperature change would induce excessive strain/stress in the mushy zone and open up connected dendrite arms. Solidification cracking occurs if an insufficient amount of liquid flows back to the opened gap [9].

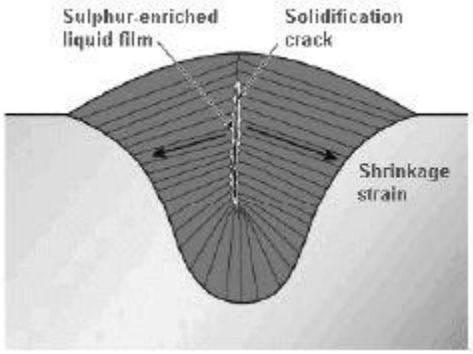

Figure 3 Schematic representation of solidification crack in a weld pool [9]

The cracks formed at the solidification boundaries are characteristically inter-dendritic or inter-granular. The morphology reflects the weld solidification structure and there may be evidence of segregation associated with the solidification boundary. Because of the nature of the mushy zone and complex interactions of the mechanisms, the prediction of solidification cracks is a complicated subject [9].

1.2. Outline of the thesis

Of all AHSS, only dual phase (DP) steel and transformation induced plasticity (TRIP) steel have been identified as potential candidates for car body fabrication because of their better formability compared with martensitic steel and their low manufacturing cost compared with other AHSS [4] [5]. As mentioned, laser welding on the commercially viable steels might induce solidification cracking. This phenomenon serves the motivation for the current graduation thesis. Based on the results achieved from the preliminary investigation, a systematic study was conducted to reveal the mechanisms leading to possible solidification crack formation.

Solidification cracking requires a complete understanding of various factors' interaction which affects cracking susceptibility. The topic itself, as it applies to weldability has for many years been a highly contentious subject, particularly with regard to defining its initiation cause. This is due in large part to its complex nature, involving interplay between thermal, mechanical, and metallurgical components. Although considerable advances in understanding hot cracking mechanisms have been made, most of the known influencing factors are metallurgical in character. The thermo-mechanical effects comparatively are less considered or quantified. Presently, there exist numerous hot cracking tests that were however conceived for welding methods in the application of laser welding.

The master graduation report explains the work carried out thus far based on thermo mechanical aspect of the hot cracking phenomena due to laser welding on DP and TRIP steels. The project aims at providing experimental study based on solidification cracking on laser spot welds addressing the following chapters

- Following chapter 1, chapter 2 details out the literature survey conducted on the methodology of laser welding, summary on advanced high strength steels (focusing on DP and TRIP steels) and available theory behind weld solidification cracking.
- Chapter 3 describes the experimental procedure conducted by using laser beam welding. For this project, laser spot welding was conducted as the major welding procedure. Few bead-on-plate welds were also made for a comparison based study which will be described in the chapter 4.
- As the study is based on thermo-mechanical aspect in solidification cracking, the experiments are based on a modified version of controlled tensile weldability test procedure. In other words, the study is primarily focused on solidification cracking behavior due to imposed tensile loads on the specimen during a weld thermal cycle.
- Experimental results are described in chapter 4 presenting the outcome after welding.
- Chapter 5 gives a detailed discussion on the possible reasons explaining results.

Chapter 2 Literature survey

The current literature survey focuses on three aspects in order, namely Laser beam welding, advanced high-strength steels and weld solidification cracking in the fusion zone. A short description of liquation cracking in the heat affected zone is also presented in this chapter. However, liquation cracking has a different nature and was not observed in the entire set of experiments.

2.1. Laser Beam welding

The heating source, which melts the metal in fusion welding processes, can either be an arc, plasma, laser beam, electron beam or a combination of them. The transient temperature in and around the weld pool is greatly governed by the distribution of the energy from these heat sources. It is therefore necessary to properly represent such a heat source. As the physics to represent arc, laser beam, electron beam or plasma beam is often complex, thermal modeling of welding heat sources has been developed [4] [5].

Laser welding, because of the advancement over the years, constitutes an important operation among the joining processes [4]. Figure 4 shows the top view of the schematic set-up for laser welding without a filler rod. The focused laser beam is made to irradiate the work piece or joint at the given power and speed. A shroud gas such as Argon, protects the weld pool from undue oxidation. Laser heating fuses the work piece or plate edges and joins once the beam has passed. In case of welding with filler, melting is primarily confined to the feeding wire tip while a part of the substrate being irradiated melts to insure a smooth joint. In either case, the work piece or the beam travels at a rate suitable for welding and maintaining a minimum heat affected zone.

The energy required to melt the material depends on the physical properties of the material (absorption coefficient, heat conduction), the wavelength of the laser light and the properties of the surface of the workpiece. Usually materials with higher thermal conductivity produce welds with deep, narrow weld profiles, a small HAZ and little distortion [5]. As a result of the better energy utilisation and larger depth to width ratios of welds attainable with deep penetration welding, this is the prime method of welding used in industry with the conventional laser sources [5].

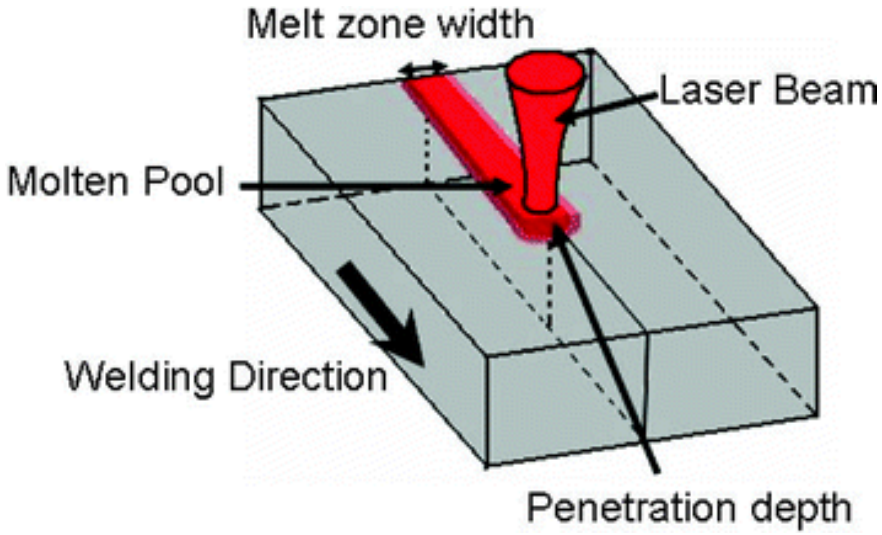

Figure 4 Top view of the schematic set-up for laser welding [4]

2.2. Modes of laser welding

There are two fundamental modes of laser welding depending on the beam power/configuration and its focus with respect to the work piece [4]

- conduction welding
- keyhole or penetration welding

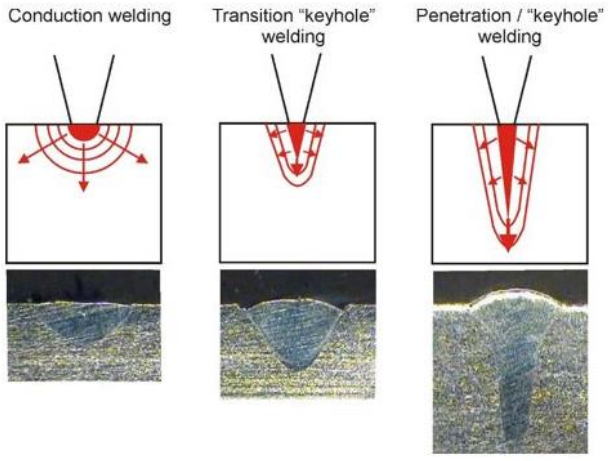

Figure 5 Schematic representation of modes of laser welding [4]

Conduction limited welding occurs when both the beam is out of focus and power density is low/insufficient to cause boiling at the given welding speed as shown in figure 5. In deep penetration or keyhole welding, there is sufficient energy/unit length to cause recoil force and hence, a hole forms in the melt pool. The 'keyhole' behaves like an optical black body. The radiation enters the hole and is subjected to multiple reflections before being able to escape. The transition from conduction mode to deep penetration mode occurs with increase in laser intensity and duration of laser pulse applied to the work piece [4] [5].

2.2.1. Conduction Welding

Laser conduction welding is performed at low energy density, typically around 0.5 MW/cm^2, forming a weld pool shape that is shallow and wide. It also results in narrow heat affected zone and minimum thermal distortion. The heat to create the weld in the material occurs by conduction from the surface. Typically this can be used for applications that require an aesthetic weld and when particulates are a concern, such as certain battery sealing applications [5].

Conduction laser welding shows several advantages. This welding process can be a viable alternative to keyhole laser and to arc welding. It is a stable process which allows good control of the heat delivered to the work-piece. The use of large beams in this mode reduces fit-up problems and the laser system used does not require a high beam quality. One of the disadvantages attributed to conduction mode welding was that the penetration depth of the welds was small, around 2 mm [5].

2.2.2. Key-hole formation

Increasing the power density beyond around 1.5 MW/cm^2 shifts the weld to keyhole mode, which is characterized by deep narrow welds with an aspect ratio greater than 1.5 (weld width to depth of penetration). Figure 6 a shows how increasing the peak power density beyond a certain value of power density moves the weld from conduction to penetration or keyhole welding [5].

In this keyhole welding mode the weld can be completed at either very high speeds in excess of 35 cm/s with shallow key-hole welds, or very deep welds for speed as low as 0.8 cm/s. The high power density laser light forms a filament of vaporized material, known as a keyhole, which

extends into the material and provides a conduit for the laser light to be efficiently delivered into the material as shown in figure 6 b. This direct delivery of energy into the material maximizes weld depth and minimizes the heat into the material, reducing the heat affected zone and part distortion. This type of welding is used in the manufacture of many automotive power train components such as gearboxes and torque converters and also in high speed battery tab welding.

The keyhole is surrounded by molten material that acts to close the keyhole. Under steady state and optimized welding conditions, the vapor pressure contained within the keyhole effectively prevents the molten material from permanently collapsing which would stop the instable welds. However, local and short time period collapses of the keyhole may occur even during optimized welding condition.

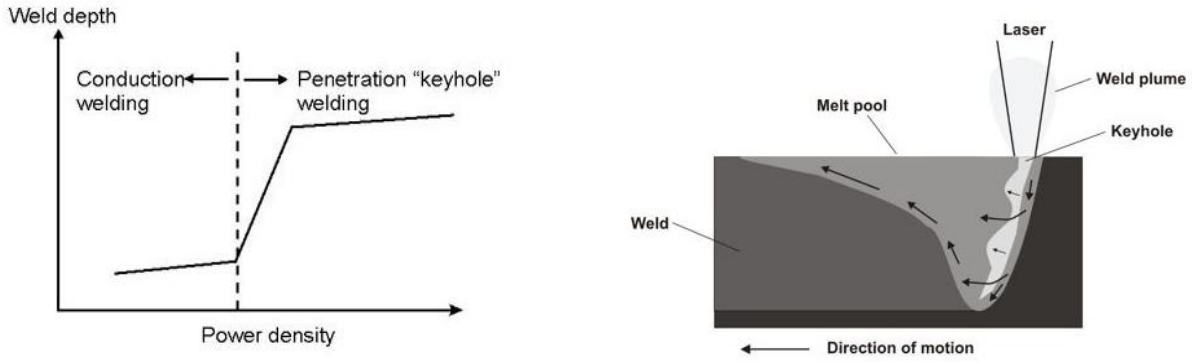

(a) (b)

Figure 6 (a) Weld depth vs power density (representation of transition of the modes of welding) (b) Schematic representation of keyhole penetration [5] [6]

2.3. Commercial Lasers for structural fabrication

There are two main types of industrial laser of interest for structural fabrication namely carbon dioxide (CO_2) lasers and neodymium-yttrium–aluminium–garnet fibre lasers (Nd:YAG). Traditional CO_2 lasers have been predominately used in industry when compared with solid-state Nd:YAG lasers. Low power Nd:YAG lasers are extensively used in the electronics industry. Rapid improvements in technology mean that diode lasers of sufficiently high power and power density for the production of good deep penetration welds are now possible. All the

experiments for this project were conducted using the Nd:YAG laser as the source which has an operating wavelength of 1.06 µm.

Most of the commercially available Nd:YAG lasers have average powers of several hundred Watts with peak powers 1-10 kW. Metals exhibit a higher surface absorptivity at this lower wavelength [6]. Their overall efficiency is about 3-5%. Unlike CO_2 lasers, the beam can be guided through flexible glass fibres, due to its smaller wavelength. This makes it attractive for 3-dimensional operations combined with articulated arm type robots, providing greater flexibility, accessibility and lower costs. In comparison, CO_2 lasers have to use a complicated mirror system. The optical lenses and fibre optics provide a source of well-defined size and angular radiating cone, with an even energy distribution. Mechanical or electro-optical deflectors can be used to deflect or multiplex a beam to several locations; dielectric beam splitters allow the energy to be split for simultaneous action; all in combination with the use of optical fibres for relaying the laser beam to the place of work. Simultaneous spot welding by Nd:YAG lasers has found wide use in the electronics industry as it is highly efficient and has the inherent advantage of minimising distortion and stress in the finished product [6]. It is also possible to shape the temporal power profile of each pulse at pulse repetition rates of up to several kHz [6]

2.4. Optical Properties

The optical properties of the material, the wavelength of the laser light and the surface roughness of the workpiece are the main factors which determine the energy fraction of the beam which is absorbed and penetrates to a thickness generally defined as the optical penetration depth. A high optical absorption coefficient at the operating wavelength of the laser greatly enhances this process. The operating wavelength, however, is a fixed quantity determined by the choice of laser source.

In the case of Nd:YAG lasers, the absorptivity of many materials is low at the wavelength of 1.06 µm, resulting in very low energy efficiencies for these welding systems (typically 1-3%) [7]. The absorption of the laser beam by the workpiece is also affected by the surface condition of the material. Optically rough surfaces cause less specular reflection of the beam and more readily absorb the light energy. In deep penetration welding, the formation of a 'keyhole' also enhances the coupling between the incident laser light and the material, as multiple reflections of the scattered light occur within the confined space of the keyhole [7]. This process greatly increases the amount of light absorbed.

2.5. Energy Transfer Efficiency and Melting Efficiency

The absorption of the laser beam energy by the weldment is strongly dependent on the laser power and the position of the focused laser beam. Two parameters have been used as a measure of the efficient use of the laser power in the production of a weld. They are the energy transfer efficiency and the melting efficiency. The energy for melting consists of two components namely heat of fusion and heat required (specific heat capacity, C_P) for the temperature rise. The process efficiency is known to depend on the laser beam power density (power and focus), heat losses (conduction, convection, radiation) and reflection. The melting efficiency is affected by laser output power and travel speed.

Measurements of the efficiencies have been made by Fuerschbach for bead-on-plate welds (partial penetration) in relatively thick plates of 304 stainless steel, 1018 low-carbon steel and pure tin using a continuous power CO_2 laser beam and Argon shielding gas [7].

2.6. Laser spot welding

Laser beam welding has a number of desirable attributes. The heat affected zones are characteristically smaller and narrower than those produced using conventional welding techniques and distortion of the work piece is reduced. The processes are also suitable for the welding of heat sensitive materials and, with appropriate selection of operating parameters (the same heat source can be used for both welding and cutting). As the mechanical properties of a weld (obtained from microstructures) are highly dependent on the cooling rate of the weld metal, knowledge of the temperature field in and around the melt pool is essential for the understanding and modeling of the welding process [8][9].

During laser spot welding, an intense beam is focused onto a small area. The material under the beam rapidly melts and may partly vaporise, leaving behind a small vapour filled crater, which enhances the absorptivity of the incident beam. As mentioned, this vapour filled crater is referred to as a ‘keyhole’. The molten front extends more in the thickness than in the width direction if the laser power is sufficiently high. This can lead to a parallel sided molten pool and heat transfer occurs via radiative and convective modes through the vapour and molten material.

2.6.1. Background

Rosenthal, Swift-Hook and Gick analytically modeled continuous laser welding assuming heat transfer due to conduction [10][11][12][18]. The beam was represented as a moving line source with full penetration under all welding conditions. They were able to estimate the weld dimensions as a function of laser power and beam velocity relative to the work-piece. Any deviation in results was explained attributing the definition of the heat source and the failure to account for the convective heat flow. Andrews and Atthey reported a three-dimensional heat transfer model, which assumed total absorption of power by the material as soon as the laser beam impinges on the work-piece [18]. The keyhole dimensions were calculated considering convective flow in the weld pool to be driven by surface tension and gravity. The only discrepancy in their case was the assumption regarding total absorption of the laser power. Kaplan calculated the keyhole profile using a point by point determination of the energy balance along the keyhole wall, locally solving the energy balance equation and representing the laser as a line heat source [18]. The parameters involved in the mentioned theories are summarized in the appendix.

It is necessary to consider how the variations for spot welding can be accommodated in the analysis and to examine how a heat flux distribution can cater for both conduction and combined convection and conduction modes of heat transfer. Goldak et al. initiated the concept of a volumetric heat source in the context of moving arc welding that permitted the energy to reach inside the weld pool volume and defining a pseudo weld pool in the form of a double ellipsoid as shown in figure 7 [18]. The double ellipsoid heat source was defined by parameters a, b, c_1 for representing front of the ellipsoid, whereas the rear ellipsoid was defined by parameter a, b and c_2.

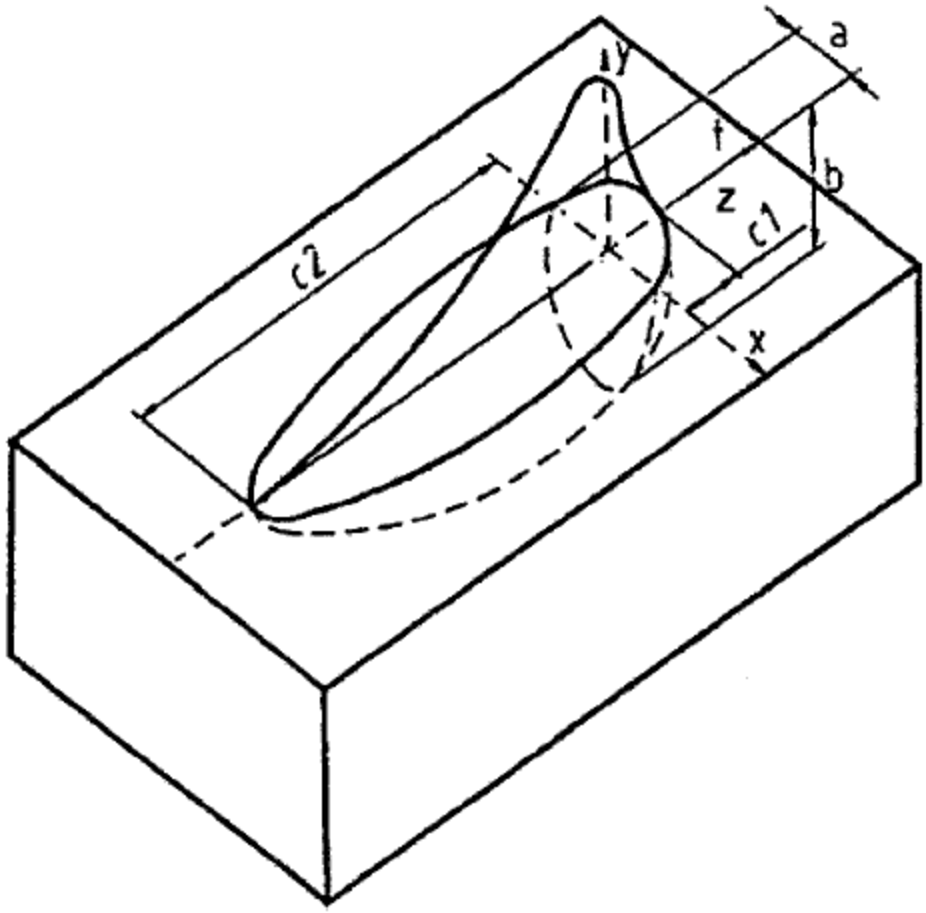

Figure 7 Double ellipsoidal model representation [18]

The power density distribution in the front and rear quadrant of weld pool was given as

$$q(x.y.z.t) = \frac{6\sqrt{3}Q}{abc_{1.2}\pi\sqrt{\pi}}\exp(-3\frac{x^2}{a^2})\exp(-3\frac{x^2}{b^2})\exp(-3\frac{(z-v(\tau-t))^2}{a^2}) \quad (1)$$

where Q is the power of the heat source (i.e. welding arc, laser beam, electron beam, etc.), 2a represents the weld bead width, b is the penetration, v is the welding speed, c_1 and c_2 represent the extent of the heat source from its centre towards the front and rear of the source respectively and τ is defined as a time factor such that t=0 and $v\tau$ is the distance between the heat source and the point of interest. This leads to a typical heat source that is a combination of two half ellipsoids – one in advance of the centre of the heat source and the other at the rear.

The intensity of the source is distributed in a Gaussian manner within each half ellipsoid. The double ellipsoidal representation thus manifests a volumetric heat source and also considers the fact that for relative motion between the heat source and the material, there will be an

asymmetry in the magnitude of the heat input between the front section and the rear section of the centre of the heat source. The only limitation of this representation is that it requires a prior knowledge of the pool shape, i.e. parameters a, b, c_1, and c_2.

Frewin and Scott proposed a three-dimensional finite element analysis for pulsed laser welding. From experiments they found the heat flux distribution to be conical [15]. The measured longitudinal power density distribution within the beam, as a function of distance from the focused spot, revealed the influence of the position of the focal point (with respect to the top surface) on the final weld bead dimensions. They considered in their study an extensive variation in the temperature dependent material properties but neglected convective heat flow within the molten pool [15] [16].

The heat source being stationary in laser spot welding, the present work assumes a single ellipsoidal profile using $c_1=c_2$, i.e. the extent of the beam is equal in both the front and the rear sections along the longitudinal direction. Although the parameter a is to be determined from the actual weld width, in the present work 2a is considered to be equal to the focus diameter of the laser beam, as only the material directly beneath the beam will be subjected to direct heat input. Further, c_1 and c_2 are assumed to be equal to a, as the stationary beam is symmetric in both the longitudinal and transverse directions. The heat transfer analysis is therefore axisymmetric, with the y axis defined as the axis of symmetry. Therefore, in the current study, the theoretical approach was simplified by using the heat source as a Gaussian parameter as represented in figure 8. This approach was used for the finite element simulation.

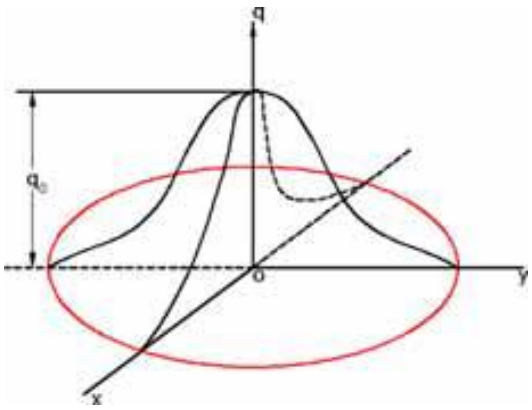

Figure 8 Schematic representation of the Gaussian distribution of the heat source [16]

2.6.2. Heat Transfer in laser spot welds

The governing equation of transient heat conduction in two-dimensional cylindrical coordinates is given by

$$\frac{1}{r}\frac{\partial}{\partial r}\left(rk\frac{\partial T}{\partial r}\right)+\frac{1}{r}\frac{\partial}{\partial z}\left(rk\frac{\partial T}{\partial z}\right)+Q=\rho c\frac{\partial T}{\partial t} \qquad (2)$$

where r and z are radial and axial coordinates, ρ, c, and k are density, specific heat, and thermal conductivity of the material respectively, T and t represent temperature and time respectively, and Q represents the rate of internal heat generation or input heat rate per unit volume [14]. The values of k, c and ρ are temperature dependent. The essential and natural boundary conditions are expressed as

$T=T_{S1}$ (on the portion of the boundary S_1/fusion line) (3)

$k_n\frac{\partial T}{\partial n}-q+h(T-T_0)+\sigma\varepsilon(T^4-T_0^4)=0$ (on the portion of the boundary S_2 and t>0) (4)

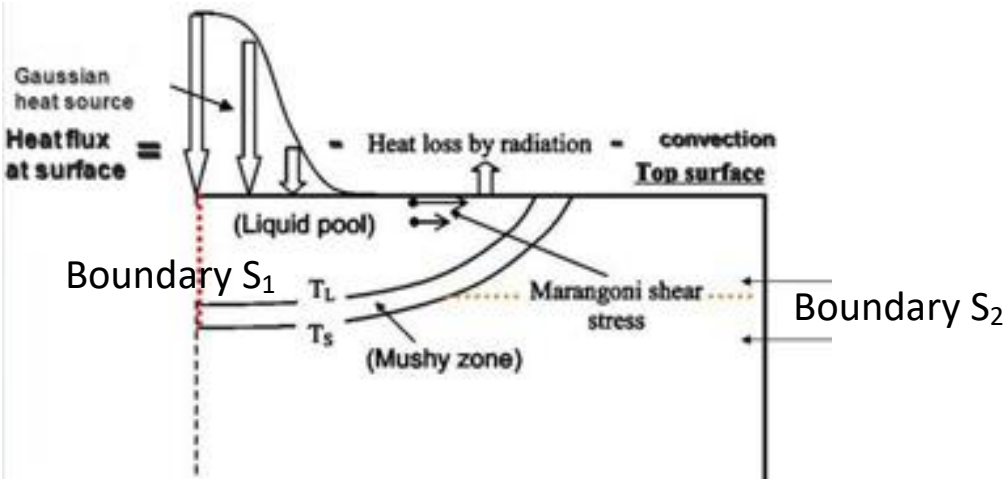

Figure 9 Schematic representation of spot weld pool [26]

S_2 represents those surfaces that may be subject to radiation, convection, and imposed heat fluxes (q), k_n represents the thermal conductivity normal to the surface, T_0 the ambient temperature, h the convective heat transfer coefficient, ε the emissivity, and σ the Stefan–Boltzmann constant for radiation. Instead of considering the radiation term in the boundary condition, the effect of radiation and convection is considered together through a 'lumped' heat transfer coefficient as $h=2.461023 \text{ X } \varepsilon T^{1.61}$ [14] .

Owing to the axial symmetry, the radial heat transfer across the laser beam axis (the symmetry line) is taken as zero, i.e. dT/dr=0. The latent heat of melting and solidification is included in this simulation through an increase or decrease in the specific heat of the material.

2.7. Advanced high strength steels

The use of advanced high-strength steel (AHSS) has increased in popularity in the automotive industry because of its excellent combination of high strength and ductility as seen in figure 10. It allows the thickness of steel, used to make auto body parts to be decreased, which in turn facilitates improved safety [1][2]. The global steel industry has met this need through the development of new AHSS grades, whose unique metallurgical properties and processing capabilities enable the automotive industry to meet the requirements, while keeping cost down [2].

The newer generation of steel grades provides extremely high strength and other advantageous properties. The AHSS could be distinguished based upon the strength properties, mainly, yield strength > 300 MPa and tensile strength > 600 MPa as seen in figure 11. In comparison to the conventional high strength steels, where ductility decreases with strength, modern AHSS steels combine high strength and formability/ductility [1].

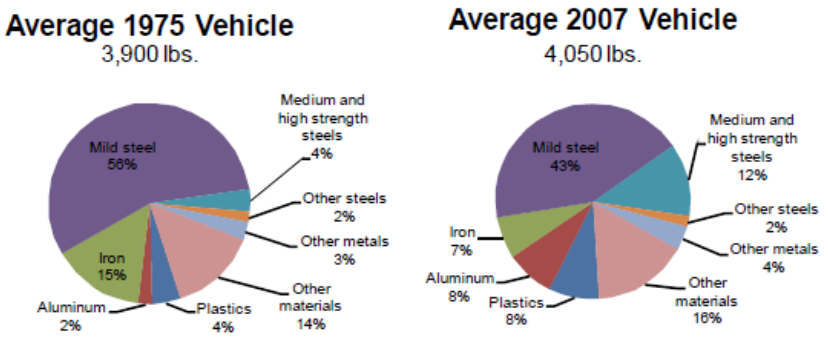

Figure 10 1975 and 2007 average vehicle mass breakdown by material [Data from Ducker Worldwide].

Conventional low to high strength steels include mild, interstitial-free, bake-hardenable and high strength low alloy steels [1] [2]. They typically have low carbon content and minimal alloying element exhibiting good formability and ductility. However, these steels generally have yield strength of less than 550 MPa and ductility that decreases with increased strength [1]. On the other hand, AHSS are more complex, particularly through their microstructures which are multi-phase for an improved combination of strength and ductility. AHSS include dual and complex phase structures, ferritic-bainitic, martensitic, transformation induced plasticity, hot formed and twinning induced plasticity steels. Each has unique microstructural features, alloying additions, processing requirements, advantages and challenges associated with the use.

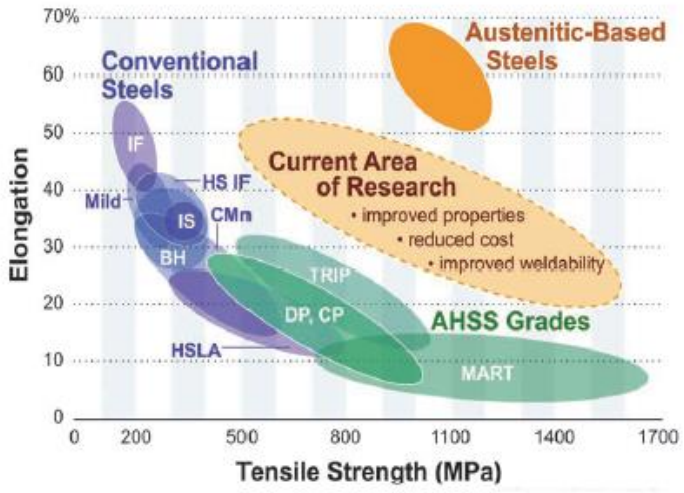

Figure 11 Area of opportunity for third generation steels [1]

2.8. Application aspects of AHSS

As discussed, the combination of high strength and ductility can allow thinner components to be used in the automotive applications and also to improve the safety features due to high energy absorption capabilities. AHSS, compared with conventional high strength steels of comparable strength give the automobile designer a high degree of flexibility to optimize the component geometry.

Other component performance criteria comprise stiffness, durability, crash energy management. A short characterization of AHSS with respect to these criteria is given [2] [3]

2.8.1. Stiffness

The stiffness of a component is affected by the material modulus of elasticity (E), as well as, its geometry. The module of elasticity is constant for steel, which means that changing steel grade does not affect the stiffness. To improve stiffness, the component geometry could be changed. AHSS offer greater design flexibility to optimize the stiffness due to their enhanced formability. This can be done without increasing mass or decreasing strength.

2.8.2. Strength

Loading capacity of a component depends on its geometry and yield and/or tensile strength. AHSS provide an advantage in the design flexibility over conventional high strength steels due to their higher formability and work hardening characteristics. These grades also have good bake hardening ability [2]. Therefore, it is important to account for this strength increase during the design process of car components in order to avoid the over design that may occur when the design process is based upon as rolled mechanical properties specification. Both these features i.e., formability and hardening, enable achieving high strength of as-manufactured components.

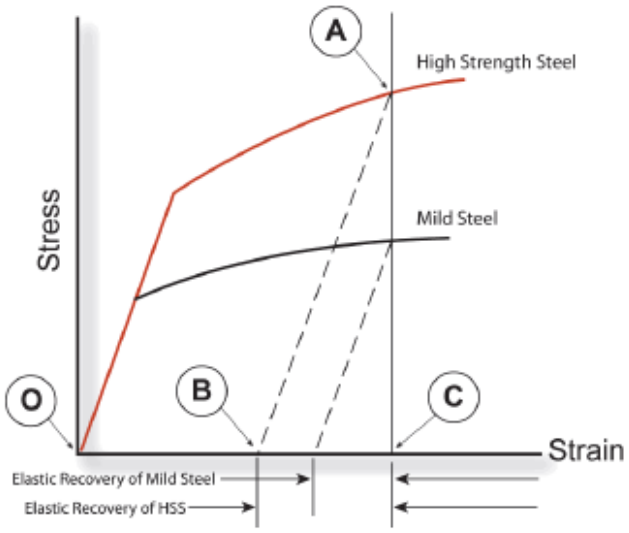

Figure 12 Stress-strain curves illustrating that springback is proportional to stress [2].

Work hardening is schematically represented in figure 12. Referring to figure 12, if a mild steel and high strength steel (HSS) with the same elastic modulus are loaded to equal strain A, when

the load is removed, the HSS will have greater springback (to B). This greater elastic recovery is possible because the HSS was carrying a much greater stress at the same strain.

2.8.3. Fatigue

Fatigue properties of structural components depend on geometry, thickness, applied loads and material endurance limit. The endurance limit of a material increases with tensile strength. Thus, high strength combined with superior work hardening and bake hardening, resulting in a significant increase in the as-manufactured strength of AHSS components, also results in a better fatigue resistance.

2.8.4. Crashworthiness

Crashworthiness is an important characteristic that is currently becoming increasingly important. Recent trends require for a material to absorb more energy in crash scenario. The potential absorption energy can be assessed based upon the area under the stress-strain curves. Better performance in crash of AHSS compared to classical high strength steels is associated with higher work hardening rate and high flow stress. This feature accounts for a more uniform strain distribution in components in the crash event. Both, work hardening and bake hardening significantly improve the energy absorption characteristics due to the yield stress increase.

2.8.5. Formability

AHSS have many advantageous characteristics connected to formability compared to those of HSLA steels with comparable yield strength. AHSS were developed partly to address decreased formability with increased strength in conventional steels. As steels became increasingly stronger, they simultaneously became increasingly difficult to form into automotive parts. AHSS, although much stronger than conventional low- to high-strength steel, also offer high work hardening and bake hardening capabilities that allow increased formability.

2.9. Dual phase and Transformation induced plasticity steels

By 2007, the average vehicle contained 11.6 % medium and high strength steels, for a total steel vehicle content of 57 % as mentioned in section 1.1. During recent times, Dual phase (DP) steels and Transformation induced plasticity (TRIP) steels have emerged as the most important grades in all of the AHSS demands. These steels are excellent in the crash zones of the vehicle due to their high energy absorption. Therefore, only DP steel and TRIP steel have been identified as potential candidates for car body fabrication because of their better formability compared with martensitic steel and their low manufacturing cost compared with TWIP steel [19][20][21].

2.9.1. Dual-phase steels

The microstructure of dual phase steels is composed of a soft ferrite matrix and 10-40 % of hard mastensite as shown in figure 13. This type of microstructure allows achieving the ultimate tensile strength in the range of 500–1200 MPa. The ferrite is continuous for many grades up to DP780, but as volume fractions of martensite exceed 50 % (as might be found in DP 980 or higher strengths), the ferrite may become discontinuous. The combination of hard and soft phases results in an excellent strength-ductility balance, with strength increasing with increasing amount of martensite. When the volume fraction of martensite exceeds 20 %, DP steels are often called partial martensitic [20].

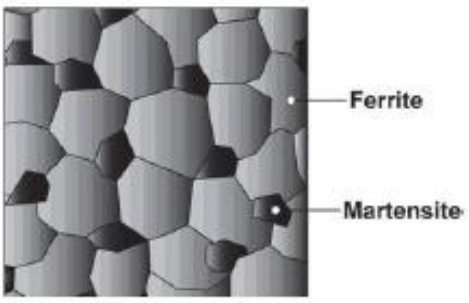

Figure 13 Schematic representation of DP steel microstructure [20]

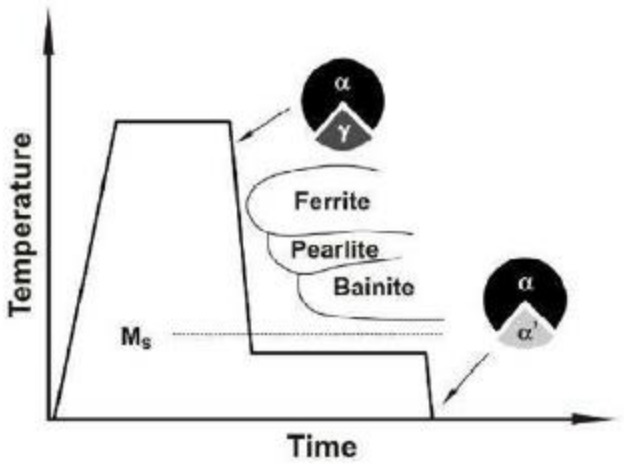

Figure 14 Temperature variations depicting microstructure for DP steels [20]

This dual phase type of microstructure can exhibit the following advantageous features over the conventional high strength steels [20] [21]:

- The strength of the DP steel microstructure is controlled by the amount of martensite and ductility by the size and distribution of this phase,
- DP steels possesses low UTS/YS ratio (around 0.5) and high strain hardening characteristics, especially at the beginning of plastic deformation,
- They can be strengthened by static or dynamic strain ageing
- Grades containing low carbon content have been shown to exhibit excellent resistance to fatigue crack propagation

DP steel is currently one of the most widely used AHSS. Automakers are increasingly employing DP steel to increase strength. Important to consider when designing with DP steel, as with other AHSS, is the effect of strain and bake hardening. DP steels may be developed with low to high yield strength (YS) to ultimate tensile strength (UTS) ratios, allowing for a broad range of applications from crumple zone to body structure.

Modern DP steels are produced in complex processes involving thermo-mechanical processing followed by controlled cooling. For cold rolled DP steels, continuous annealing following cold rolling is being used. Dual phase microstructure can also be developed in a cold rolled sheet material by the application of continuous annealing followed by hot dip galvanising. A schematic diagram of the temperature cycle during the annealing process is given in figure 14.

2.9.2. Transformation induced plasticity steels

TRIP steel received its name for its unique behavior during plastic strain. In addition to the dispersal of hard phases, the austenite transforms to martensite. This transformation allows the high hardening rate to endure at very high strain levels, hence “Transformation-Induced Plasticity.” The possible development of this type of steels was first discovered by Zackay et al. [22]. They proposed that the strain or stress induced transformation of retained austenite present in the microstructure in a sufficient amount can substantially harden the steel during deformation, and therefore results in a higher ductility. The amount of strain required to initiate this transformation may be managed by regulating the stability of the austenite by controlling its carbon content, size, morphology or alloy content. With less stability, the transformation begins almost as soon as deformation transpires. With more stability, the austenitic transformation to martensite is delayed until higher levels of strain are reached, typically beyond those of the forming process.

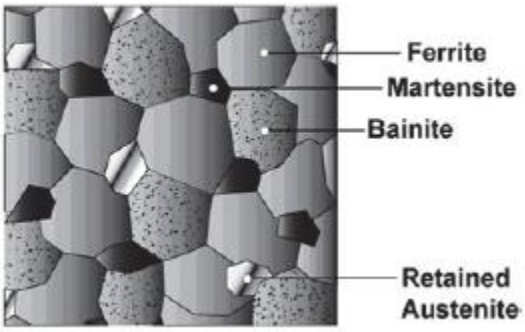

Figure 15 Schematic representation of TRIP steel microstructure [20]

In highly stabilized TRIP steel automotive parts, this delay can allow austenite to remain until a crash event transforms it to martensite. Other factors also affect the transformation, including the specific conditions of deformation, such as the strain rate, the mode of deformation, the temperature, and the object causing the deformation. When the austenite-martensite transformation occurs, the resulting structure is toughened by the hard martensite.

The mechanical properties of TRIP steels are derived from their dispersed multi-phase microstructure which is composed of ferrite α (0.50-0.55 wt. %), bainite (0.30-0.35 wt. %), retained austenite γ (0.07-0.15 wt. %), and possibly martensite (0.01-0.05 wt. %). Schematic representation of microstructure of TRIP is steel is shown in figure 15. Retained austenite is an important phase constituent of TRIP steels. The TRIP steels are characterised by a relatively low content of alloying elements. In the current 700 MPa TRIP steels, the total content of alloying

elements is about 3.5 wt. % [20] [21]. A schematic diagram of the temperature cycle during the annealing process is given in figure 16.

Carbon content in the current TRIP steels is limited to 0.20-0.25 wt.% due to weldability concerns. The recent developments in the TRIP steel production concept includes only partial replacement of Si by a limited amount of Al and use P in the amount of 0.05-0.10 wt.%. Lower Si content makes the steel galvanizable. The use of P is intended to limit the Al content, since P also suppresses the cementite formation and is a very effective solid solution hardening element. It was shown for TRIP steels low in Si that P increases the amount of retained austenite. P also significantly increases the C activity in ferrite. The optimal combination of strength and ductility of TRIP steels is achieved by decreasing ferrite by grain refinement and obtaining a uniform distribution of fine second phase particles [20] [21].

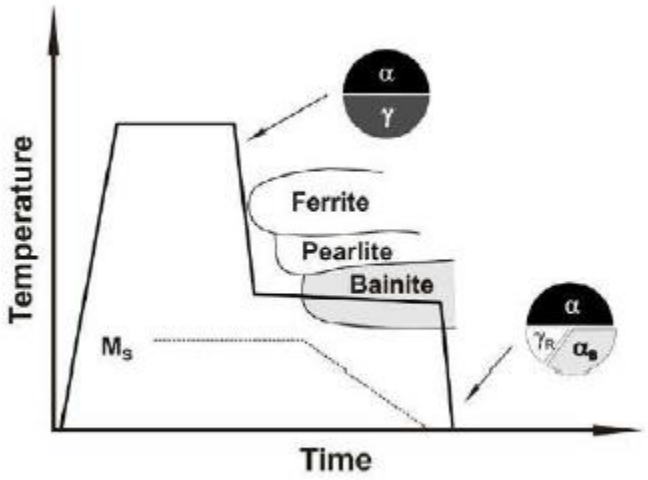

Figure 16 Temperature variations depicting microstructure for TRIP steels [20]

2.10. Solidification behaviour in alloy steels

During the solidification of steel, the solid-liquid interface and the mode of solidification can be planar, cellular, or dendritic depending on the solidification condition and the material system involved. The four basic types of the interface morphology observed during the solidification are shown in figure 17 [22].

The mode of solidification in weld depends on composition and cooling conditions experienced by weld metal at a particular location during the solidification. The kinetics of the liquid-solid

interface is described by the ratio of the thermal gradient (G) and the travel speed of liquid solid interface (R). Thermal conditions during solidification are determined by the heat transfer in the weld pool affecting the temperature gradient (G) at solid-liquid metal interface (°C/mm) and the growth rate of the solidification front (R) as indicated from growth rate (mm/sec) of solid-liquid metal interface []. A combination of a high actual temperature gradient (G) and a low growth rate (R) results in planar solidification, i.e. where liquid-solid interface is plane. A combination of low actual temperature gradient (G) and a high growth rate (R) results in equiaxed solidification. A combination of intermediate G and R values results in cellular and dendritic modes of solidification.

Solute is partitioned into the liquid ahead of the solidification front (figure 18). This causes a variation in the liquidus temperature below which freezing begins. However, a positive temperature gradient in the liquid, gives rise to a supercooled zone of liquid ahead of the interface. This phenomena is called constitutional supercooling which it is caused by composition changes. A small perturbation on the interface will therefore expand into a supercooled liquid. This gives a rise to dendrites. It follows that a supercooled zone only occurs when the liquidus temperature (T_L) gradient at the interface is larger than the temperature gradient (dT/dx) as shown in figure 18.

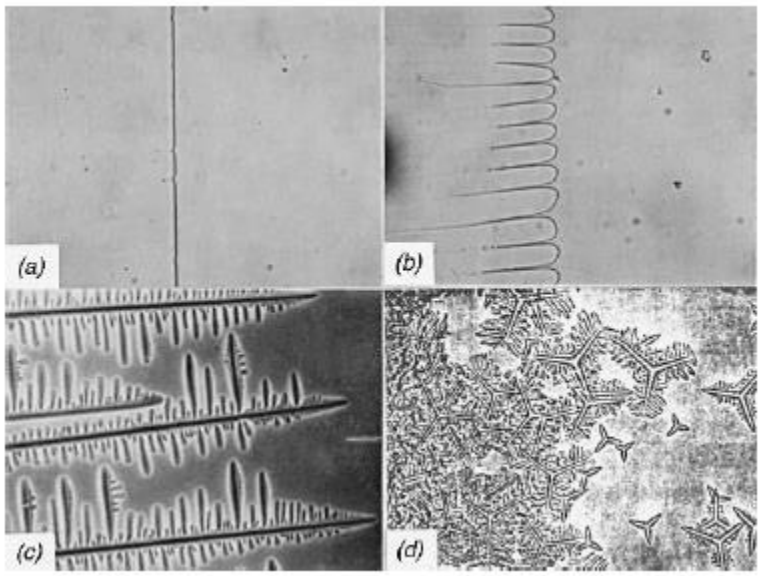

Figure 17 Solidification modes (magnification 67x) (a) planar solidification of carbon tetrabromide (b) cellular solidification of carbon tetrabromide with a small amount of impurity (c) columnar dendritic solidification of carbon tetrabromide with several percent impurity (d) equiaxed dendritic solidification of cyclohexanolwith impurity [22] [23].

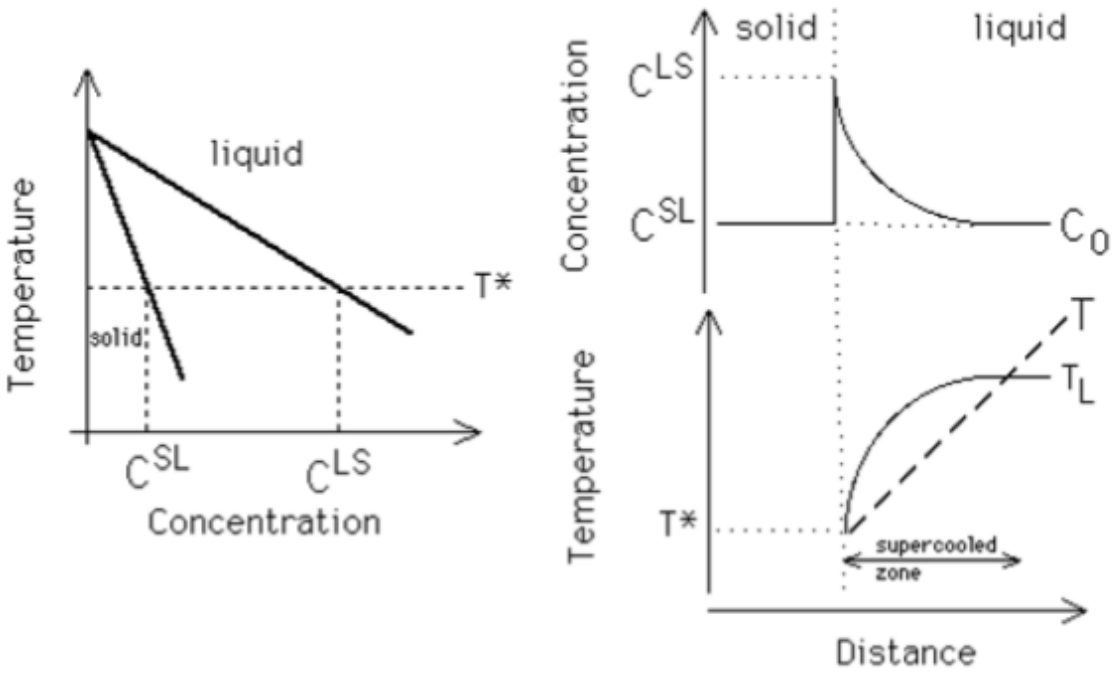

Figure 18 Schematic representation of constitutional supercooling [25].

2.11. Microstructural evolution of grain boundaries

2.11.1. Solidification sub-grain boundaries

During solidification within a single grain, the finest (sub-grain) structure that can be resolved in a light optical microscope is an array of parallel hexagonal cells or dendrites with distorted cubic structure which are separated by 'low-angle' grain boundaries []. These are low angle boundaries since there is virtually no crystallographic misorientation across these boundaries and therefore also known as solidification sub-grain boundary. These boundaries are evident in the microstructure since their composition is different from that of the bulk microstructure. This difference is a result of microscopic solute redistribution, also referred to as Scheil partitioning [23]. Columnar grains typically grow along the three <100> easy growth directions in bcc and fcc structures. Figure 19 shows the schematic of dendritic easy growth directions in cubic structures [23].

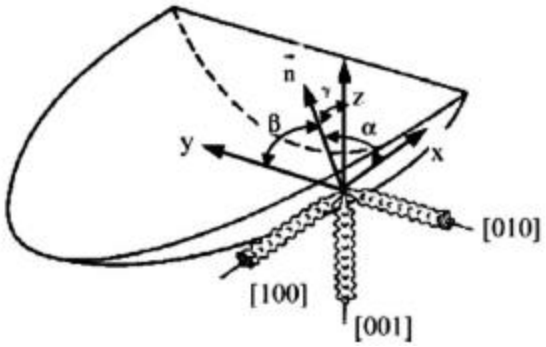

Figure 19 Schematic representation of dendrites arm along the three easy growth direction for fcc and bcc [23].

2.11.2. Solidification Grain Boundaries

The solidification grain boundary results from the intersection of packets, or groups of sub-grains as shown in figure 20. Thus, grain boundaries are the direct result of bulk growth that occurs along the trailing edge of the weld pool. Each of these packets consisting of dendrites has their own crystallographic direction as a result of different growth direction. As these packets intersect, they form a boundary with a high angular misorientation. These are referred to 'high angle' grain boundaries. This misorientation results in the development of a dislocation network at the grain boundaries [23].

They also have a compositional component besides its crystallographic component. This composition component is a result of the solute redistribution during solidification. This distribution can be modelled by macroscopic solidification and often leads to a high concentration of solute and impurity elements [].

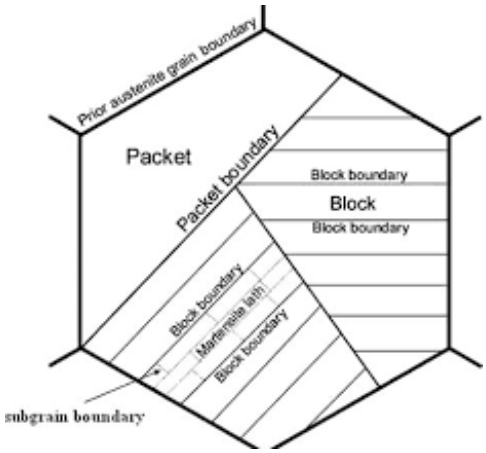

Figure 20 Schematic representation of grain boundaries as packets [24]

2.11.3. Migrated Grain Boundaries

Migrated grain boundaries are mostly seen in fully austenitic weld metal. As it has been already described, the grain boundaries that form at the end stages of solidification have both a crystallographic and a compositional component. In some cases, when the crystallographic component of the grain boundaries migrate away from the compositional component, a boundary with high angle misorientation is formed which is called a migrated grain boundary. The driving force for such a phenomenon is the same as for simple grain growth in base metals, a lowering of the boundary surface energy [23] [25].

2.12. Fusion zone solidification cracking

In the fusion zone, upon completion of a weld, formation of defects may take place. One such effect is the weld solidification cracking in the fusion zone of the weld pool. Solidification cracks are normally readily distinguished from other types of cracks due to the following characteristic factors [26] [27]

- They occur only in the weld metal.
- They normally appear as straight lines along the centre-line of the weld bead, as shown in figure 21 a. Figure 21 b shows direction of grains in each weld spot is towards the spot center in pulsed laser welding. There is a clear solidification boundary between the two successive spots. Brittle cracks are observed in this case.
- Solidification cracks in the final crater may have a branching appearance as the cracks are often open, i.e., they can be visible to the naked eye.

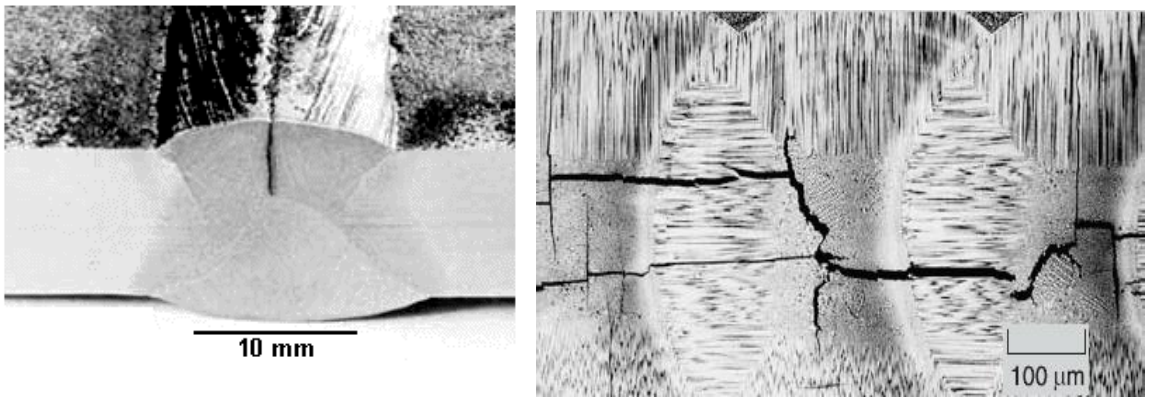

(a) **(b)**

Figure 21 (a) Centre-line cracking and (b) brittle cracks observed in pulsed laser welding [26] [27]

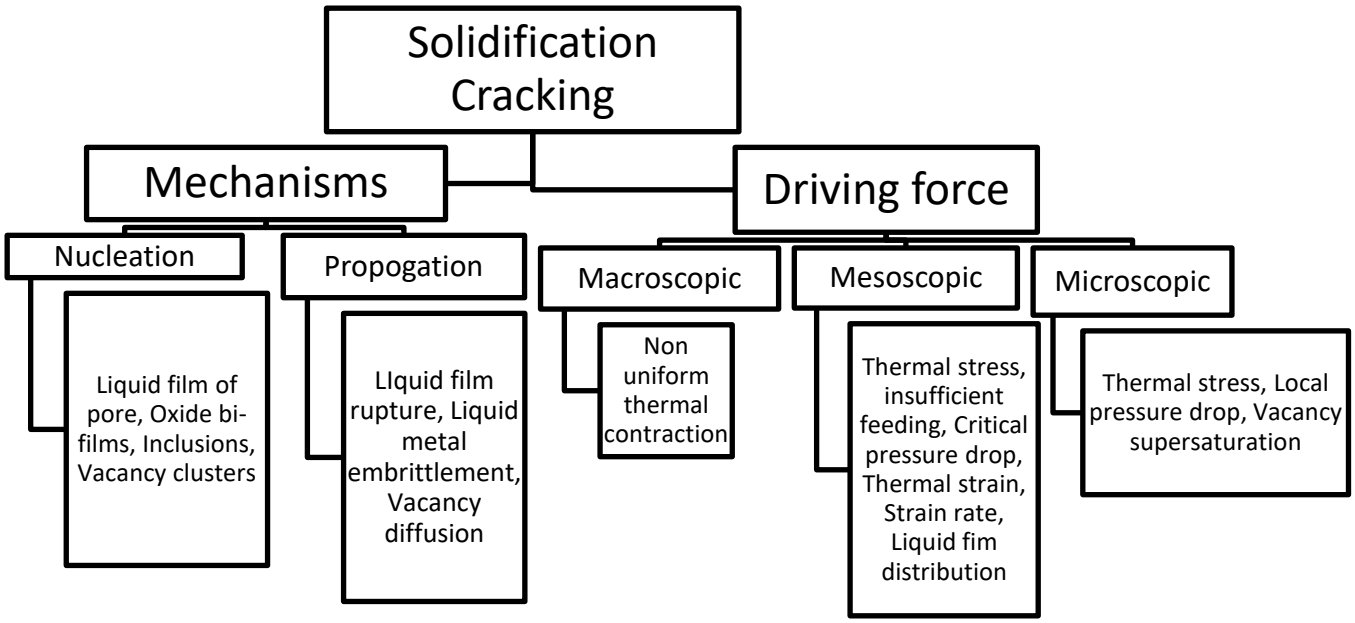

Figure 22 Summarised flow chart for weld solidification cracking

The possible causes of cracking as summarized in figure 22 are [26] [27]

- Strain on the weld pool is too high. The overriding cause of solidification cracking is that the weld bead in the final stage of solidification has insufficient strength to withstand the contraction stresses generated as the weld pool solidifies.
- Liquid cannot reach the regions where it is needed due to inadequate supply or blockage/ narrow channels between solidifying grains.
- Inappropriate weld bead size or shape. Joint design can have a significant influence on the level of residual stresses. Large gaps between component parts will increase the strain on the solidifying weld metal, especially if the depth of penetration is small. Therefore, weld beads with a small depth-to-width ratio, such as formed in bridging a large gap with a wide, thin bead, will be more susceptible to solidification cracking
- Welding under high restraint. An elliptically shaped weld pool is preferable to a tear drop shape. Fast welding speeds, which result in a large separation between the weld pool and cracking locations, increase the risk of cracking.

- Material properties such as high impurity content or a relatively large amount of shrinkage on solidification. Segregation of impurities to the centre of the weld also encourages cracking. Concentration of impurities ahead of the solidifying weld front forms a liquid film of low freezing point which, on solidification, produces a weak zone. As solidification proceeds, the zone is likely to crack as the stresses through normal thermal contraction build up. Welding with contaminants such as cutting oils on the surface of the parent metal will also increase the impurities in the weld pool and the risk of cracking.

Usually, there is no simple relation between factors making direct correlations challenging between observation and theory. Here, thermal-metallurgical interactions control the solidification microstructure, while, thermal-mechanical interactions control the local and global stresses and strains.

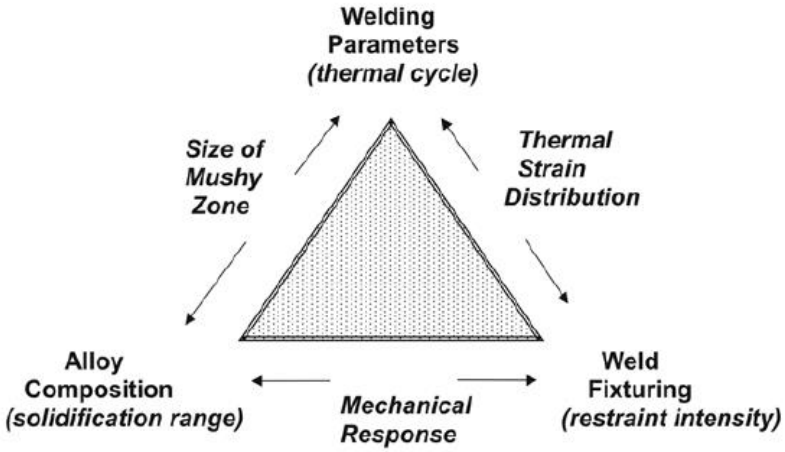

Figure 23 Diagram indicating complex interaction between process parameters affecting weld solidification cracking [28]

2.13. Solidification cracking theories

Numerous theories have been proposed to describe the conditions required for crack initiation. The initiation involves a complex interaction between metallurgical and mechanical factors with the additional requirement of temperature gradients generated during welding. The hot cracking susceptibility (HCS) coefficient proposed by Clyne & Davies [29] is defined as the ratio

of the susceptible time and the time available for backfilling or the stress-relief process. In Feurer's criterion [29], cracking is related to the difficulties of backfilling of the terminal liquid phase through the mushy zone in competition with solidification shrinkage. In Katgerman's criterion [29] the theoretical considerations of Clyne & Davies and Feurer are combined. The applications of these criteria in the prediction of hot tearing behavior in direct chill casting have been investigated by Suyitno et al. [29].

The 'Shrinkage-Brittleness Theory' was proposed by Bochvar for the cracks in aluminum casting above the solidus temperature [28]. Following the Bochvar's work with aluminum casting, Pumphrey finalised the theory to describe the cracking behaviour of aluminium alloy welds during solidification [26]. The theory explains that a solidifying alloy represents a temperature in which dendrite interlocking occurs during cooling. This temperature is called coherence temperature. The proportion of the liquid to solid above the coherence temperature is large enough that cracking will not occur. However, below the coherence temperature, solid-solid interaction begins to take place between adjacent dendrites and the remaining liquid films may rupture due to the strain accommodation. If sufficient amount of liquid exist (such as in alloys with the large amount of eutectic formation), crack healing may occur where liquid flow into crack or freshly formed void [30].

Pellini developed the 'Strain Theory' to describe the observation of hot tears is castings and then for the occurrence of solidification cracking in weld metals. It was explained that solidification process undergoes two stages. A "mushy condition" and then followed by a "film stage" where solidification cracking may occur. The mushy condition is considered by simultaneous presence of solid and liquid at the solidifying weld pool, but the strain at this stage is uniformly distributed and prevents cracking. During the film stage, the continuous liquid film exists along interdendritic region while strain accumulation at interdendritic regions occurs due to the temperature gradient in the solid. Consequently, the liquid film can be separated at interdendritic regions [31].

In 1960 Borland introduced the 'Generalized Theory' to explain the solidification cracking phenomenon and overcome the apparent shortcomings of both the 'Shrinkage-Brittleness 'and 'Strain Theory'. Borland classified the solidification process into four stages based on the quantity and distribution of liquid. During the first stage dendrites are widely dispersed by large amount of liquid. Following the first stage, at the second stage Borland defined the coherent temperature that upon crossing this temperature dendrite interlocking occurs. If below coherent temperature the amount of liquid was not enough, cracking might occur just below the coherent temperature. Upon further cooling, a critical temperature is reached in which dendrite formation has progressed to the point that interdendritic liquid networks become isolated and cracking healing is not possible. Borland referred to this region as the critical

solidification range (CSR). It is in this region, below the critical temperature and above the solidus temperature (complete solidification), that solidification cracking occurs. Following the third stage, at the final stage of the solidification, no liquid is present any more and cracking occurs.

Table 1 Summary of known theories based on solidification cracking behavior

Mechanisms and Conditions	Suggested and Developed by
Cause of solidification cracking	
Thermal contraction	Heine (1935), Pellini (1952), Dobatkin (1948)
Liquid film distribution	Vero (1936)
Liquid pressure drop	Prokhorov (1962), Niyama (1977)
Vacancy supersaturation	Fredriksson et al. (2005)
Nucleation	
Liquid film or pore as stress concentrator	Patterson et al. (1953, 1967), Niyama (1977), Rappaz et al. (1999); Braccini et al. (2000), Suyitno et al. (2002)
Oxide bi-film entrained in the mush	Campbell (1991)
Vacancy clusters at a grain boundary or solid/liquid interface	Fredriksson et al. (2005)
Profogation	
Through liquid film by sliding ;	Patterson (1953), Williams and Singer (1960, 1966), Novikov and Novik (1963)
By liquid film rupture	Pellini (1952), Patterson (1953), Saveiko (1961), Dickhaus (1994)
By liquid metal embrittlement	Novikov (1966), Sigworth (1996)
Through liquid film or solid phase depending on the temperature range	Guven and Hunt (1988)
Diffusion of vacancies from the solid to the crack	Fredriksson et al. (2005)
Conditions	
Thermal strain cannot be accommodated by	Pellini (1952), Prokhorov (1962), Novikov

liquid flow and mush ductility	(1966), Magnin et al. (1996)
Pressure drop over the mush reaches a critical value for cavity nucleation	Niyama (1977), Guven and Hunt (1988), Rappaz et al. (1999), Farup and Mo (2000)
Strain rate reaches a critical value that cannot be compensated by liquid feeding and much ductility	Pellini (1952), Prokhorov (1962), Rappaz et al. (1999), Braccini et al. (2000)
Thermal stress exceed rupture or local critical stress	Lees (1946), Langlais and Griuzleski (2000), Lahaie and Bauchard (2001), Suyitno et al. (2002)
Stresses and insufficient feeding in the vulnerable temperature range	Bochvar (1942), Lees (1946), Pumphrey and Lyons (1948), Clyne and Davies (1975), Feurer (1977), Kargerman (1982)
Thermal stress exceeds rupture stress of the liquid film	Saveiko (1961)

2.14. Controlling factors

Over the years, much more effort has been put on the conditions required for solidification cracking occurrence rather than on the mechanisms of crack initiation and propagation. When it comes to the nucleation and propagation of solidification cracks, an educated guess frequently replaces experimental proof. Figure 9 also shows that the conditions for and causes of solidification cracking can be considered on different length scales, from macroscopic to microscopic. Some of these conditions are important on both macroscopic and microscopic scales.

Today, the macroscopic mechanical parameters such as strain, strain rate are believed to be the most important factors and some modern models are based on it. The physical explanation of this approach is that semisolid material during solidification can accommodate the imposed thermal strain by plastic deformation, diffusion-aided creep, structure rearrangement, and filling of the gaps and pores with the liquid. All these processes require some time, and the lack

of time will result in fracture. Therefore, there exists a maximum strain rate that the semisolid material can endure without fracture during solidification [32].

However, it is worth noting that most of the existing solidification cracking criteria deals with the conditions rather than with the mechanisms of solidification cracking. These factors are identified below, grouped for comparison as either mechanical and/or metallurgical in nature.

2.14.1. Mechanical factors which affect solidification cracking in welds

Assuming that all thermo-metallurgical conditions are held constant (e.g. constant alloy composition and cooling rate), the conditions required to initiate and propagate cracking from a purely thermo-mechanical aspect is a criteria itself. This serves to deduce proper theoretical solutions from problems based on variable metallurgical influences. With this regard, cracking is caused from the strains that arise from the weld thermal experimentations, including both thermal and solidification shrinkage, affected by weld heat input and conditions of restraint.

2.14.1.1. Strain

Pellini, in his “Strain Theory”, proposed that cracking occurs when an inter-granular liquid film is strained beyond some critical value [32]. Strain has been assumed to play a decisive role in controlling solidification cracking as a mechanical factor. The amount of strain that a liquid film will experience is determined by the film life. The film life is determined by the solidification range and the weld cooling rate as explained.

There are several strain limitation concepts from Pellini’s theory. Both Prokhorov and Senda, et al established ductility curves, defining the maximum strain tolerated before cracking occurs. According to these theories, the solidification range defines the upper and lower temperature bounds, and the critical ductility curve is determined experimentally (controlled strain in weldabilitiy tests). Cracking will occur if the deformation curve, representing strain across the mushy zone, intersects the ductility curve as shown in figure 24. For crack initiation, the total strain $\varepsilon=\varepsilon_{int}+\varepsilon_{ext}$ must be lower than the ductility. The internal strain ε_{int} comprises the thermal

strain and the strain resulting from volume change during liquid/solid phase transition. External strains ε_{ext} are generated by external mechanical stressing.

2.14.1.2. Stress

As stress and strain are linked through continuum mechanics, stress must play a role in any of the cracking mechanisms involving strain. Chihoski provided an early analysis of the local compression and tension stress cells that follow a moving weld pool, demonstrating how the relative size and location of these cells will vary with welding parameters [32].

Finite element models have been used to evaluate local stresses in weldability studies [32]. Zacharia has shown that by applying a high cross-weld stress in a Sigmajig test, the trailing end of the mushy zone will experience a tensile stress resulting in cracking [33].

Liquid films possess a critical strength dependent upon surface tension and thickness [32]. Dendrite coherency should provide additional resistance to stress. Thus, it seems plausible that a weld mushy zone must possess some inherent strength. Various experimental tests have been developed in an attempt to measure the strength of liquid-solid mushy zones, including the Gleeble tests [34].

2.14.1.3. Strain rate

The importance of strain rate on cracking has been accepted from early analyses. From the work of Prokhorov and Senda, the rate of deformation, normal to the weld, is required to determine whether the critical strain for cracking is achieved [31]. The slope of the deformation curve in figure 24. It can be related to strain rate (dε/dt) and cooling rate (dT/dt) as

$$d\varepsilon/dT = \frac{(d\varepsilon/dt)}{(dT/dt)}$$

If the slope is intersecting the BTR then hot cracking will occur. Several weldability tests have been specifically developed to measure the critical strain rate required for cracking such as VDR (Variable deformation test) test and PVR (Programmed deformation rate) test [31][32].

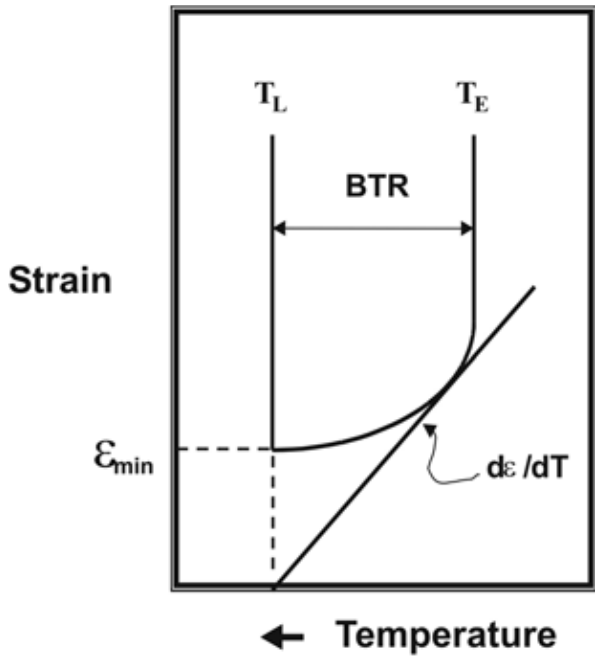

Figure 24 Schematic representation of ductility curve indicating critical strain [31]

2.14.2. Metallurgical factors which affect solidification cracking in welds

There are a number of metallurgical factors that can affect the solidification cracking susceptibility of metals. These factors are presented in further detail in this section [28] [29] [30].

2.14.2.1. Solidification temperature range

The weakest and most susceptible region to solidification cracking during welding is the mushy zone where both solid and liquid exists. Therefore, the larger this solid/liquid region is, the more susceptible the metal is to cracking. In steel welds, liquid films usually manifest as a result of the segregation of low melting point eutectics containing impurities such as S, P and alloying additions such as C, Ni, Ti, Mn and Nb.

The segregation of the solutes, generally speaking, increases the alloys solidification (freezing) temperature range (STR) as illustrated in figure 25, with S showing the most detrimental increase to the STR. A large STR promotes solidification cracking due to the increased time in which the alloy spends in the susceptible state in which thin liquid films exist between the dendrites [29]. Due to the complexity of the mechanisms involved in solidification crack formation, several models developed to date are based simply upon the STR being used as a gauge to measure the cracking susceptibility [29].

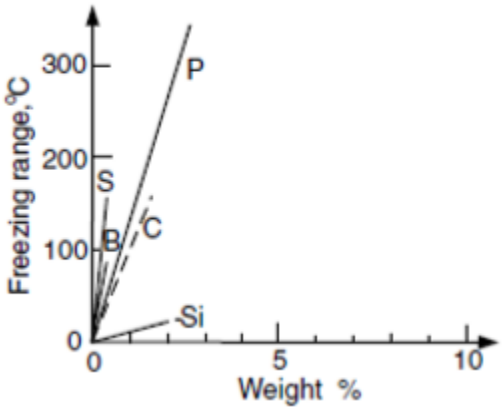

Figure 25 Solidification temperature range representation for different solute elements [29]

2.14.2.2. Solubility of solute elements in the primary solidification phase

Literature suggests that alloys with large solute content, and hence large quantities of eutectic, will be less susceptible to cracking [29]. This is because there is a less extensive coherent dendrite structure and shrinkage can be more readily fed by means of back-filling due to a more open dendrite array.

This reasoning can be used to explain the peak susceptibility behaviour typically observed in aluminum alloys, where high alloy content in base metal or filler metal often results in improved weldability [29][30]. Filler metal alloys are typically high in alloy content for this reason. Al-Si filler alloys in particular, which generate large quantities of eutectic, are known for their exceptional weldability.

2.14.2.3. Surface tension of grain boundary liquid

If the surface tension between the solid grains and grain boundary liquid is very low, a liquid film will form between the grains. Figure 26 depicts the continuous liquid film and as a result of the continuous nature of the film, solidification cracking susceptibility will be high. If the last liquid to solidify wets the dendrites (i.e. low $\gamma_{L/S}$), there will be higher chances of a continuous network of liquid providing back-filling [29] [30].

However, if no wetting occurs (i.e. high $\gamma_{L/S}$), bridging between dendrite arms is promoted, resisting strain, and thus avoiding cracking. It is at intermediate values of wettability, between these two extremes, where cracking is encountered. At higher surface tension, the liquid phase will be globular, as illustrated in figure 25. Such discontinuous liquid globules do not significantly reduce the strength of the solid network, and therefore, are not as detrimental.

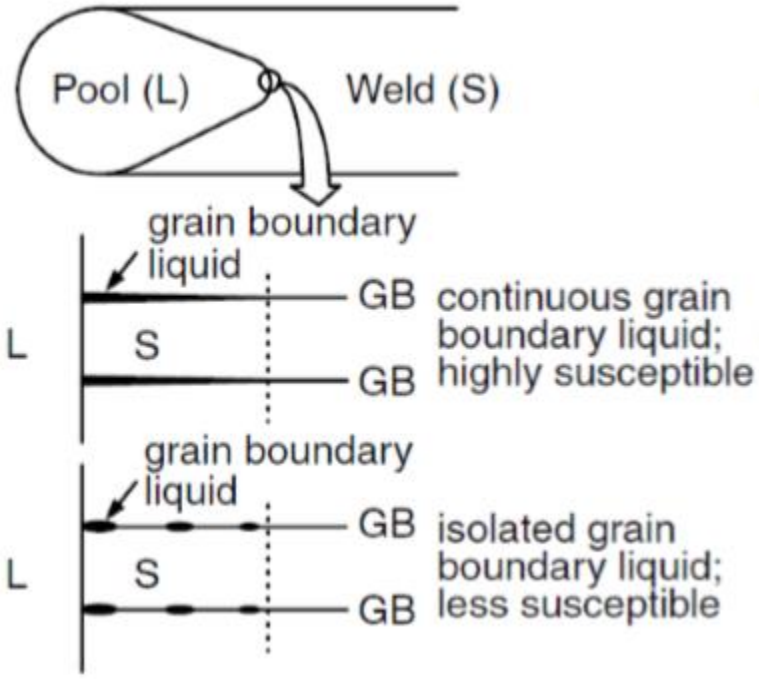

Figure 26 Surface tension criteria [29]

2.14.2.4. Solidification grain structure

Fine equiaxed grains are often less susceptible to solidification cracking than coarse columnar grains [34]. Fine equiaxed grains can deform to accommodate contraction strains more easily, i.e., it is more ductile, than columnar grains. Liquid feeding and healing of incipient cracks can also be more effective in fine-grained material. In addition, the grain boundary area is much greater in fine-grained material and, therefore, harmful low-melting point segregates are less concentrated at the grain boundary.

It is interesting to note that, due to the steep angle between columnar grains (growing from opposite sides of the weld pool), welds made with a tear drop shaped weld pool tend to be more susceptible to centreline solidification cracking than welds. A steep angle seems to favour the head-on impingement of columnar grains growing from opposite sides of the weld pool and the formation of the continuous liquid film of low-melting-point segregates at the weld centreline. As a result, centreline solidification cracking occurs under the influence of transverse contraction stresses.

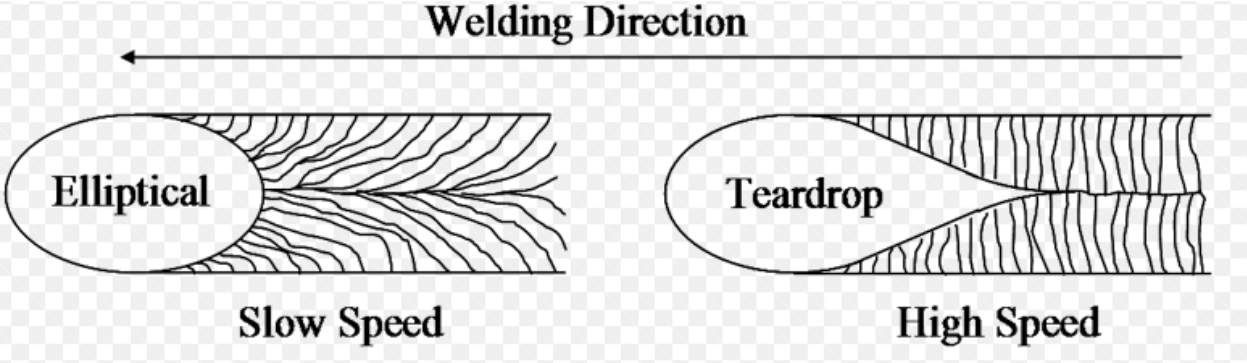

Figure 27 Representation of weld pool formation [34]

2.15. Liquation Cracking

Liquation cracking occurs in partially melted zone (PMZ) as a result of the large quantity of alloying addition that form eutectic phase with low melting point. The liquid will tear if sufficient stress is present [35]. Means to combat liquation cracking is more limited in comparison with solidification cracking as it occurs in the base metal where compositional control are usually outside the scope of welding process.

By definition, the region of the heat affected zone (HAZ) within which liquation occurs is limited to the PMZ and, thus, hot cracking or cracking resulting from liquation, is indigenous to the PMZ [35]. Since the term hot cracking has been generally used in the welding literature to describe high-temperature cracking in both the weld metal and HAZ, its use is often ambiguous. As a consequence, the terms weld solidification cracking and HAZ liquation cracking have been adopted here to more accurately classify weld metal and HAZ hot cracking, respectively.

Mechanisms used to describe HAZ liquation cracking support a grain boundary penetration mechanism. The penetration mechanism for HAZ liquation cracking involves the interaction of a migrating HAZ grain boundary with liquating matrix particles such as carbides, sulfides, borides, etc. The metallurgical basis for this mechanism is a phenomenon known as constitutional liquation. Constitutional liquation was first proposed by Savage from a strictly theoretical standpoint in 1959 [35].

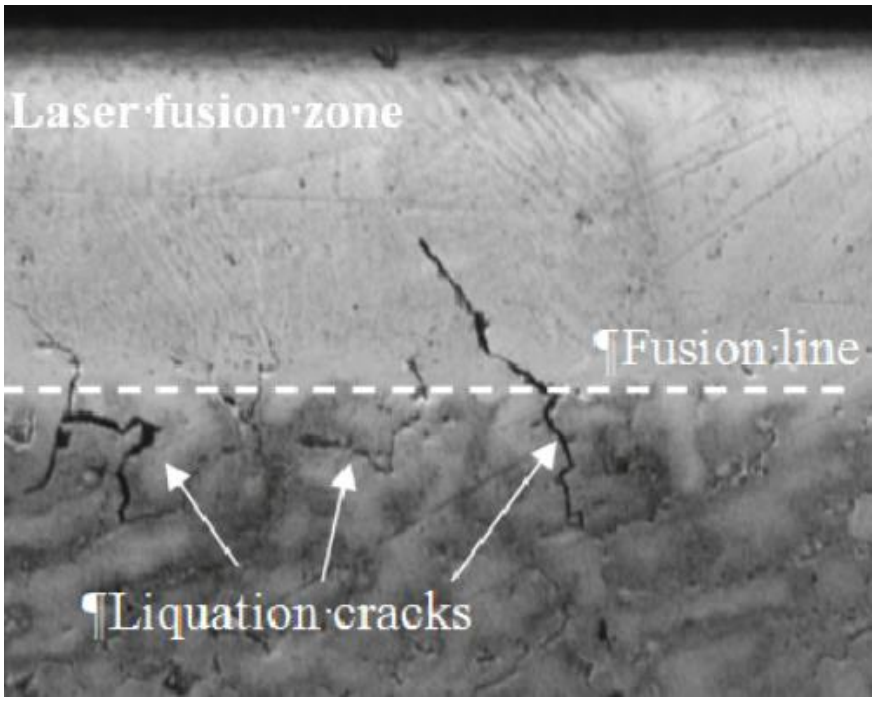

Figure 28 Representation of Liquation cracking in comparison to cracking in fusion zone [36]

Constitutional liquation is a non-equilibrium phenomenon associated with the rapid heating rates experienced in the HAZ adjacent to the fusion line. As certain constituent particles are rapidly heated to temperatures below the matrix solidus temperature, localized liquation occurs along the particle-matrix interface. This liquation is a consequence of the rapid

dissolution of the constituent particle at elevated temperatures and the resultant metallurgical reaction at the particle/matrix interface. The amount of liquid that forms along the interface depends on the heating rate, the dissolution kinetics of the constituent particle, and the diffusivity of solute atoms in the matrix. For example, if heating rates are extremely rapid, as in the HAZ of an electron beam or laser beam weld, particle dissolution is negligible and constitutional liquation would be minimized [35].

Chapter 3 Methodology

To study the solidification cracking behaviour experimentally, a modified version of controlled tensile weldability (CTW) test was adopted. This CTW–hot cracking test developed at BAM Federal Institute for Materials Research and Testing represents in its form an externally loaded hot cracking test [31]. Possibility of modification helps in choosing specimen dimensions, applicable welding process, as well as welding direction relative to the loading direction. Loading in the CTW–hot cracking test is based on tension. The specimen is subjected to the tensile load at a defined loading rate prior to or during welding.

Following the work of Prokhorov, the thermo mechanical aspect suggests that critical strains and strain rates that occur during welding in the vicinity of the solidification front are the cause of material separation. Subsequent specimen stressing for widening potential hot cracks is usually carried out in conventional test facilities, followed by light microscopical evaluation.

3.1. Material and sample geometry

All the controlled tensile weldability experiments were conducted using pre-cut dog bone samples for both the materials. Figure 29 provides the dimensions of the samples

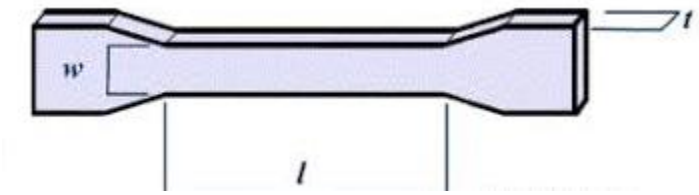

Figure 29 Dog bone sample geometry

Width (w) = 12.7mm
Length (l) = 57mm
Thickness (t) = 1.2mm

For this project, two types of AHSS, a DP 1000 and TRIP 700 steel, were examined. The yield strength of DP 1000 is 666 MPa. The chemical compositions of these two steels are given in Table 2 [37]. Properties of DP and TRIP steels based on the chemical composition given in Table 2 are shown in figure 30. DP steel exhibits a consistently higher density than TRIP steel [37]. The heat conductivity of DP steel is larger than that of TRIP steel below 1000 K, and becomes similar

above 1000 K. The specific heat capacity of these two steels is similar until the solidus temperature. TRIP steel shows a slightly higher specific heat capacity due to the latent heat during the solid–liquid phase transformation.

Table 2 Chemical compositions of TRIP and DP steels (in wt.%, with Fe balance)

	C	Mn	Si	P	Al
DP 1000	0.15	2.3	0.1	0.01	0.03
TRIP 700	0.19	1.63	0.35	0.089	1.1

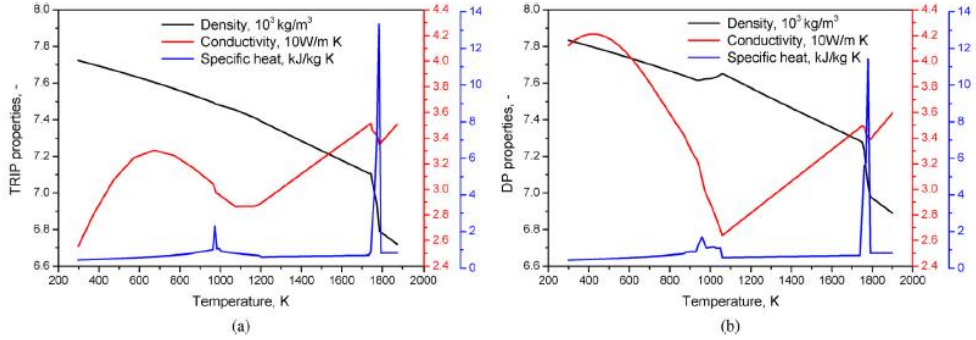

Figure 30 Temperature-dependent thermal properties of (a) TRIP 700 and (b) DP 1000 steel with chemical compositions defined in Table [37]

3.2. Welding experimentation

Spot welding experiments were performed using a 3 kW Nd:YAG laser as the heat source with a beam pilot diameter of 7 mm. The laser beam was out of focus on the top surface to achieve the required spot size in comparison to the width of the sample plate. A focal length of 195 mm was used for spot welding with a weld time of 2s. Bead on plate welding at a focal length of 169 mm (in focus) was also conducted on few samples for a comparison, which will be explained in the later sections. Here, the welding parameters were heat input and constraining conditions (tensile load) as the variables used during the experiments for both the materials. These experiments were conducted as a form of series for the later part of the study. Argon gas was used during welding as a shielding agent. All the welds were made twice for top surface and cross-sectional inspection. Table 3-6 provides the laser conditions, combined with the constraining conditions.

Table 3 DP steel welded at a constant load and variable laser power

S.no.	Material	Designation	Power (W)	Load (kg)	Applied stress (MPa)	Time (s)
1	DP1000	DPP1	700	300	196.85	2
2	DP1000	DPP2	800	300	196.85	2
3	DP1000	DPP3	900	300	196.85	2
4	DP1000	DPP4	1000	300	196.85	2
5	DP1000	DPP5	1100	300	196.85	2

Table 4 TRIP steel welded at a constant load and variable laser power

S.no.	Material	Designation	Power (W)	Load (kg)	Applied stress (MPa)	Time (s)
6	TRIP700	TRP1	700	300	196.85	2
7	TRIP700	TRP2	800	300	196.85	2
8	TRIP700	TRP3	900	300	196.85	2
9	TRIP700	TRP4	1000	300	196.85	2
10	TRIP700	TRP5	1100	300	196.85	2

Table 5 DP steel welded at a constant laser power and variable load

S.no.	Material	Designation	Power (W)	Load (kg)	Applied stress (MPa)	Time (s)
11	DP1000	DPP6	1000	0	0	2
12	DP1000	DPP7	1000	150	98.42	2
13	DP1000	DPP9	1000	450	295.27	2
14	DP1000	DPP10	1000	600	393.7	2

Table 6 TRIP steel welded at a constant laser power and variable load

S.no.	Material	Designation	Power (W)	Load (kg)	Applied stress (MPa)	Time (s)
15	TRIP700	TRP6	1000	0	0	2
16	TRIP700	TRP7	1000	150	98.42	2
17	TRIP700	TRP9	1000	450	295.27	2
18	TRIP700	TRP10	1000	600	393.7	2

3.3. Test setup

The aim of this project was to study the effect of mechanical load on the solidification cracking behavior of AHSS during welding by application of an external tensile load on the sample plate. The approach has close analogy with material movements causing hot cracks in real component welds, externally loaded hot cracking test procedures are aimed at deforming the weld pool area thermo-mechanically.

3.3.1. Global load measurements

In externally loaded tests, the forces required for specimen straining are imposed by an external mechanical testing device. Therefore, all the samples were clamped with a load setup device as shown in figure 31. The device was manually operated for pre-loading. A digital load cell was attached to the sample to record the load variations as a result of welding. The connected scope presented results in the load variation during the experiment and subsequently recorded the output data for further analysis. The variation in load was recorded in units of voltage. Appendix details out the voltage calibration with kg as SI units.

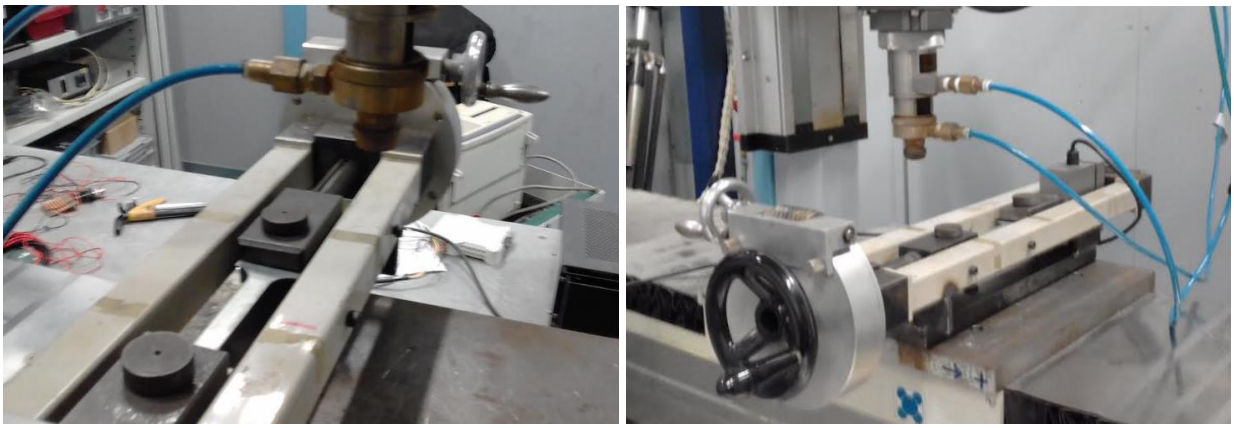

Figure 31 Load setup (front and top view)

3.3.2. Temperature measurements

For temperature measurements during the welding process, spot-welded Type K thermocouple was used at two positions at the top surface and the bottom surface at a distance of 10 mm from the weld centerline as shown in figure 32. Type K (chromel–alumel) is the most common general-purpose thermocouple with sensitivity of approximately 41 µV/°C. It is inexpensive and operates very well in oxidizing atmospheres. The scope recorded the temperature data simultaneously with the loading data.

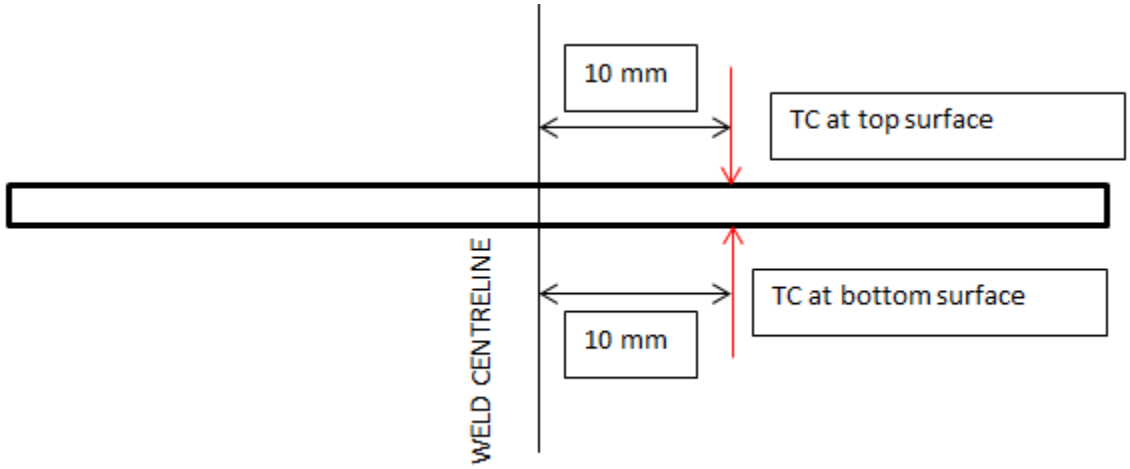

Figure 32 TC represents the position of the attached thermocouple (side view) on the top and the bottom surface of the sample at a distance of 10 mm from the centre of the intended weld spot

3.3.3. Strain measurements

Digital imaging correlation or DIC is a non-contact optical technique for measuring strains. In principle, DIC compares a series of grey-scale images of a sample at different stages of deformation, tracks pixels movement in the region of interest (ROI) and calculates displacement and strain by the use of correlation algorithm [38].

DIC consists of at least digital camera, zoom objective and PC software. Before mechanical tests, specular markers should be applied on the sample surface in order to let the camera capture their movement and track them. Therefore, the markers are of great importance and

can be obtained by spraying, etching or self-roughness (or texture). During the test, consecutive pictures are taken by one or more cameras while samples are under deformation tests, the number of cameras depends on whether the analysis is 2D or 3D.

From the perspective of function and economy, DIC has some outstanding advantages compare to conventional strain measurement. As a non-contact tool, DIC can obtain large visual area and provide clear image whose physical pixel size can be on the micrometer scale. This property can make DIC of great value in special testing environments such as vacuum chamber, x-ray scattering, high temperature etc. DIC has the capability to track specular patterns in subsets over the whole ROI (region of interest), which means a full field measurement contains considerable amount of experimental data can be used to map the displacement contour plot and strain distribution etc. The strain maps reveal phenomena like localization, further contribute to materials studies, e.g. crystallography. Compare to other nondestructive testing, DIC possesses high economic efficiency [30].

For DIC measurement, sufficient illumination is a critical factor for obtaining high quality images, the analysis will benefit from the light to a large extent, and the light direction should also be vertical to the sample surface, otherwise shades result from irregularity of the surface will change and therefore affect the correctness of analysis. Fine and even speckle pattern will also benefit the analysis.

A goal-oriented optical method for determining local critical strain and strain rates is the so-called MISO (Measurement by Means of In-Situ Observation) method by Matsuda et al. [30]. This method uses a high speed camera in combination with an optical magnifying device to record hot crack formation. The MISO method performs adequately, excepting the situations, where the difficult optical conditions (smoke, smears) in the vicinity of the weld pool along with the high magnifications lead to an increase in measurement errors. Using the MISO method, strain can be measured only at a certain point taking into account that the critical strain is location-dependent. The purpose of the present study is to measure strain in close vicinity of the weld pool with the help of the DIC measurement technique during the hot cracking test.

The experimental arrangement used in this work is shown schematically in figure 33. In this work, the DIC technique is applied on the upper surface close to the weld to measure in situ transverse strain fields during laser welding. DIC is generally applied ex situ for welding-related measurements. In situ studies are hindered by the intense light emitted during welding, which renders observation close to the fusion boundary difficult [30]. There are only a few reported studies in which the in situ strains are measured during welding [30].

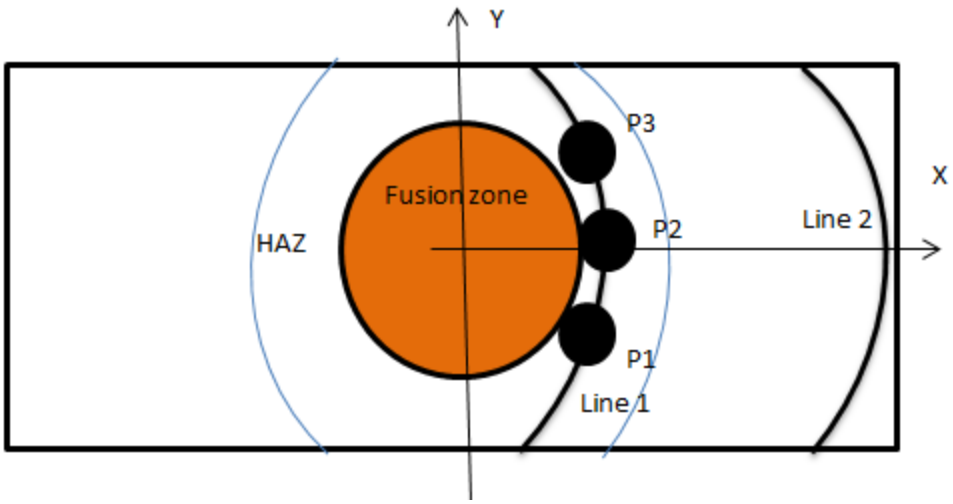

Figure 33 Locations for the extraction of DIC measurements. P1-3 represent points near the fusion zone of the spot weld. Line 1 shows the values in accordance to the mean values of the three points. Line 2 represents the contour value at the extreme end of the gauge length

In these study, displacement fields were measured along x direction from the weld centre of the sample. Similar experiments are conducted as standard tests to determine the hot cracking susceptibility of steels used in the automotive sector [37]. Random speckle patterns were applied on the top surface using a high-temperature commercial paint. The paint can withstand temperature up to 1100°C.

LIMESS Q-400-3D DIC system along with a commercial software package Istra 4D was used to capture and analyse images at a frame rate of 8Hz [37]. Image correlation on the specimen surface was conducted as the first step for the calibration of the DIC cameras using 10 images of a translated and rotated planar dot pattern of known spacing of 3 µm.

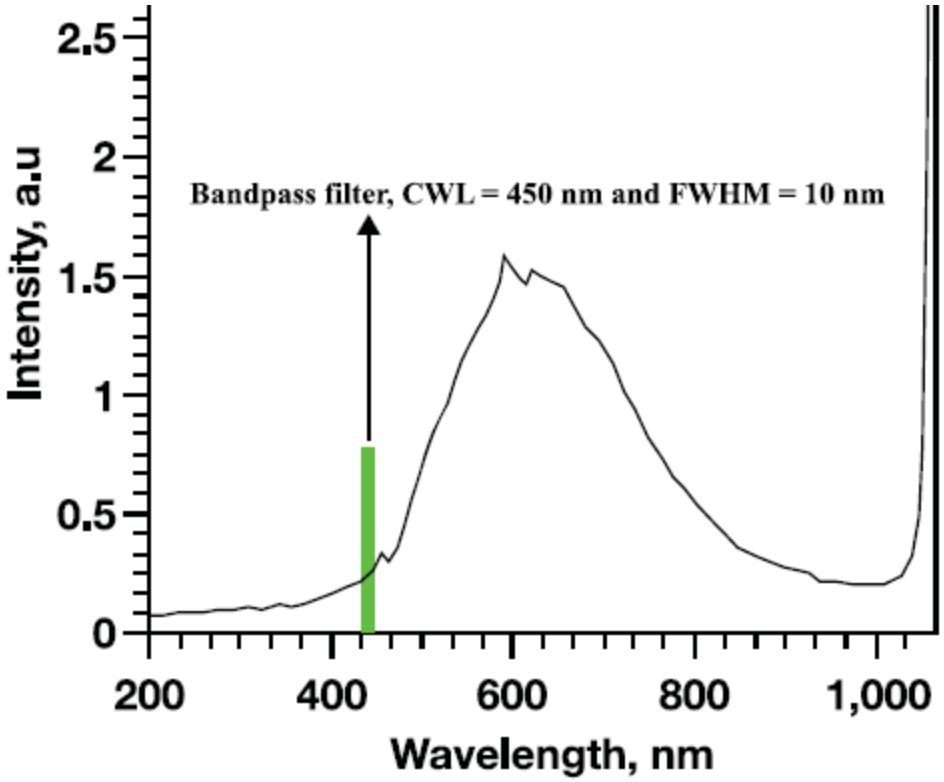

Figure 34 Emission spectrum of an Nd:YAG laser plume of an iron-based specimen [37]

To minimize the effect of intensity of laser plume light, an auxiliary high intensity 30W LED with a wavelength of 450 nm was used to illuminate the top surface of the specimen. Corresponding optical narrow bandpass filter with a centre wavelength of 450nm and full width half maxima (FWHM) of 10 nm was attached in front of the lenses to minimise the effect of plume light. This approach allowed measurement of displacement fields as close as 1.5-2mm from the fusion boundary. Figure 34 shows a typical emission spectrum of the laser plume of an iron-based specimen. To reduce any hindrance due to evaporation of metallic coating when the images were taken, a suction pump was attached with the load setup. Together with shielding gas and suction pump, the surrounding vapor was minimised.

3.4. Sample preparation after welding

The first step involved for the sample preparation was to cut out samples for embedding them in a resin. The welds from dog bone geometry were sheared out longitudinally in the dimensions of 30X12.7 mm rectangular samples. As all the welds were made twice, one from each of the samples was further sheared from the top transversely for cross-sectional inspection as shown in figure 35. Each sample was placed inside a mold with top surface on the top (side surface on the top for cross- sections).

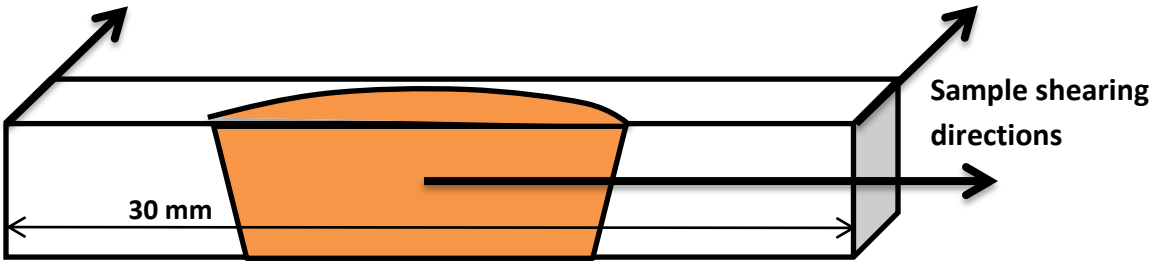

Figure 35 Schematic representation of weld pool (cross section)

For the next step, hot pressed mounts were made using thermosetting resin Polyfast at elevated temperatures. This was done to avoid porous, non-uniform mounts as it is important that the pressure is always constant and at the right level. The heating temperature was set at 180°C and a force of 25N with mounting duration (heating and cooling) of 8 mins.

These hardened mounts were further grinded and polished. The grinding began with the coarse SiC paper #180. All the scratches were allowed first to align in one direction before moving on to next grinding paper. The order of the papers used during grinding after #180 were #320, #400, #800, #1200 and #2000. The final paper managed to minimize the scratches upto a certain extent. After grinding, all the samples were cleaned using ethanol submerged in a sonic bath for 10 mins.

Next, the samples were polished to remove any possible scratches from the viewing surface. Polishing was conducted on both mol and nap polishing cloth loaded with diamond based abrasives in the form of liquid suspensions. The suspension sizes used in order were 3µm (mol) and 1 µm (nap). After every cycle of polishing, the samples were thoroughly washed under water to remove excess abrasives from the surface. The last step was to etch the samples for microscopy evaluation. Samples were etched using 2% nital.

3.5. Optical microscopy investigation

This inspection was performed in two ways. Firstly, before sample preparation all the welds were photographed at 3.15X magnification directly from the dog bone geometry to analyse the weld size as shown in figure. Both top and bottom part of the samples were photographed as all the welds turned out to be full penetrated.

After sample preparation, the samples were analysed using light optical microscopy. Keyence and Olympus BX-60M microscope were used with magnification ranging from 5X to 100X. Several photographs were taken to analyse cracking behavior and microstructural evolution.

3.6. Vickers hardness test

The hardness test was conducted on the cross sectioned samples at 10 positions as shown in figure 36. Here, 3 indentations were made on the fusion zone (FZ), 2 on heat affected zone (HAZ) and rest other on base material. The indenter was a diamond shaped pyramid which used 1 HV (Vickers Pyramid Number) of indenter load at a distance of 0.3mm between each indentation. Subsequently, all the hardness results were analysed under 60X magnification and data was exported for further study.

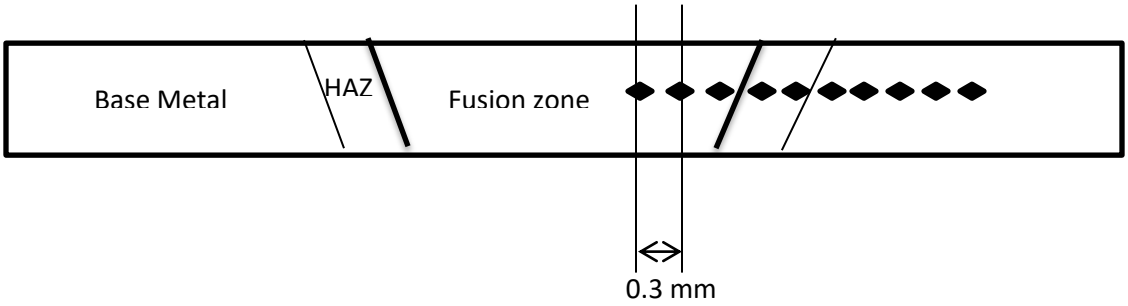

Figure 36 Schematic representation of positions of the indentations

3.7. Thermal modeling using COMSOL software

A finite element model was constructed using a commercial software COMSOL™ [30]. The heat balance during welding was simulated including the heat input, heat transfer and heat losses. The heat input was applied as a volumetric conical heat source with a Gaussian distribution.

The heat transfer in the sheet was governed by the temperature-dependent thermal properties as discussed in chapter 2. The latent heats due to phase transformations were included in the specific heat capacity as mentioned in section 3.2 of chapter 3. The heat loss was modeled by means of a surface film boundary condition. Ambient temperature T_0 was considered as a reference temperature.

For the finite element analysis, a model was designed using the material properties from DP 1000 and TRIP 700 steels as will be explained in the later sections. Owing to the steel's temperature dependent material properties, figure 30 was used to generate equations for thermal conductivity (K), specific heat (c) and density (ρ) with fitting curves for further analyses. The equations are

1. DP 1000

- $K = 3[exp[-25[T^9]]] - 3.2[exp[-21[T^8]]] + 1.5[exp[-17[T^7]]] - 4[exp[-14[T^6]]] + 6.5[exp[-11[T^5]]] - 6.6[exp[-8[T^4]]] + 4.3[exp[-5[T^3]]] - 0.017[T^2] + 3.5[T] - 2.8[exp2]$ 10W/mK

- $c = -3.6[exp[-22[T^8]]] + 2.9[exp[-18[T^7]]] - 1[exp[-14[T^6]]] + 2[exp[-11[T^5]]] - 2.2[exp[-8[T^4]]] + 1.6[exp[-5[T^3]]] - 0.0065[T^2] + 1.4[T] - 1.3[exp2]$ KJ/kg K

- $\rho = -7.4[exp[-19[T^6]]] + 4.5[exp[-15[T^5]]] - 1.1[exp[-11[T^4]]] + 1.4[exp[-8[T^3]]] - 9.4[exp[-6[T^2]]] + 0.0027[T] + 7.6]$ 1000kg/m^3

2. TRIP 700

- $K = 2\left[exp[-19[T^9]]\right] - 2.7\left[exp[-25[T^8]]\right] + 0.8\left[exp[-16[T^7]]\right] - 3\left[exp[-18[T^6]]\right] + 5.7\left[exp\left[-8[T^5]\right]\right] - 4.2\left[exp[-6[T^4]]\right] + 3.1[exp[-8[T^3]]] - 0.07[T^2] + 3.5[T] - 1.9[exp2]$ 10W/mK

- $c = -3.3[exp[-22[T^8]]] + 3.1[exp[-18[T^7]]] - 1[exp[-14[T^6]]] + 1[exp[-11[T^5]]] - 2.5[exp[-8[T^4]]] + 1.3[exp[-5[T^3]]] - 0.0052[T^2] + 1.2[T] - 1.7[exp2]$ KJ/kg K

- $\rho = -7[exp[-19[T^6]]] + 3.8[exp[-15[T^5]]] - 1.2[exp[-11[T^4]]] + 1.4[exp[-8[T^3]]] - 9[exp[-6[T^2]]] + 0.001[T] + 5]$ 1000kg/m^3

By using COMSOL multiphysics, geometry was generated for the model as shown in figure 37. The material chosen was a blank material as pre-defined material properties were not available in the materials' library in the software. Thus by using equations presented, the temperature dependent properties were chosen for the material.

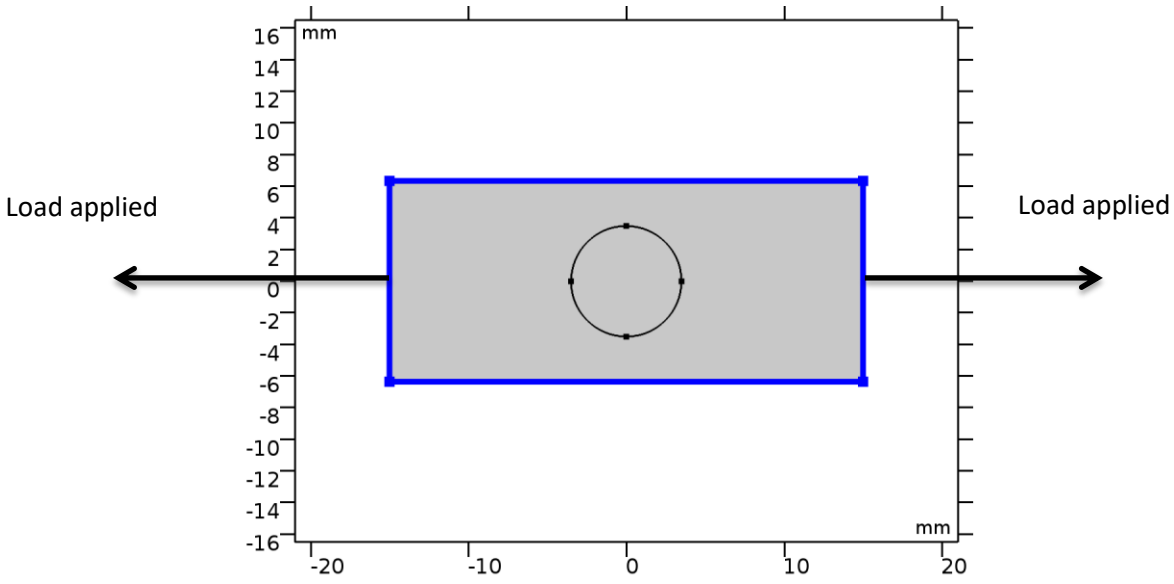

Figure 37 Geometry of the model. The circle represents the heat source per unit area which is conducted along the material. The dark blue edges represent the heat loss due to surface film boundary condition

As the laser beam impinging on the substrate material (workpiece) over a very short span of time, the workpiece is subjected to very rapid heating and cooling cycles. Each point in the spot weld experiences a thermal cycle which creates temperature profile. Temperature measurements are quite complicated by analytical modeling techniques. Therefore, the numerical model is an effective way to obtain these thermal cycles. Vice-versa, for all kind of temperature profiles, the thermal cycles in combination of laser input parameters (laser power) could be obtained.

Chapter 4 Results

This chapter details out the outcome of the experimental techniques which were used to assess the welds through recorded measurements during the welding cycle and light optical microscopy. This chapter includes the measured values from change in the applied global load and transient temperature measurements extracted by the attached thermocouple during welding. In addition, the digital image correlation recordings closest to the fusion zone of the weld pool till complete solidification were assessed to observe the possible behaviour of solidification cracking using the methodology as explained in section 3.4. The finite element simulation for the both the steels are also compared with the experimental observation. Lastly, a relationship was established between the observed transverse strains and the welding parameters distinguishing between the samples where the cracks were observed.

4.1. Light optical microscopy

The optical microscopy was carried out to determine the weld pool shape and the dimensions of the fusion and heat affected zones. Figure 38 and 39 represent the images of top and bottom surfaces with measured dimensions for the spot weld made at 1000 W at an applied load of 300 kg before sample preparation for both DP and TRIP steel respectively. For DP steel, at top and bottom surfaces, the diameters were 7.3 mm and 6.7 mm respectively. Similarly, figure 39 a and b represent the elliptical weld shape for TRIP steel at top and bottom surfaces with lengths at the minor axis as 8.2 mm and 7.1 mm respectively. The length of the major axis is 11.1 mm at the top surface.

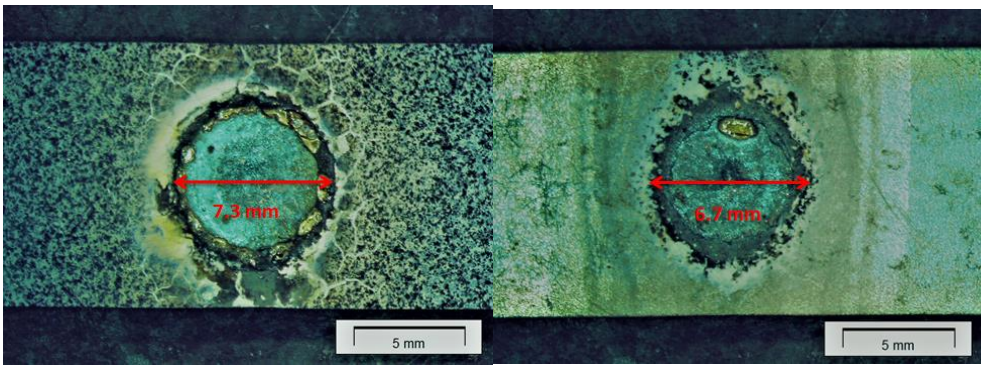

Fig 38 DP1000 weld (1000 W at an applied load of 300 kg) (a) top (b) bottom

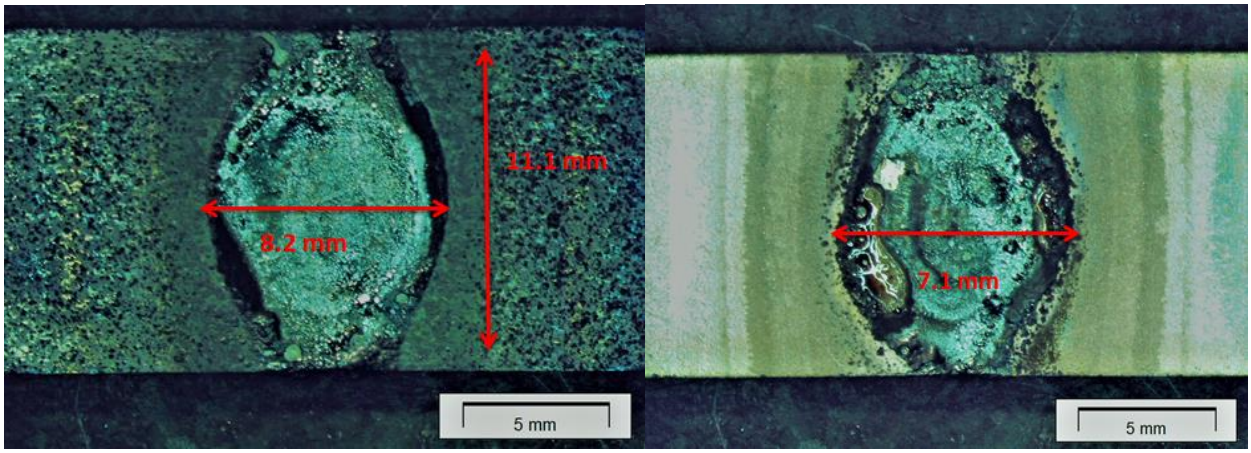

Fig 39 TRIP700 weld (1000 W at an applied load of 300 kg) (a) top (b) bottom

TRIP steel shows a considerably wider, elliptical weld pool shape both at the top and the bottom surface. Also, the HAZ is larger compared to DP steel. Due to surface contamination on the welded samples, the uncertainty in the determination of the dimensions of the spot welds is rather high. Therefore, the samples were ground and polished as explained in section 3.5. The diameters of the welds without sample preparation in the images are represented in the colour red. Even with surface contamination, it can be seen that the size of the welds for both the steels show a difference for the same welding conditions applied. Figure 40 represent the etched samples after sample preparation. These images give a clearer picture of the size of the fusion zone at the welding power of 1000 W and an applied load of 300 kg. Both DP and TRIP steel display vaporized crater at the centre with dimensions respectively evidencing loss of material, possibly due to excessive vaporisation when laser power is too high.

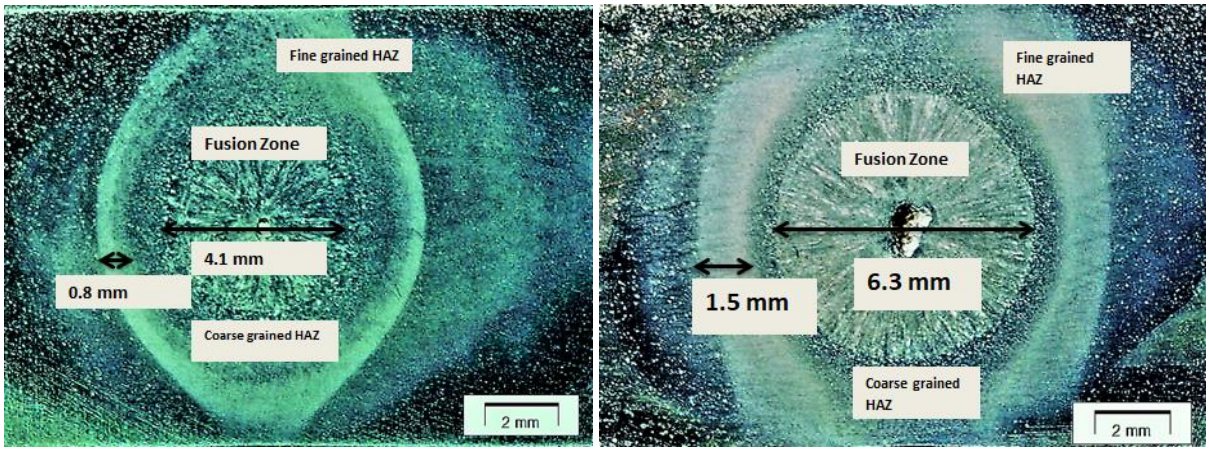

Fig 40 (a) Etched DP1000 weld (1000 W at an applied load of 300 kg) (b) TRIP 700 weld (1000 W at an applied load of 300 kg).

4.2. Variation in applied global tensile load

The global load measurements were carried out using a load setup as explained in section 3.2. As an example from the results obtained, figures 41 and 42 show the variation in the applied tensile load for the welds made using laser power for 700 and 800 W for DP 1000 and TRIP 700 welds respectively during the entire welding cycle.

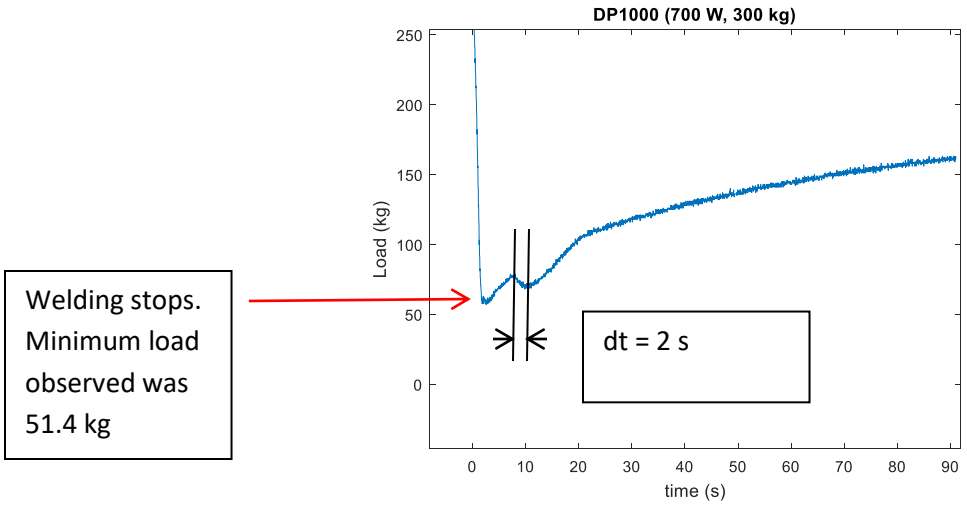

(a)

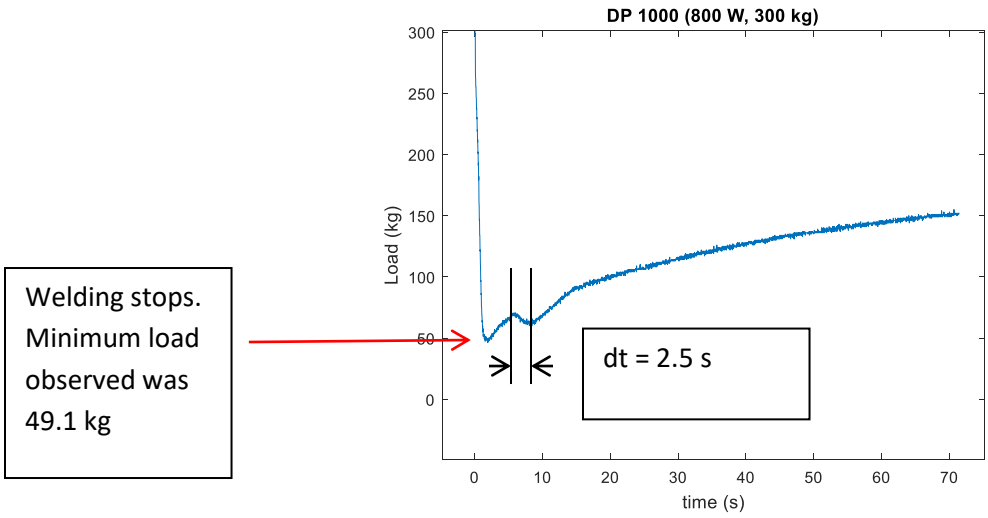

(b)

Fig 41 The measured load as a function of time (a) DP1000 weld made at laser power of 700 W and applied load of 300 kg(b) DP1000 weld made at a laser power of 800 W and applied load of 300 kg.

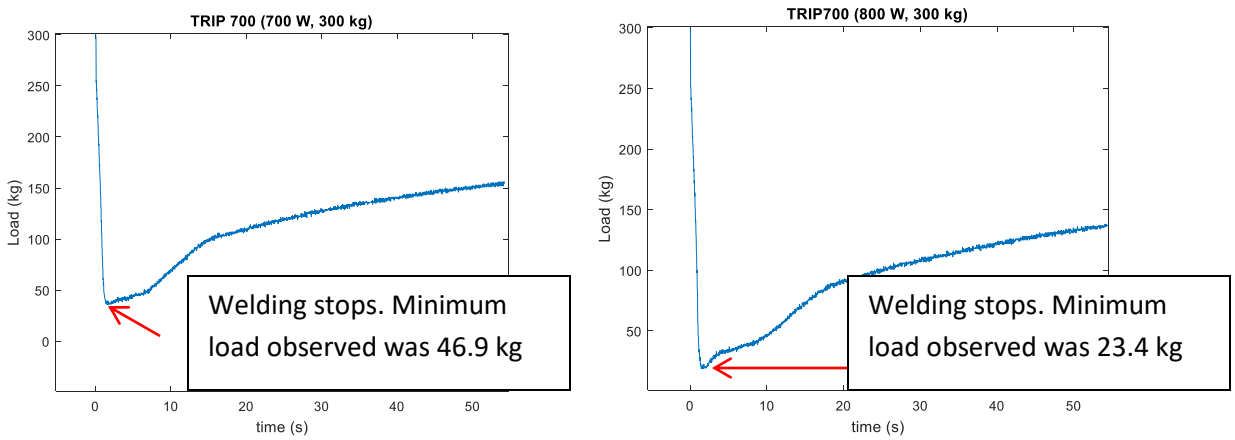

(a) **(b)**

Fig 42 The measured load as a function of time (a) TRIP 700 welds made at laser power of 700 W at an applied load of 300 kg (b) TRIP 700 welds made at laser power of 800 W at an applied load of 300 kg

The variation in the applied load of 300 kg for the entire weld cycle is represented in the figures. Referring to figure 41 a, at 700 W of laser power, the load drops to the value of 51.4 kg after 2 s, i.e., welding duration. After welding stops, a gradual increase in the load value can be seen . However, when the load reaches the value of 70.2 kg, a sharp reduction upto 63.4 kg at about 9.68 secs was observed, before increasing further. Similar observations were evident in all the DP steel welds.

The phenomena observed for DP steel were not exactly the same in TRIP steel as shown in figure 42 a and b. Although, there is a visible change in the slope of the load rate in the case of TRIP steels, no sharp reduction in load was seen the way it was prevalent in DP steels. For similar welding parameters, the reduction in the global applied load was higher in TRIP steel. The minimum values of the load observed were 46.9 and 23.4 kg for laser power of 700 W and 800 W respectively.

4.3. Transient temperature measurements

The transient temperature measurements from the thermocouples attached as explained in section 3.3.2 is represented in figure 43 a and b for DP and TRIP steel respectively. The welds chosen as an example here were made at laser power 1000 W and an applied load of 300 kg for both the steels. The peak temperatures recorded after welding of 2s, from the thermocouple attached at a distance of 10 mm from the weld centre on the top surface are 274°C and 328°C for DP and TRIP steels, respectively. However, temperature measurements were recorded with

attached thermocouples at both the top and bottom surfaces for these welds both at an axial distance of 10 mm from the y-axis as shown in figure 43. Figure 44 a and b represent the weld thermal cycle extracted from finite element simulation for DP and TRIP steel, respectively.

The difference in the recorded peak temperatures at the top (blue) and the bottom (red) surface is larger in TRIP steel. Cooling rate for DP and TRIP steel at a laser power of 1000 W obtained from models was approximately 40°C/s and 55°C/s, respectively.

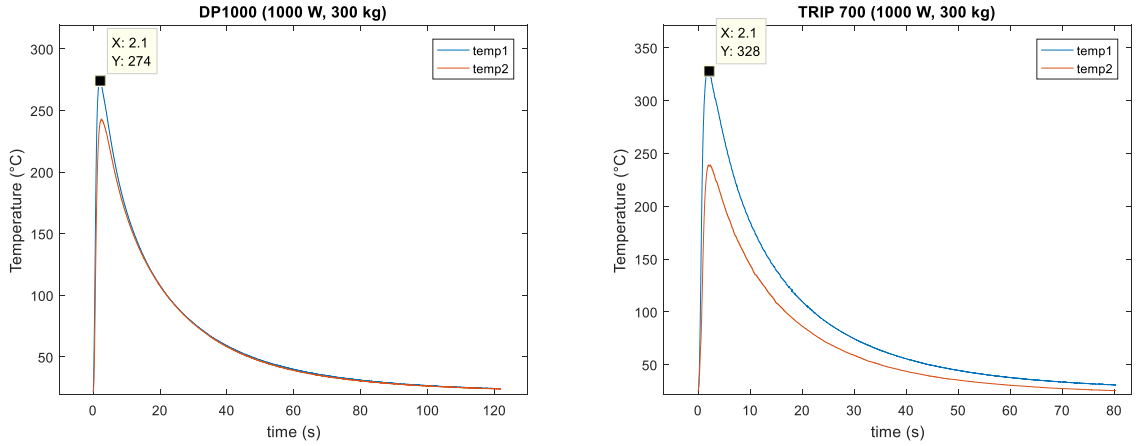

Fig 43 Transient temperature measurements from the attached thermocouples at the top (blue) and bottom surface (red) for (a) DP steel welded at 1000 W, 300kg (b) TRIP steel welded at 1000 W, 300 kg

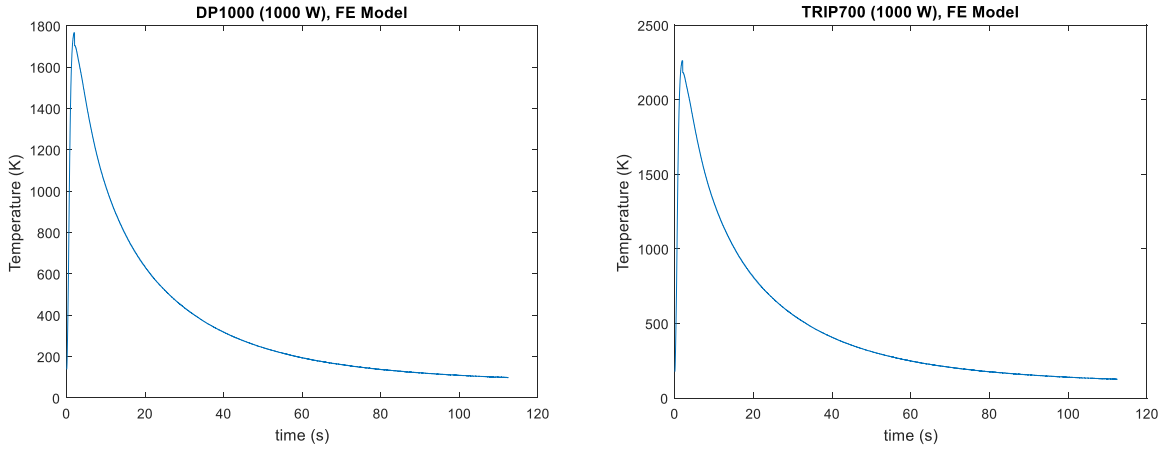

Fig 44 Transient temperature measurements from FE simulation (a) DP steel welded at 1000 W, 300kg (b) TRIP steel welded at 1000 W, 300 kg

4.4. DIC measurements

Figure 46 shows experimentally measured distribution of local displacements for DP steel weld made with laser power 700 W and an applied load of 300 kg at locations indicated in the figure 45. The locations P1, P2, P3 and Line 1 (L1) were chosen at a distance of 1 mm from the fusion boundary line to avoid possible data distortion caused by fume and spatter. However, due to the optical filtering of the intense laser plume light, a good spatial resolution close to the fusion boundary is achieved. Furthermore, location Line 2 (L2) was chosen at a distance of 5 mm from the fusion boundary line. The recorded displacement measurements are represented with respect to both x and y axis with the function of time. For the reference, the tensile load was applied on the welds along the x-axis.

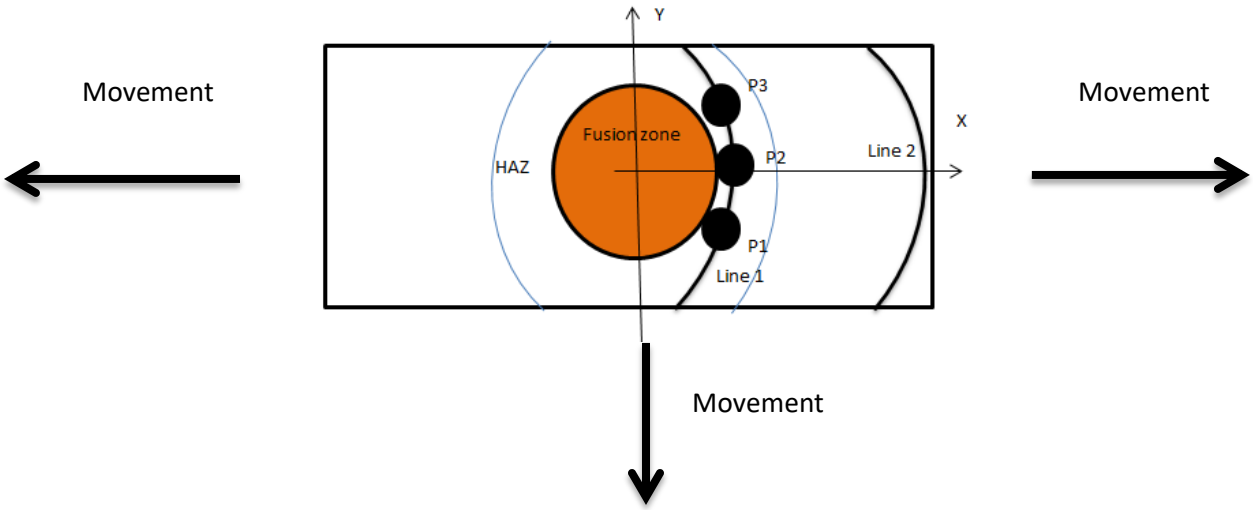

Fig 45 Schematic representation of locations for DIC measurements

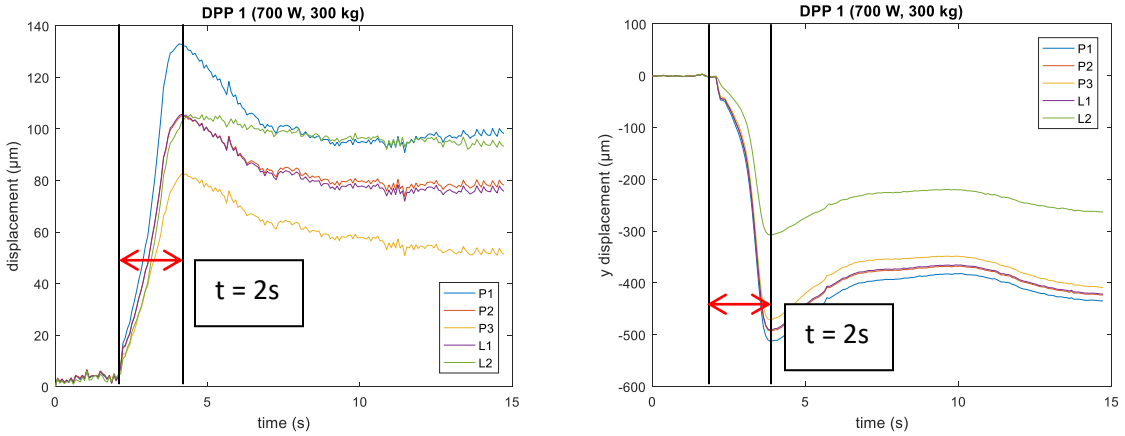

Fig 46 Displacement measurements as a function of time for (a) x-axis (b) y-axis

Peak displacements for all the locations in both the directions are attained at 2 s after the start of the welding, i.e., the welding duration. Point P1 showed maximum displacement on both x and y axis with the minimum being at location L2. Conventionally, all the locations should show same displacement gradients with the function of time along x-axis without any possible movements in the y-direction due to the application of tensile load. However, the thermal load produced by the laser source along the z-axis on top of the sample was not aligned along the weld center during experimentation. It induced an additional force along the negative y-direction and subsequently errors in the measurements. For this reason, to study solidification behaviour, mean transverse strains were extracted of a contour field closest to the fusion boundary line for all the spot welds. Figure 45 schematically represents the movement of the sample during welding, which was responsible for the error in the displacement measurements.

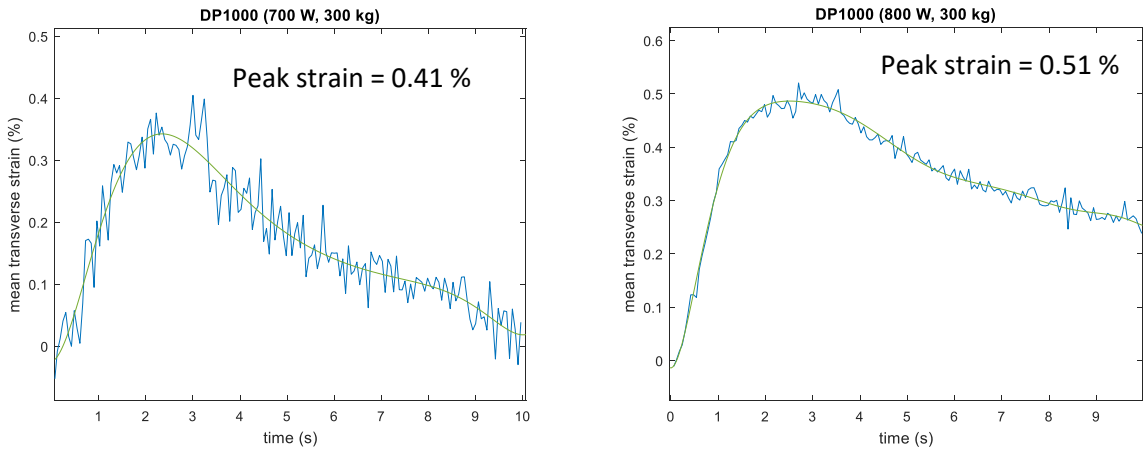

Fig 47 Mean transverse strain for DP 1000 weld at applied load of 300 kg and laser power of (a) 700 W (b) 800 W

As an example, the mean transverse strain recorded for welds made at laser powers of 700 and 800 W with an applied load of 300 kg for both the steels are displayed in figure 47 a and b. Both the steels experienced only elasticity at the applied load of 300 kg. Therefore, elastic strain has been included in the graph due to pre-loading conditions. The mean transverse gradient for these welds thus, represent the total strain experienced by the contour field on the sample in the entire welding cycle.

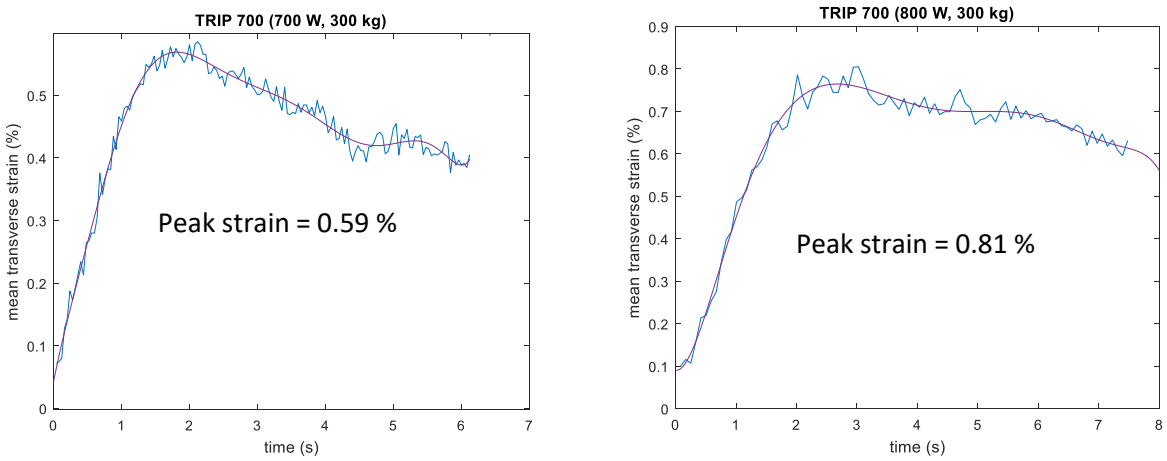

Fig 48 Mean transverse strain for TRIP 700 weld at applied load of 300 kg and laser power of (a) 700 W (b) 800 W

4.5. Weld hardness

Figure 49 shows the characteristic weld hardness distributions in DP and TRIP steel. In DP steel weld, the average of maximum hardness which was achieved in fusion zone was 340±20 HV and represents 1.72 times of DP steel base metal hardness. For TRIP steel weld, the average of maximum hardness which is present in fusion zone was 500±20 HV and represents 1.89 times of TRIP steel base metal hardness as seen in figure 49.

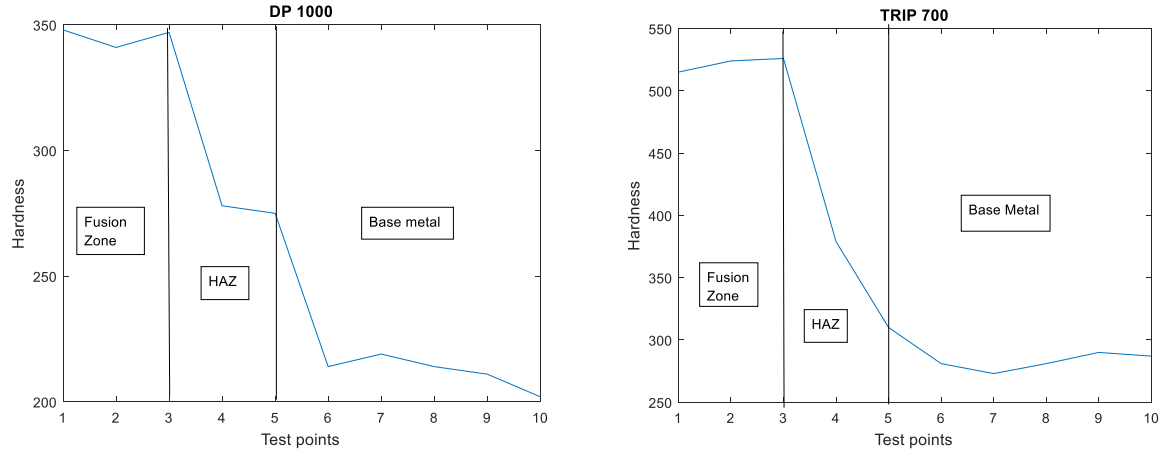

Figure 49 Vickerrs hardness measurement (a) DP 1000 (b) TRIP 700

4.6. Finite element simulation from COMSOL

In order to understand, how the laser heat is dissipated on the top surface of the sample in accordance to conduction, convection and radiation, a finite element simulation was conducted using the software COMSOL. As explained, both the materials exhibit temperature dependent properties and the model was designed accordingly. The experimental results and the simulation are in good agreement with the weld pool shapes on the top surface for the both the steels as seen in figure 51 and 52. Figure 51 and 52 represents the combination of simulations with their prepared etched samples at the welding conditions of 1000 W laser power at the applied load of 300 kg. Although, simulations do not predict the actual size of the fusion and the heat affected zone, it gives an idea about the heat transfer after the welding and validates the temperature measurements extracted to thermocouple at a distance of 10 mm from the weld centre. The peak temperatures observed after 2s at the top surface were 253°C and 311°C for DP and TRIP steel respectively. The experimental values are 7.6 % and 5.1 % higher for DP and TRIP steel respectively.

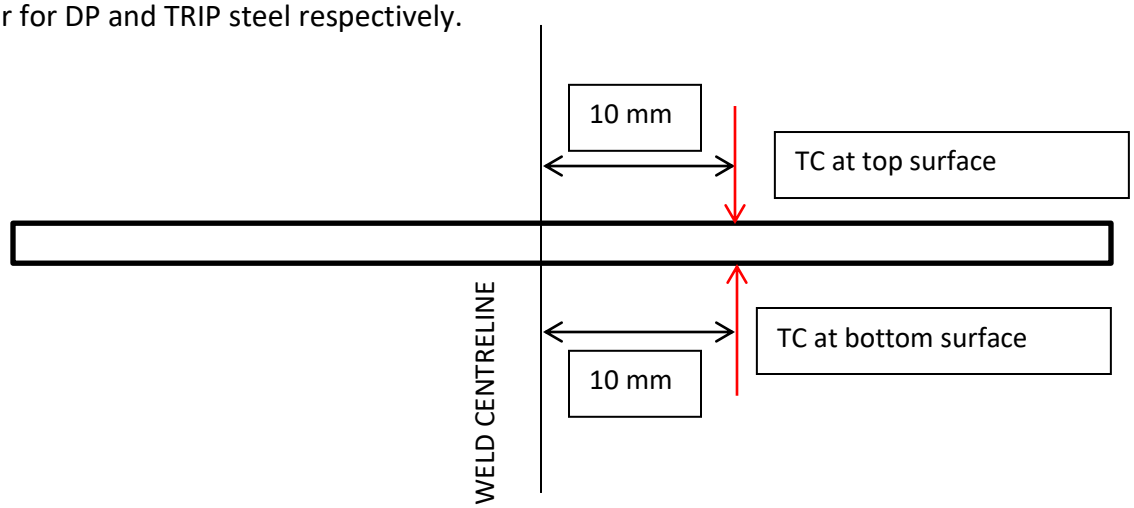

Figure 50 Schematic representation of positions of attached thermocouple

Contour plots depict the temperature ranges along the sample at the top surface after welding stops at 2s. The area upto which the material was subjected to the liquidus temperature is depicted as the region inside the bold yellow boundary pool. The temperature at the centre of the weld reached by the weld pool in DP steel was around 1700 K, while weld pool in TRIP steel showed 2400 K in the simulation. The semi-circular region (bold black) represented in the simulation images was the area of the laser pilot selected for the experimentation with the focal length of 195 mm. The vaporised crater cannot be predicted through the simulations since analysis of the vapour phase is not considered.

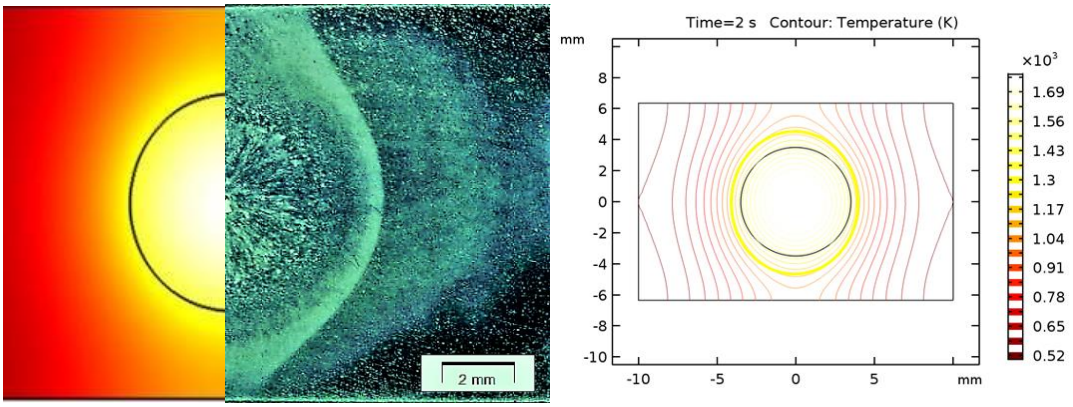

Fig 51 Representation of simulation with contour plot for DP 1000

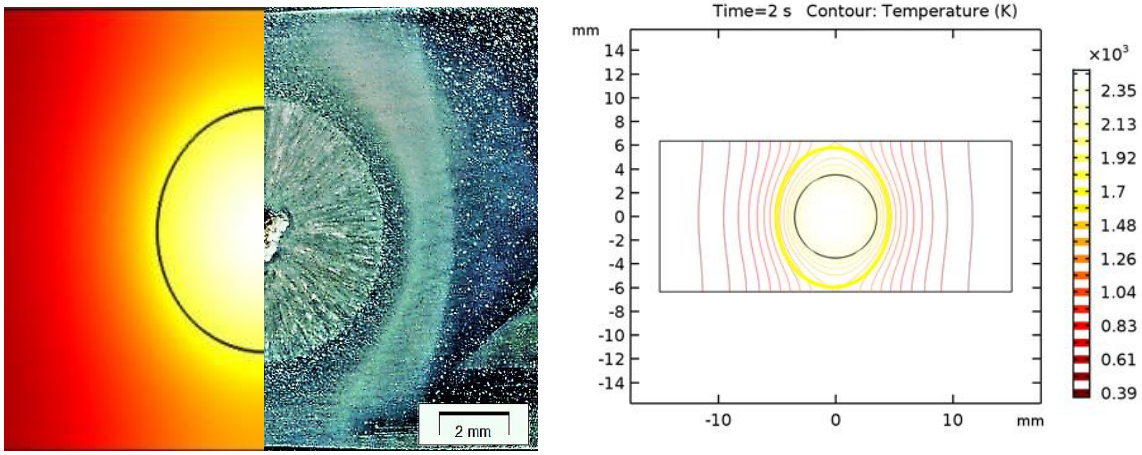

Fig 52 Representation of simulation with contour plot for TRIP 700

4.5. Cracking behaviour

In this section, the cracking behaviour is analysed for all the welds at variable welding parameters (laser power and applied load). Figure 53 represent the cracks which were observed on the top and cross-sectional surface for TRIP700 weld made with laser power at an applied load of 600 kg. This sample had a similar vaporized crater as seen in figure 41. All the welds had cracks inside the crater irrespective of the fact where they had vaporized crater or not. For this sample, the mean transverse strain obtained closest to the fusion boundary line is represented in figure 54. Maximum strain observed was 1.13 %. The crack length at the cross sectioned was 0.47 mm.

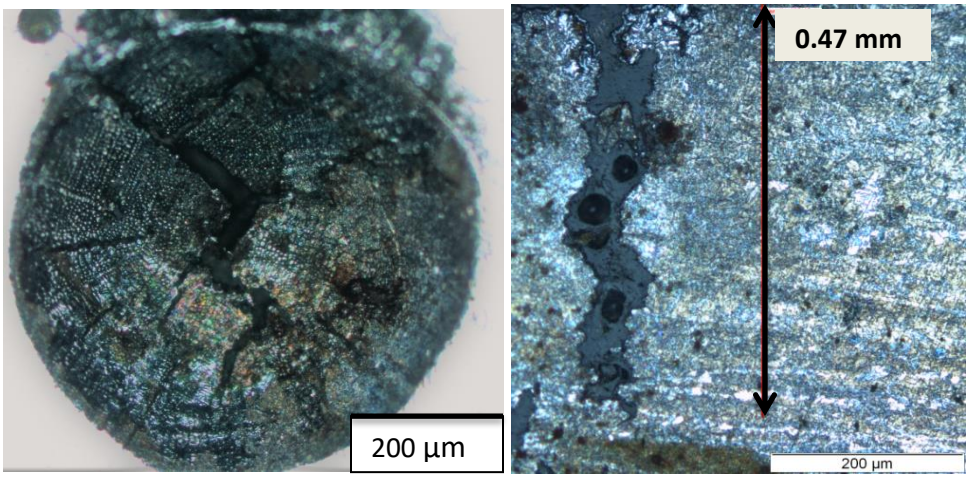

Fig 53 TRIP700 welded at laser power of 1000 W at an applied load of 600 kg. Top (left) and cross sectional surface (right)

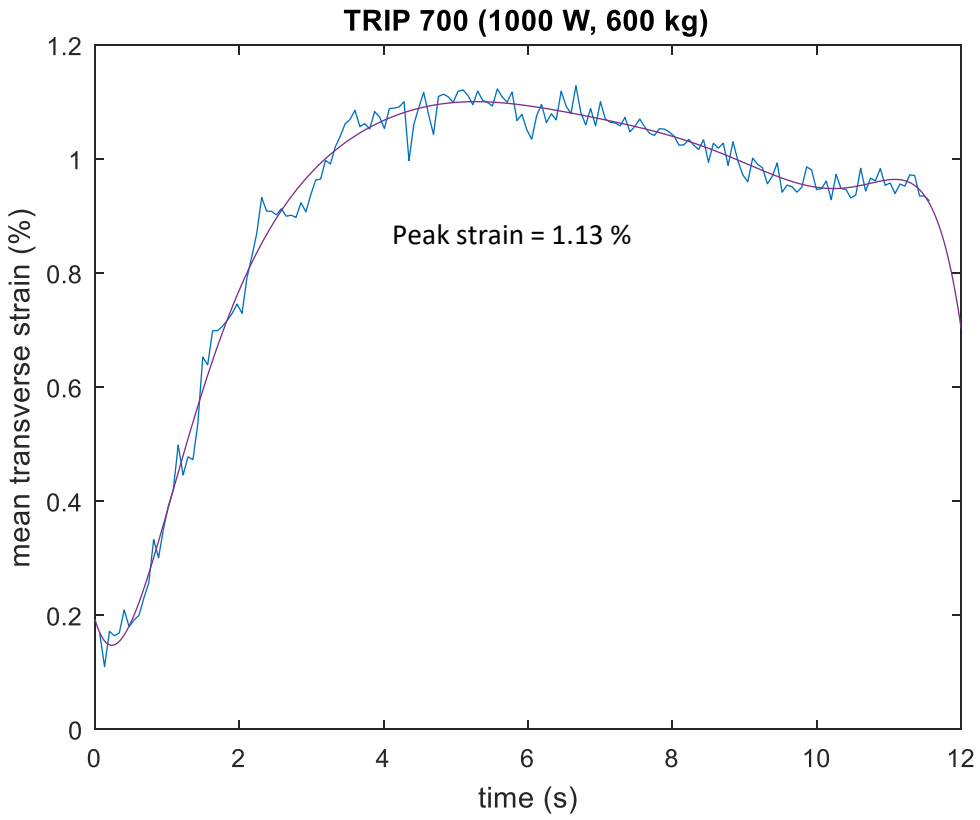

Fig 54 Mean transverse strain observed for TRIP 700 welded at laser power 1000 W at an applied load of 600 kg

For TRIP steel welds, cracks were observed at laser power higher than 1000 W at the applied load higher than 300 kg. No cracks were observed with either of the welding parameter being lesser than the mentioned. Figure 55 display the similar crack inside a vaporized crater observed at top surface of the TRIP 700 weld made at laser power 1000 W at an applied load of 300 kg. The crack length observed was 0.8 mm.

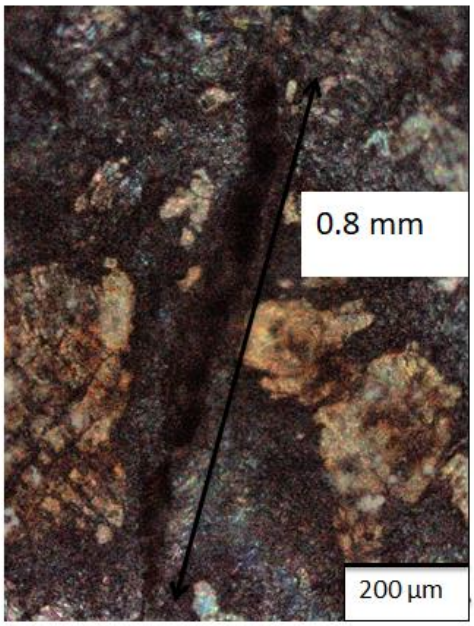

Fig 55 TRIP700 welded at laser power of 1000 W at an applied load of 300 kg

In case of DP steel welds, only a single crack was observed. The cracked weld was made at a laser power of 1000 W and 600 kg as shown in figure 56. Observed crack length was 0.41 mm. No cracks were observed for welds made using load less than 600 kg. However, the applied load less than 600 kg in which experiment was conducted was 450 kg. No cracks were observed at the load of 450 kg. Therefore, there lies a region of uncertainty between the applied loads of 450 and 600 kg at laser power of 1000 W. Similarly in case of TRIP steels, the load less than 300 kg at laser power of 1000 W (observed crack), was 150 kg where weld was made and thus, lies the similar region where experimentation was not conducted. Figure 58 and 59 summarise the crack mapping as a function of peak transverse strain observed for all the welds.

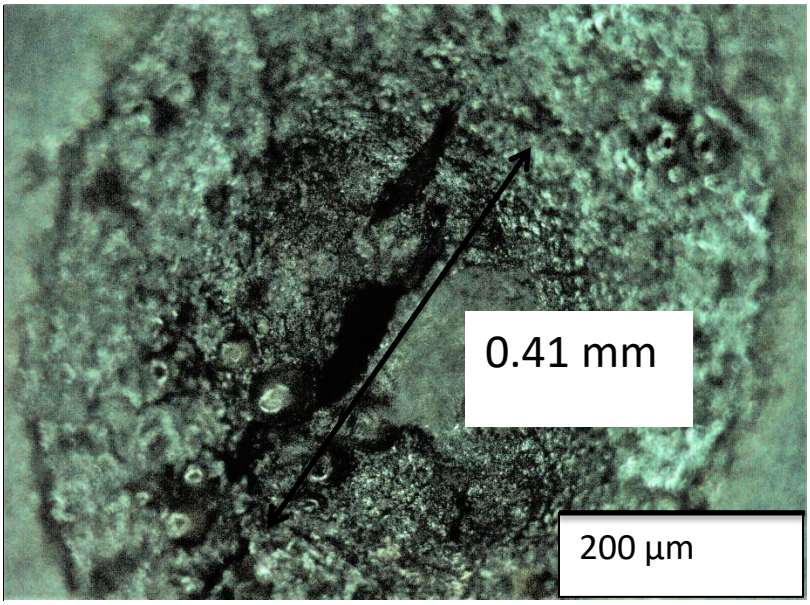

Fig 56 52 DP 1000 welded at laser power of 1000 W at an applied load of 600 kg

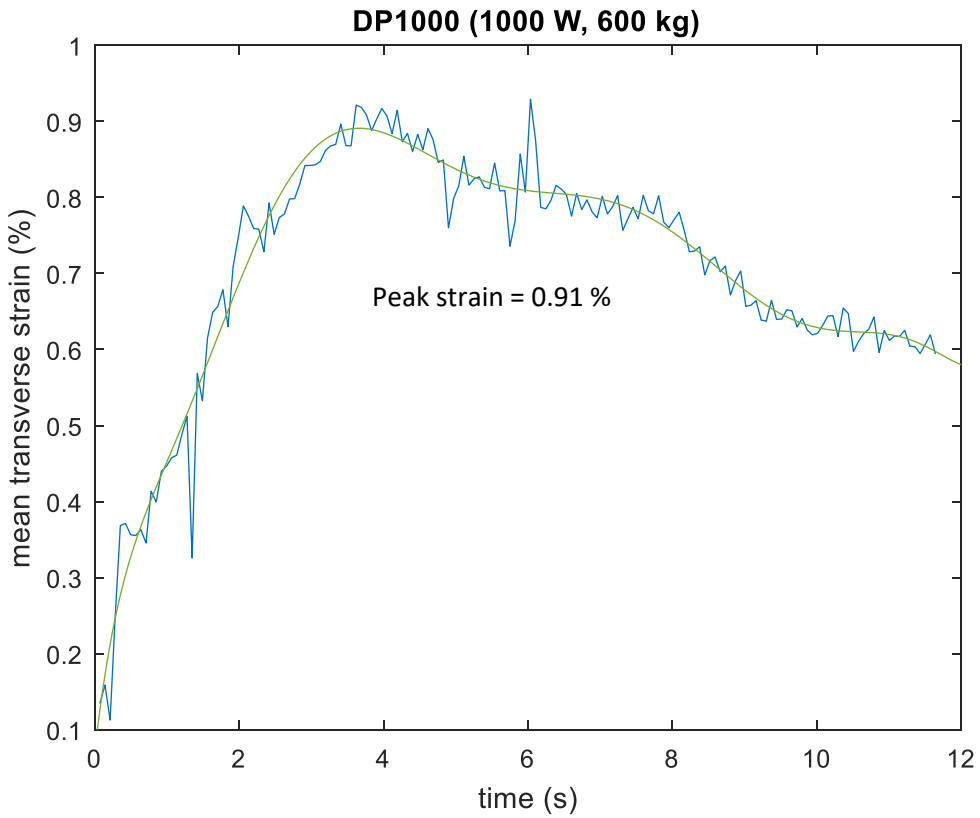

Fig 57 Mean transverse strain observed for DP 1000 welded at laser power 1000 W at an applied load of 600 kg

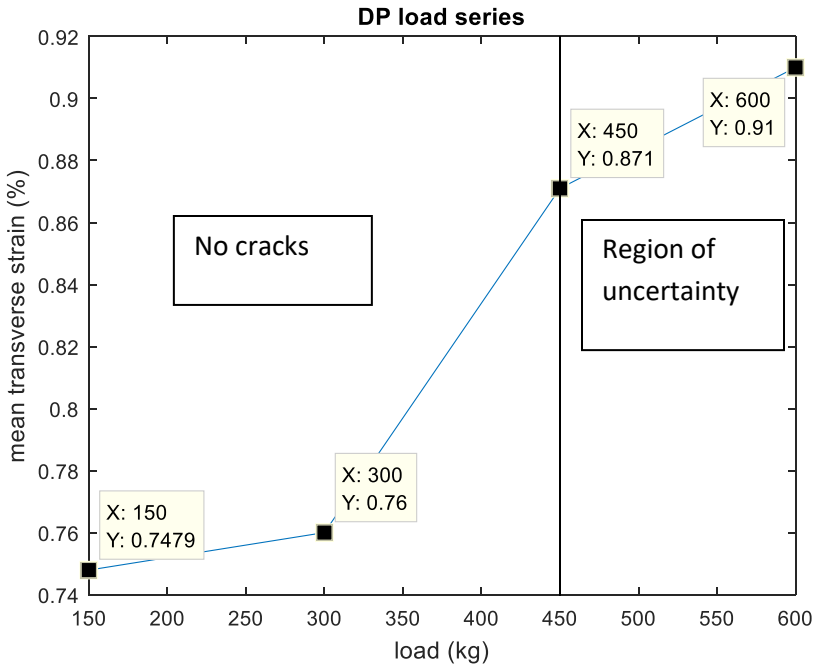

Fig 58 Crack mapping for DP 1000

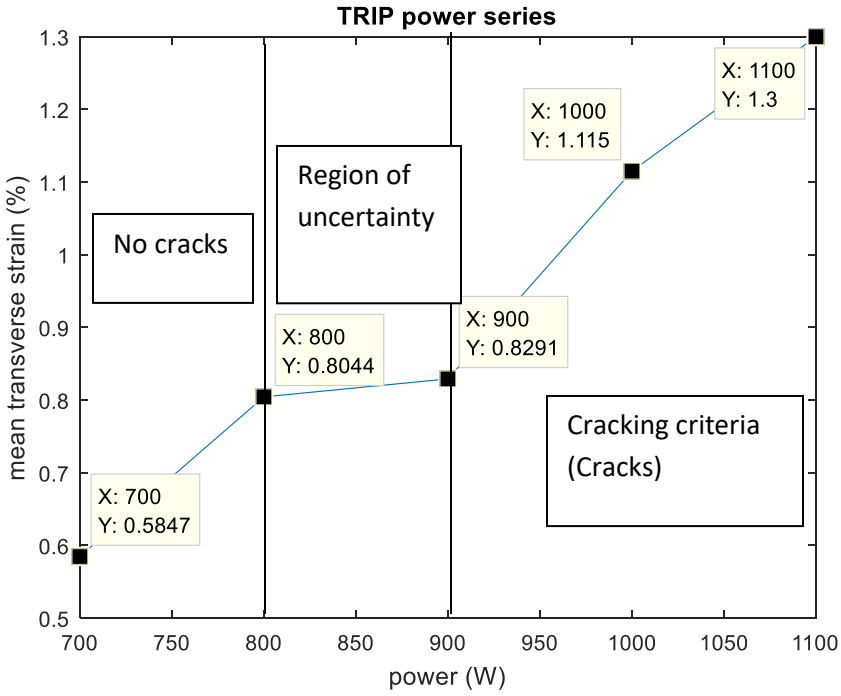

Fig 59 Crack mapping for TRIP 1000

4.6. DP and TRIP bead on plate welding

Bead-on-plate welding experiments were performed both the materials using Nd:YAG laser with a power of 1000W and welding speed of 10mm s^{-1} for a comparison point of view with the spot welds. The constraining condition was same throughout, i.e., external load of 300 kg.

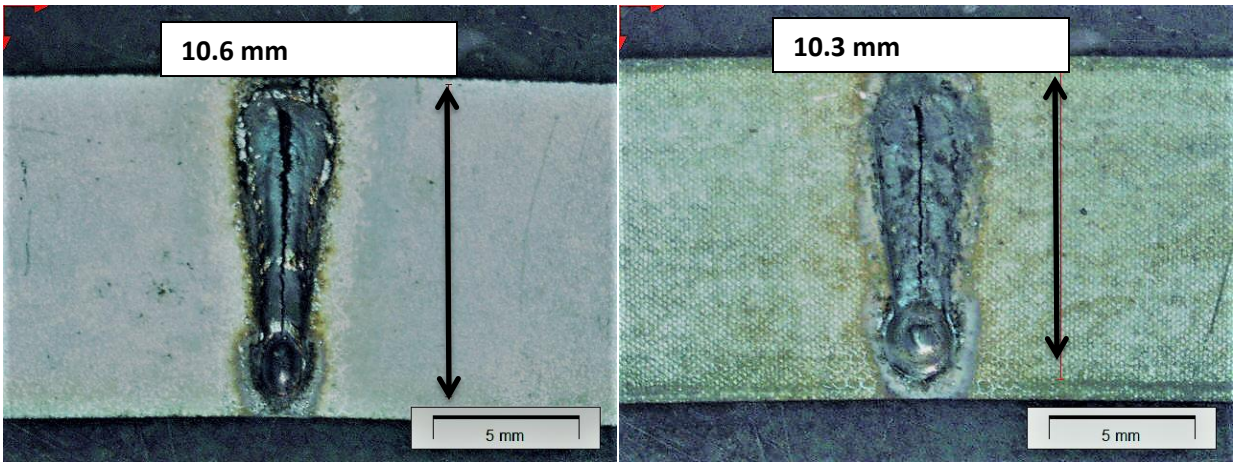

Fig 60 TRIP 700 (left) and DP 1000 (right)

From figure 60, one can observe that the weld pool formation in TRIP steel is visible as more elongated tear drop shape. The crack is wider in TRIP steel, which shows possibility of higher transverse displacement (in sync with tensile load direction). Previous work has verified that the crack was observed along the weld centre line in TRIP steel with same laser parameters, whereas for the DP samples, no cracks were detected [37]. In this experiment, the changes in additional parameters applied for DP steel was the constraining condition, i.e., a load of 300 kg and sample geometry. No cracks were observed on the DP samples with application of load less than 300 kg.

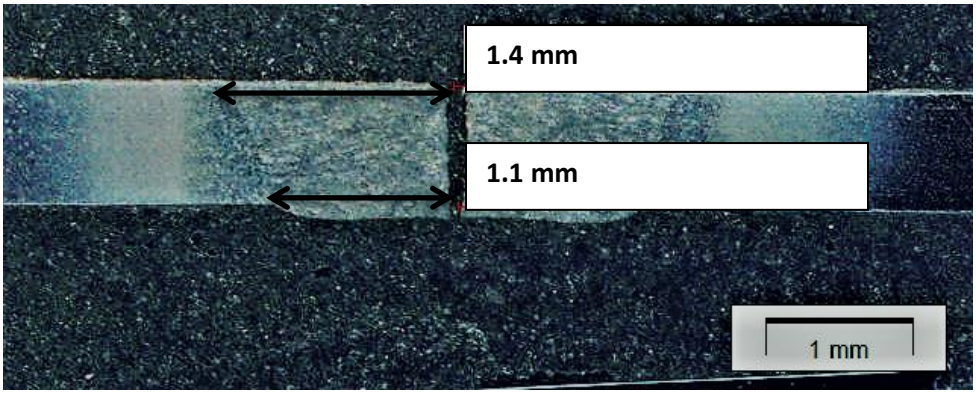

Fig 61 Cross sectioned sample of TRIP 700

Chapter 5 Discussion

In this chapter, based on the theoretical background, the experimental procedures and the results that have been mentioned in the chapter 3 and 4 respectively, hot cracking behaviour of spot welded DP and TRIP steels will be discussed. In addition, as a brief introduction of solidification behaviour on alloys have already been discussed in the section, therefore, the possible changes in mechanical properties during solidification after welding for both DP and TRIP steel will be discussed.

This chapter will discuss in detail the observed results with justification based on available theoretical background. The sections for this chapter are divided into three categories, namely in order, spot weld characterization including macro and microstructure, applied global load variation in DP steel and solidification behaviour with respect to total strain observed through DIC measurements for spot welds made on DP and TRIP steel.

5.1. Spot weld characterization

This section will elaborate the processing conditions on the formation of the weld pool and the microstructural characterisation of the spot welded samples. Macrostructural characterization will explain the possible theoretical reasoning behind the size of the weld pool correlating with the finite element simulation, while, microstructural characterization will correlate the literature for the spot welded samples at a microstructural level (directional solidification, solute inclusions etc.).

5.1.1. Macrostructure

As it was already discussed in section 4.1, the first observation on the welds was made through light optical microscopy. Figures 62-63 and 65-66 represent the geometrical aspects of the spot welds made on DP and TRIP steel respectively. Spot welds made at laser power of 700 W with applied load of 300 kg is displayed by figure 62 and 65 for DP and TRIP steel respectively, while, figure 63 and 66 represent spot welds made at laser power of 1100 W with applied load of 300 kg for DP and TRIP steel respectively. The difference in the dimensions is clearly observed for the weld pools in comparison to both the steels at top and bottom surface. Considering each of the steels, no significant difference in the size of the weld pool was observed at constant laser power and varying tensile load as mechanical energy provides no thermal energy to achieve the

weld pool size. Therefore, the discussion focuses on the explanation for weld pool sizes changes with varying laser power/heat input when the load was varies while the laser power was kept constant. As the laser power/heat input increased, weld pool sizes on top and bottom surface also increased. All the spot welds made using the welding parameters mentioned in table 3-6 were fully penetrated.

As mentioned in section 4.1, due to surface contamination, there was an uncertainty in the determination of dimension of the fusion zone. To get a clear picture, the samples were ground and polished. However, there would be possibility of an error during sample preparation, i.e., the extent to which the samples were ground (decrease in depth). Therefore, the images obtained from DIC camera would give us the information of the size of the fusion zone as shown in figure 68 and 69. Growth rate from the time solidification starts could be obtained from the measurements of the radius (columnar grains) of the weld pool and time to completely solidify. Table 8 and 9 summarises the size of the fusion zone and the growth rate of the columnar grains for each weld obtained at constant load and varying laser power.

Table 8 DP 1000

Laser Power (W)	Fusion zone diameter (mm)	Time to solidify (s)	Growth rate/R (mm/s)
700	4	4.1	0.48
800	4.5	4.3	0.52
900	5	4.5	0.55
1000	5.5	4.8	0.57
1100	6	5.2	0.57

Table 9 TRIP 700

Laser Power (W)	Fusion zone diameter (mm)	Time to solidify (s)	Growth rate/R (mm/s)
700	5	4.3	0.59
800	5.7	4.6	0.61
900	6.6	4.8	0.63
1000	7.3	5.3	0.66
1100	8	5.5	0.7

The simplest explanation for heat transfer from the laser source considers heat conduction equation, which can be written in its general form as [37]

$$\frac{\partial T}{\partial t} - \propto \nabla^2 T$$

,where α is the thermal diffusivity which is described by $\alpha = k/(\rho c_p)$, k is the thermal conductivity, ρ is the specific mass density and c_p is the specific heat. T(x,y,z,t) describes the temperature field as a function of space and time. It is well known that thermal diffusivity measures the rate of transfer of heat of a material from the hot side to the cold side. In a substance with high thermal diffusivity, heat moves rapidly through it because the substance conducts heat quickly [45]. The temperature-dependent thermal properties, i.e. density, conductivity and specific heat capacity based on the chemical composition of DP and TRIP steel were mentioned in figure 30. It was observed that DP steel has a consistently higher density than TRIP steel. The heat conductivity of DP steels is larger than that of TRIP steel below 1000 K, and becomes similar above 1000 K. The specific heat capacity of the two steels is similar until the solidus temperature, although, TRIP steel shows a slightly higher specific heat capacity due to the latent heat during the solid–liquid phase transformation [45]. Overall, it was determined that TRIP steel exhibit higher thermal diffusivity than DP steel.

Therefore, TRIP steel has a wider weld pool at the top and bottom surfaces as heat diffusion was higher compared to DP steel. The thermal recordings from the attached thermocouples as shown in figure 64 and 67, also support the fact that at same welding heat input, it can be expected that TRIP steel would have wider weld pools. Figure 70 represent the finite simulation recordings identifying the melt pool after 2s. The models also confirm that TRIP steel will have a wider pool.

Comparing each of the steels with respect to the applied heat input/ laser power, transition from conduction to keyhole mode of welding is possible. Buvanashekaran et al. showed that depending on the power density, different welding regimes/modes occur in laser processing, identified as keyhole and conduction [45]. Conduction regime is controlled by the power density. In the conduction regime, there is a certain minimum power density required to achieve melting. Keyhole regime is a vaporization driven process and hence the power density plays the most important role. The temperature distribution in the material depends on heat input and heat losses. This heat balance can predict the extent of melting.

According to Assuncao et al. there is a narrow window where pure conduction regime can be achieved, which depends on the power density and spot size [45]. The keyhole regime has high aspect ratio weld profiles (penetration depth to weld width) in comparison to conduction mode. However, the vaporisation, which is the inherent feature of the keyhole regime, increases the likelihood of defects. In the conduction regime no vaporisation should occur and the energy is transferred to the material from the surface via conduction, which results in a more stable melt pool and better surface finish. Both DP and TRIP steel had vaporized craters at

an applied laser power of 1000 W or more, exhibiting the keyhole mode. In the finite element models, conduction mode of welding was applied. Therefore the computed models only represent the temperature profile but do not predict vaporization. However, vaporisation was observed in experimental results.

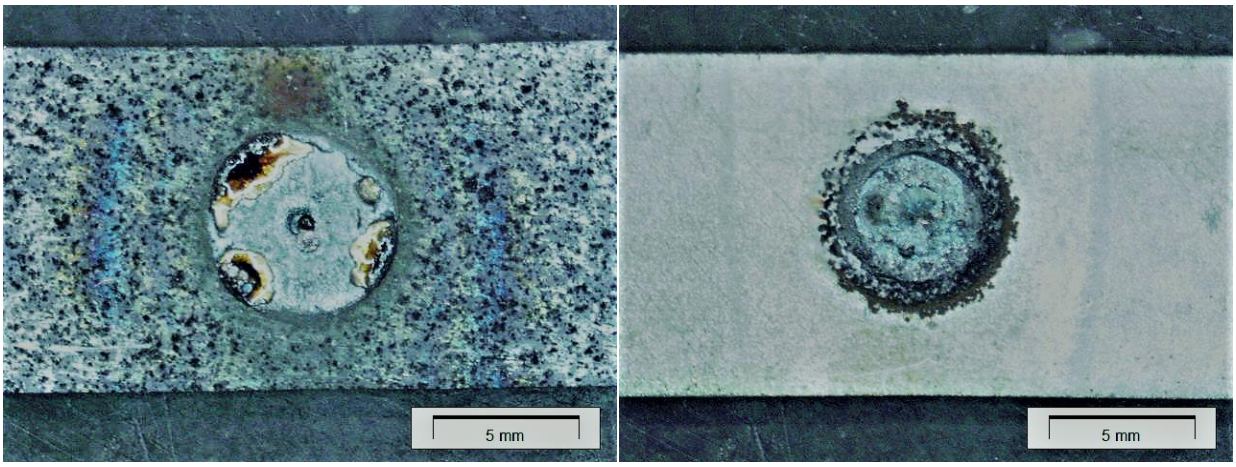

Figure 62 DP 1000 (700 W, 300 kg) (a) top (b) bottom

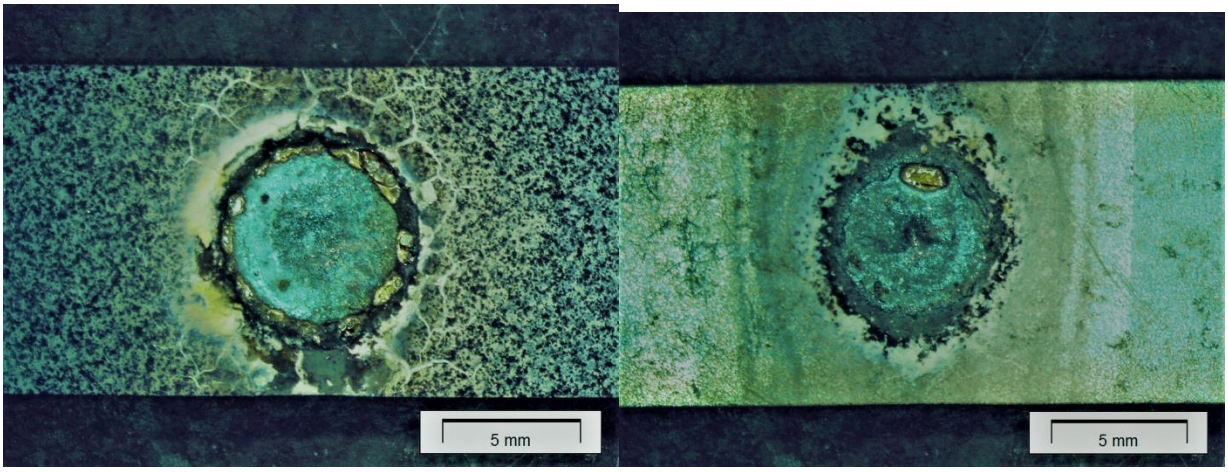

Figure 63 DP 1000 (1100 W, 300 kg) (a) top (b) bottom

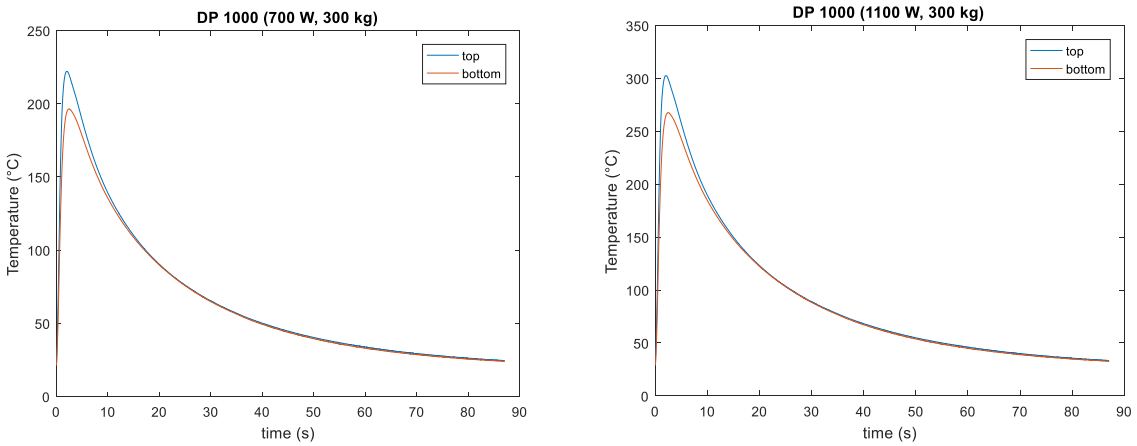

Figure 64 DP 1000 temperature recordings at top and bottom surface (a) at 700 W, 300 kg (b) at 1100 W, 300 kg

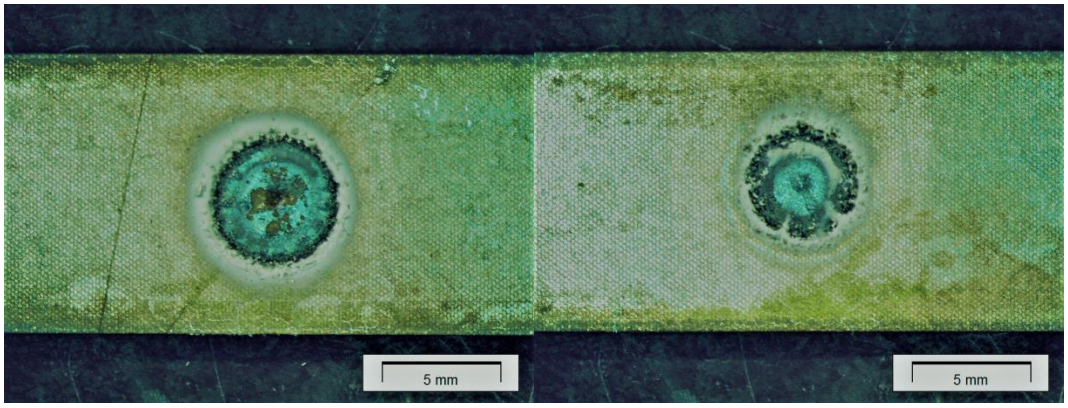

Figure 65 TRIP 700 (700 W, 300 kg) (a) top (b) bottom

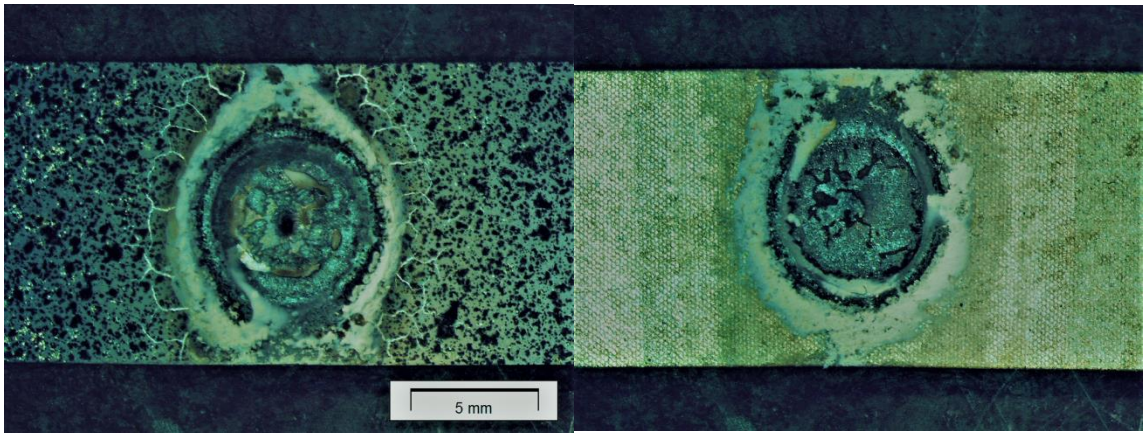

Figure 66 TRIP 700 (1100 W, 300 kg) (a) top (b) bottom

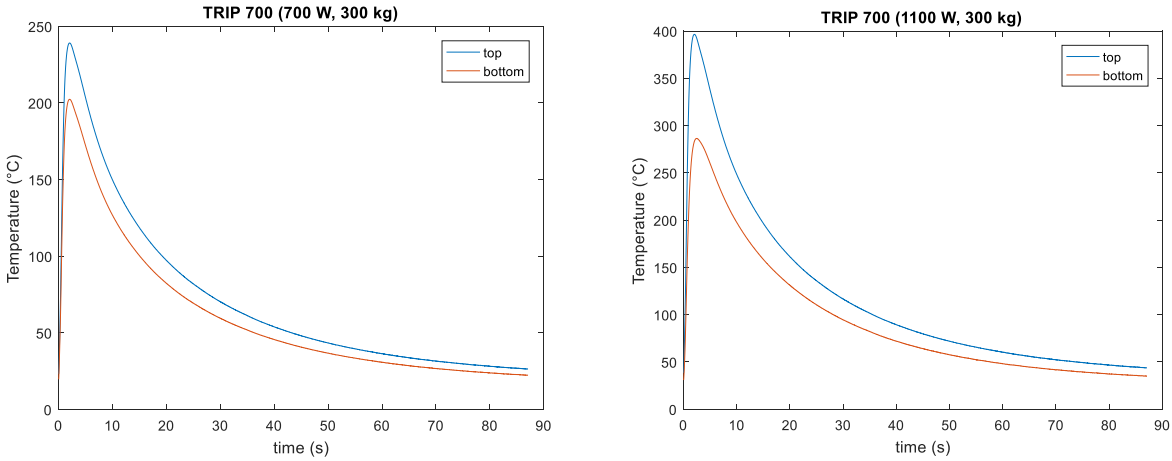

Figure 67 TRIP 700 temperature recordings at top and bottom surface (a) at 700 W, 300 kg (b) at 1100 W, 300 kg

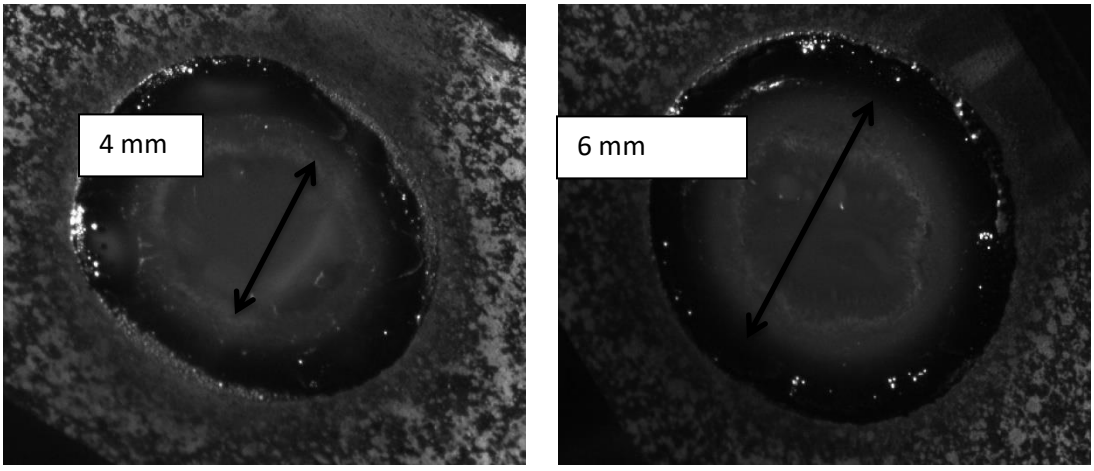

Figure 68 Dimensions of fusion zone DP 1000 welded at (a) 700 W (b) 1100 W

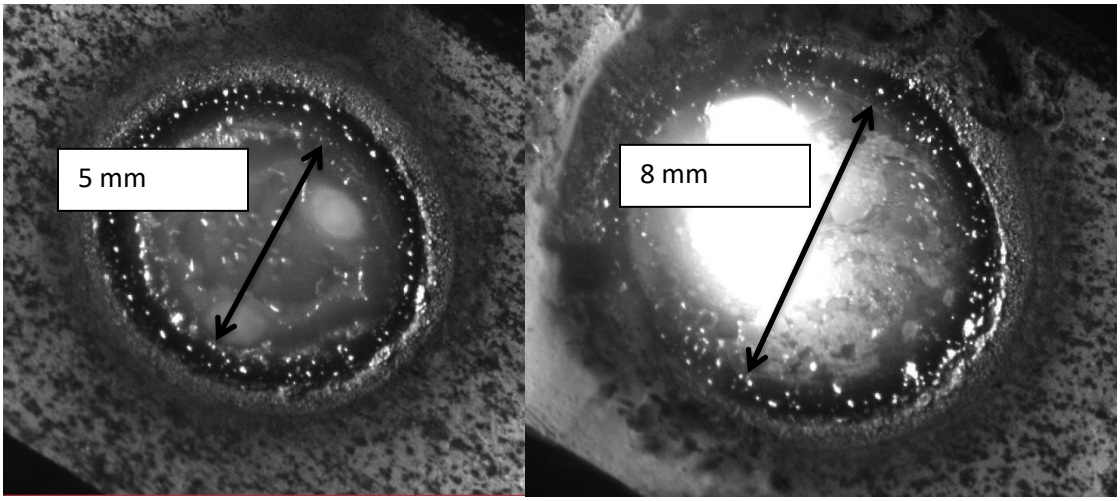

Figure 69 Dimensions of fusion zone TRIP 700 welded at (a) 700 W (b) 1100 W

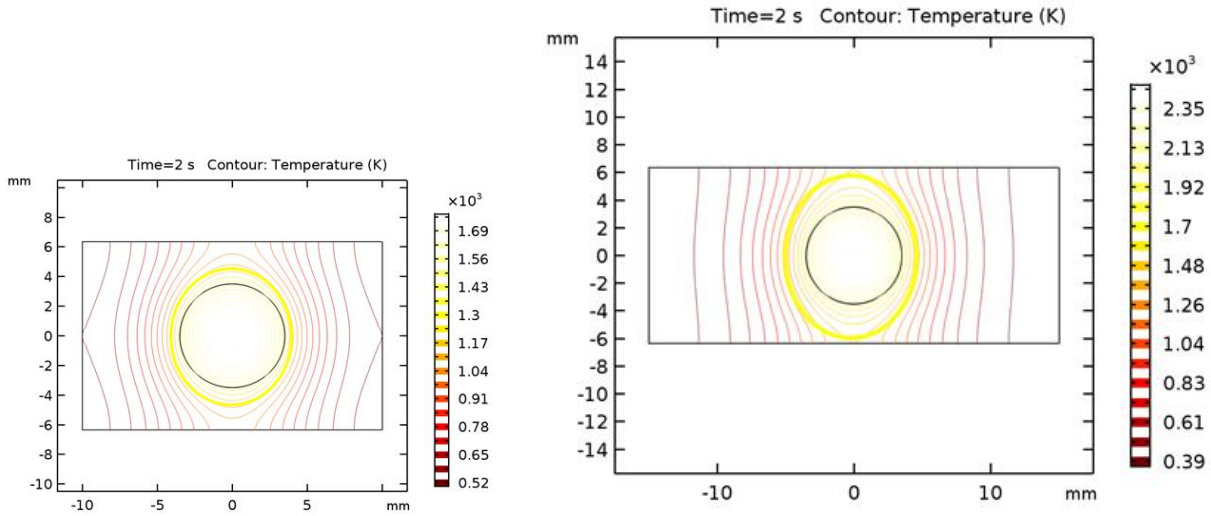

Figure 70 Finite element contour recordings at top surface (a) DP 1000 (b) TRIP 700

To identify the flow route of molten liquid in and along the weld pool, marangoni effect is considered [45]. The Marangoni effect is the mass transfer along an interface between two fluids due to a gradient of the surface tension. In the absence of a surface-active agent, the surface tension (γ_A) of the liquid metal decreases with increasing temperature (T_A), $\partial\gamma / \partial T < 0$

as shown in figure 71 a. The liquid metal with a lower surface tension at point A is pulled outward by the cooler liquid metal with a higher surface tension at point B. In other words, an outward shear stress is induced at the pool surface by the surface tension gradient along the pool surface. This causes the liquid metal to flow from the centre of the pool surface to the edge and return below the pool surface, as shown in figure 71 b . Surface-tension-driven convection is also called thermo-capillary convection or Marangoni flow [44].The presence of surface-active elements such as sulfur and oxygen in the steel weld pools has an impact on the magnitude and direction of convection [44]. If surface-active elements are not present in the weld pool, the dγ/dT term is negative, and liquid metal flows outwards from the heat source along the surface of the weld pool [45]. Outward flow from the heat source causes the weld pool to become wider [45]. If high concentrations of surface-active elements are present in the weld pool, the dγ/dT term may become positive depending on the local temperature and the concentration of the surface active element, thereby reversing the local direction of liquid metal flow [45]. Higher heat input will induce higher effect of oxygen as a surface driving agent and possible flow of molten pool with a positive surface tension gradient as seen in figure 71 b.

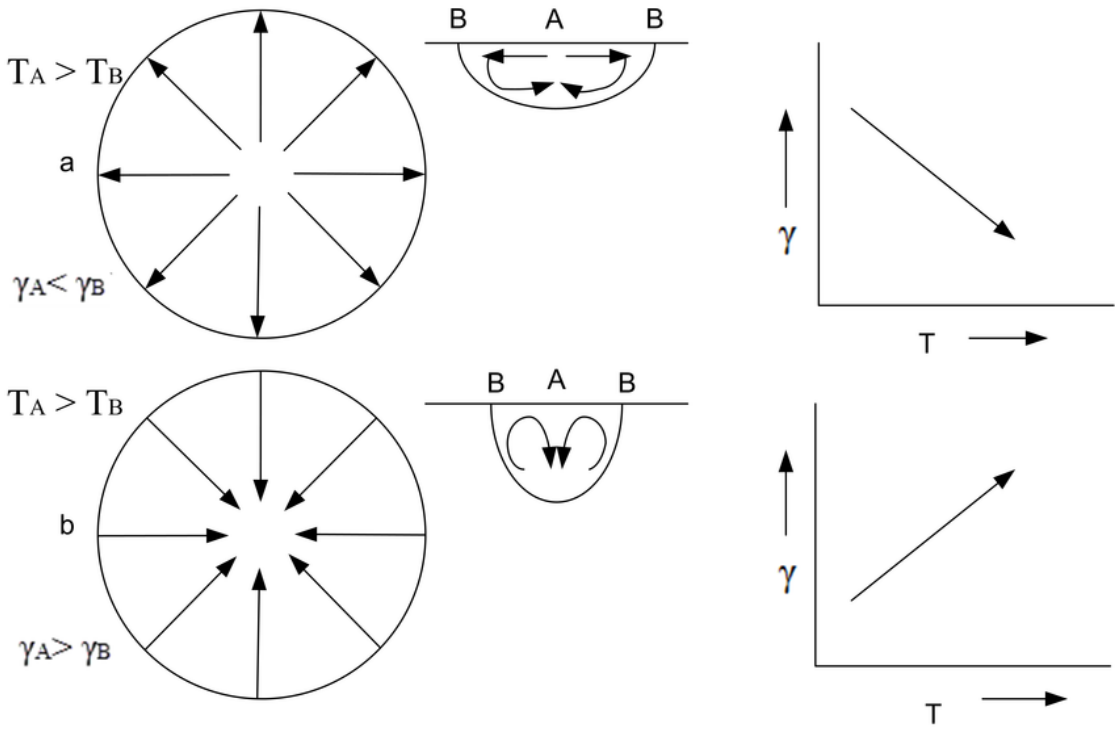

Figure 71 Schematic representation of Marangoni fluid flow in welds [45]

Fluid flow was not considered during finite element analysis. However, from the experimental results, the dimensions of the top and bottom surfaces were obtained. These spot sizes give an idea about the volume of the weld pool. The difference in the dimensions of the spot of top and bottom surface was more in TRIP steel as compared to DP steel. Therefore, it is possible that DP steel had narrower weld pools as represented in figure 71 b (+ve surface tension gradient) while TRIP steel have wider weld pools as seen in figure 71 a (-ve surface tension gradient).

5.1.2. Microstructure

As the next step, the etched samples were studied to understand the microstructural evolution. Figure 72 b represents a DP steel microstructure from the cross-sectioned weld pool. In DP steel welds, the microstructure in the base metal basically consists of evenly distributed body centre tetragonal (bct) martensite within the body centre cubic (bcc)-ferrite phase [46]. The fusion zone of the weld pool is fully martensitic (figure 72 b). The change in the microstructure constituents is also reflected in the hardness measurements data. The martensite structure allows the weld metal and HAZ near the weld metal to have the maximum hardness, and the decrease in the hardness of HAZ near the base metal results from relatively soft ferrite having low hardness [46].

The constituents containing martensite and ferrite in the HAZ were finer than in either of the base metal or the fusion zone. The resulting high density of grain boundaries constitutes obstacles in the formation of nearly complete martensite. The martensite constitutes of very thin regions of retained austenite between interdendritic region [45]. The higher manganese contents in DP1000 also result in a higher hardenability [46]. The amount of martensite formation also depends on cooling rate of the welds. The cooling rate for DP steel welded at laser power of 1000 W was predicted from finite element model as 40°C/s. Higher heat input leads to a slower cooling rate which results in the coarse grains in weld metal. At a high heat input of 1000 W, coarse grained HAZ was observed as seen in figure 40 a and 73.

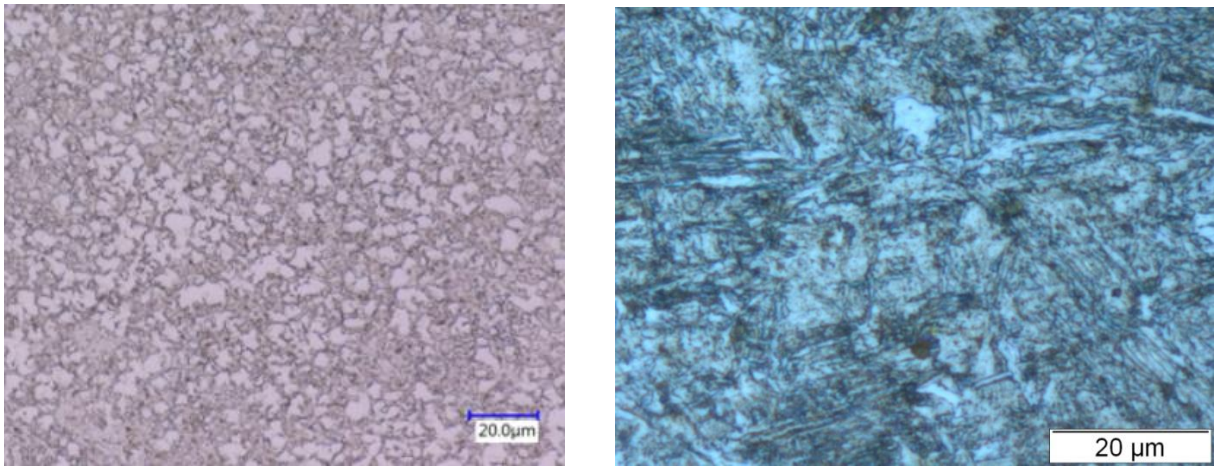

Figure 72 (a) Base metal of DP 1000 (b) Fusion zone in DP 1000 weld (1000 W, 300 kg)

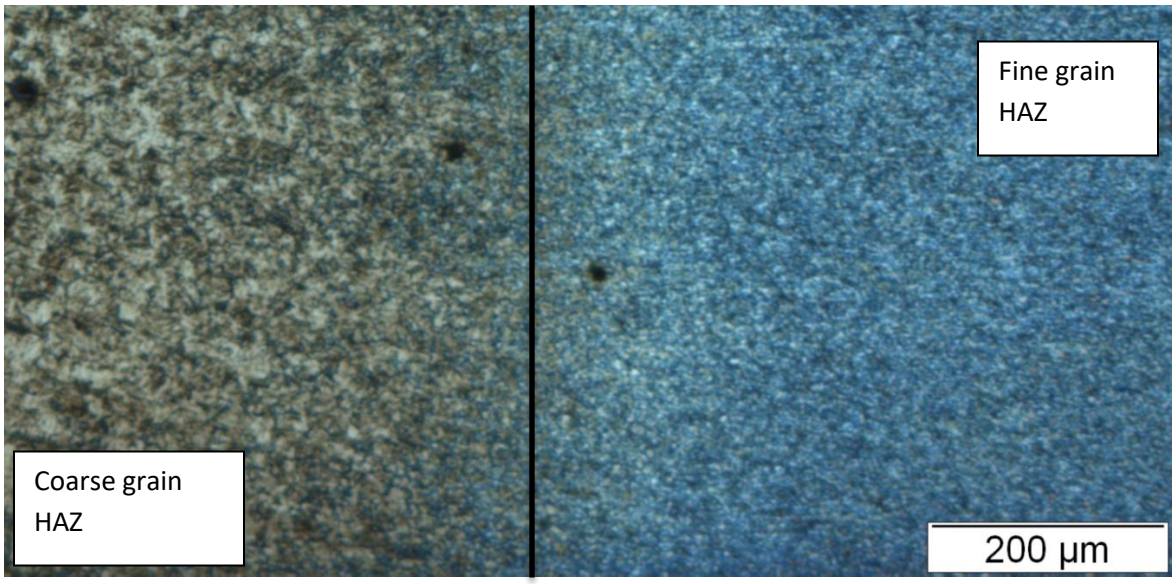

Figure 73 Coarse grain and Fine grain HAZ in DP 1000 (1000 W, 300 kg)

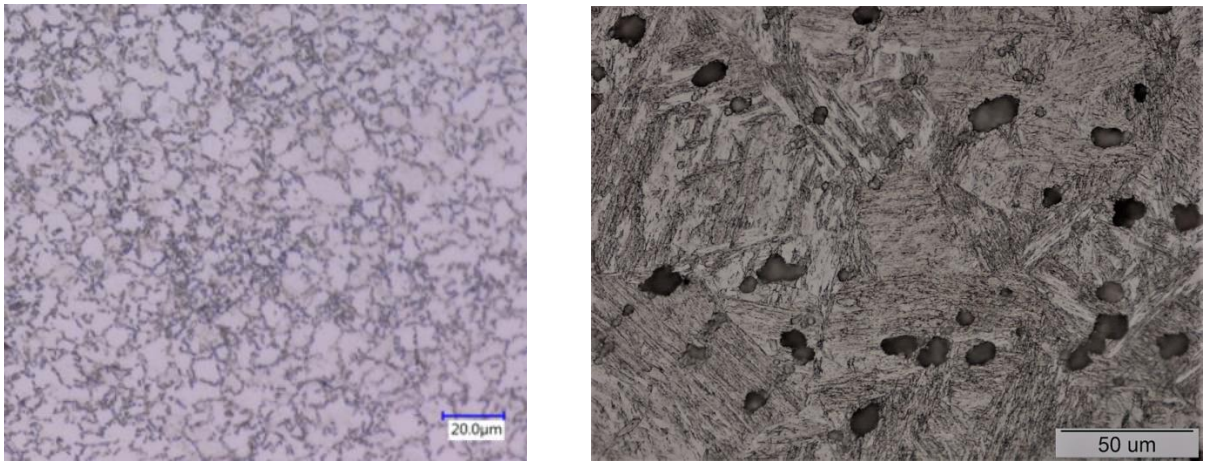

Figure 74 Fusion zone in TRIP 700 (1000 W, 300 kg)

The fusion zone microstructure of TRIP steel as seen in figure 74 consists of ferrite, martensite and retained austenite due to the high aluminum content [47]. Researchers studied the microstructural evolution during welding of aluminum-based TRIP steels and showed that alltriomorphic ferrite was found at the fusion line and grain boundaries of 1.1% Al- TRIP steel welds. It is well known that Al is a strong ferrite stabilizer and promotes high temperatures ferrite as the primary phase in the solidification process [47].

The fusion zone shows the presence of inclusions, mainly randomly distributed and also some times in a clustered manner. The fusion zone showed the presence of inclusions, mainly with a random distribution and in some places decorating the grain boundaries. The optical microscopy investigations of this study show that these inclusions are generally found at the grain boundaries. The observation of inclusions in the fusion zone of low alloyed steel welds is not new. Extensive research had been performed in the past to study the formation mechanism of inclusions, their effects on subsequent phase transformations, and the final mechanical properties of the welds [47] [48]. In order to achieve required mechanical properties, the TRIP and DP steels contain alloying elements. Carbon, manganese and silicon contents are similar for these two steels as shown in table 2. However, the TRIP steel has a higher content of phosphorus and aluminium 9 and 36 times more than the DP steel respectively. Phosphorus is added to increase the amount of austenite retained at room temperature. Aluminium is insoluble in cementite and is added to retard its formation. The presence of strong deoxidizers such as silicon and aluminum in high amounts, as in the case of the TRIP steels, leads to the formation of oxide inclusions in the liquid metal. It is also known that the reaction between the dissolved alloying elements in the weld pool with the available oxygen, nitrogen, and carbon forms nonmetallic inclusions [37].

Figure 75 shows the presence of a solidification microstructure in the samples. These microstructures, in turn, influence the mechanical, physical, and chemical behaviours of the material. The solidification starts with the heterogeneous nucleation of the austenite grains at the fusion zone as all the welded samples are fully austenitic after 2s of welding. Following the solidification, prior austenite grains based on their position relative to the weld centre and the local constitutional cooling showed sub-grain microstructure as mentioned in section 2.11. As the solid columnar grains grow inward, a closed semi-solid region is formed when the dendritic tips coalesce at the weld centre. Alloying elements such as manganese remain dissolved in the liquid state, whilst silicon and aluminium partition to the solid phase.

During solidification, solute is partitioned between the solid and liquid to either enrich or deplete interdendritic regions. This naturally leads to variations in composition on the scale of micrometres, i.e., to micro-segregation [48]. Due to fluid flow phenomena in the liquid steel and inter-dendritic space of the mushy zone, a part of the enriched liquid is washed from the inter-dendritic zone into the bulk liquid [48]. By those phenomena the bulk liquid is incrementally enriched with alloying elements. At complete solidification this leads to an enriched centre of the weld and thus the directional solidification.

This increased amount of phosphorus and aluminium in the TRIP steel leads to a broader solidification range than the DP steel. Previous studies have shown the segregation of phosphorus in both the steels when the dendritic tips reach the weld centre. TRIP steel showed a much higher concentration of phosphorus at the grain boundaries than DP steel making the TRIP steel more sensitive for cracking [37].

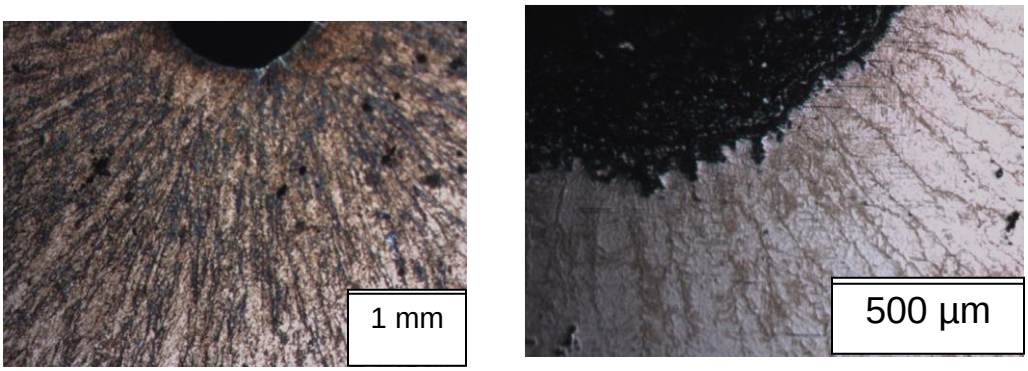

Figure 75 Columnar grain solidification in TRIP (left) and DP(right) steel welded at 1000 W towards the centre of the weld from the cross sectioned samples. The bold black region denotes the vaporised craters in each of the sample.

5.2. Variation in applied global load

Figure 76 represents the variation in the applied load of 300 kg for the entire welding cycle for DP steel welded at a laser power of 1000 W. As the welding starts, there is a drop in the load to a minimum value (in this case 36.6 kg), as the weld pool fully melts after 2s. Material surrounding the weld pool is heating up and therefore, leading to thermal expansion. This fact could also be attributed from the finite element model of DP steel (figure 76 b) designed for the same welding parameter (1000 W, 300 kg) where the temperature profile represents the area of the weld pool which was fully austenite after 2s.

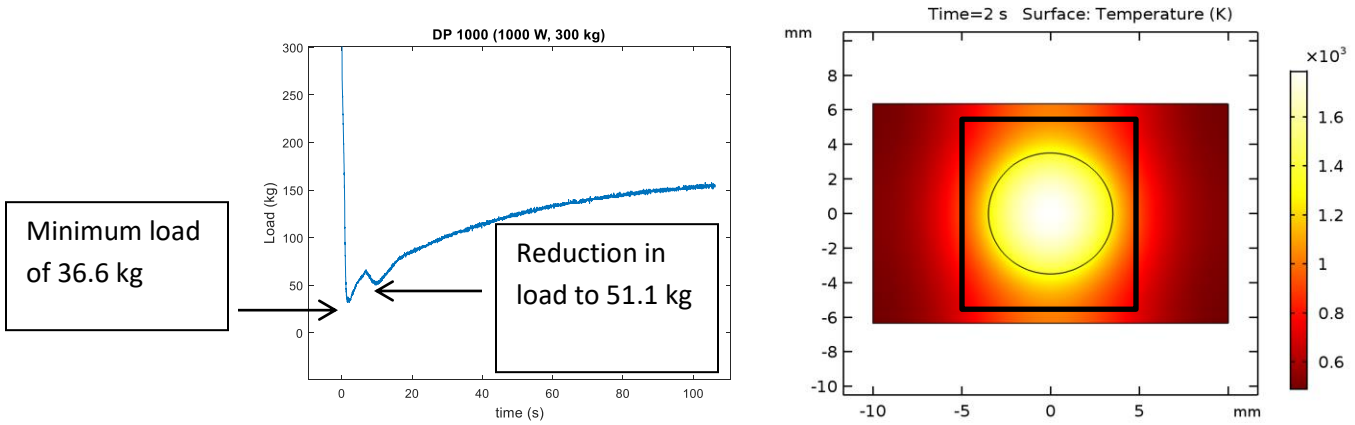

Figure 76 (a) Load cycle in DP1000 (1000 W, 300 kg) (b) Finite Element model welded at 1000 W

From figure 77, it was assumed that the area of the sample on the top surface that was fully austenite after 2s of welding was the area denoted by rectangle enclosing the weld pool on top surface. That area was further assumed to be a side of a cuboid representing part of the sample which contains fusion zone and part of the heat affected zone (HAZ) as shown in figure 77 a.

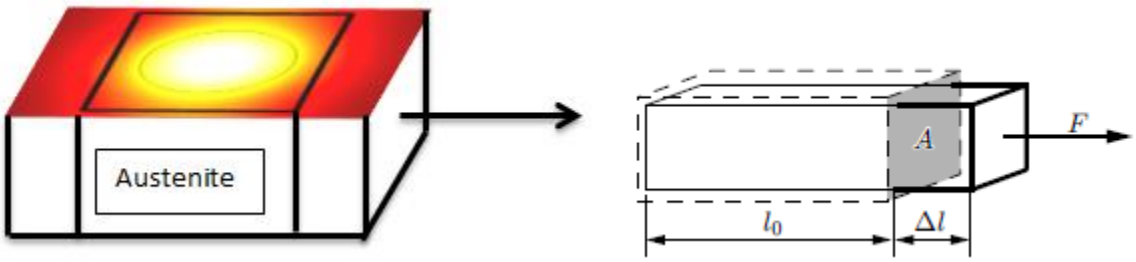

Figure 77 (a) FE model depicting austenite region in DP1000 (b) Schematic representation of application of normal stress

Stress can be distinguished by the relative orientation of the force and the area. Force acting upon the area producing normal stress on the region which was welded will exhibit variation in the overall global load, i.e., reduction due to volumetric expansion during heating and volumetric contraction during cooling of the weld pool. Figure 77 b schematically represent the application of load and change in dimension of the sample. The changes in the dimensions (strain measurements) were obtained directly from DIC measurements.

Figure 78 represents the CCT (continuous cooling transformation) diagram for DP 1000 at 0.15 % of carbon indicating the austenite region (above 850°C). After the laser is switched off, the load value starts increasing and then there is a further sharp reduction (till 51.1 kg) for a time period dt of 2.8 s as mentioned in section 4.3 with a further increase due to cooling and volumetric contraction. This phenomenon was only observed in all the welds of DP steel.

Cooling rate for DP steel was estimated in the centre of the weld from the finite element model at approx. 40°C/s. CCT diagram as seen in figure 78, represents the cooling curve depicting the way all the austenite will transform after complete cooling. It shows that the weld pool can finally be complete martensite after cooling. However, the variation in the global load shows again a reduction as mentioned in figure. This could be attributed to possible phase transformations before the formation of complete martensite. The global load decreases when the weld has entered α+α’ (ferrite and martensite) region right after martensite start temperature (M_S). The temperature extracted at this time instant of 11.88 s was approximately 718.8°C at the weld centre at a time of 11.88s as seen in figure 44.

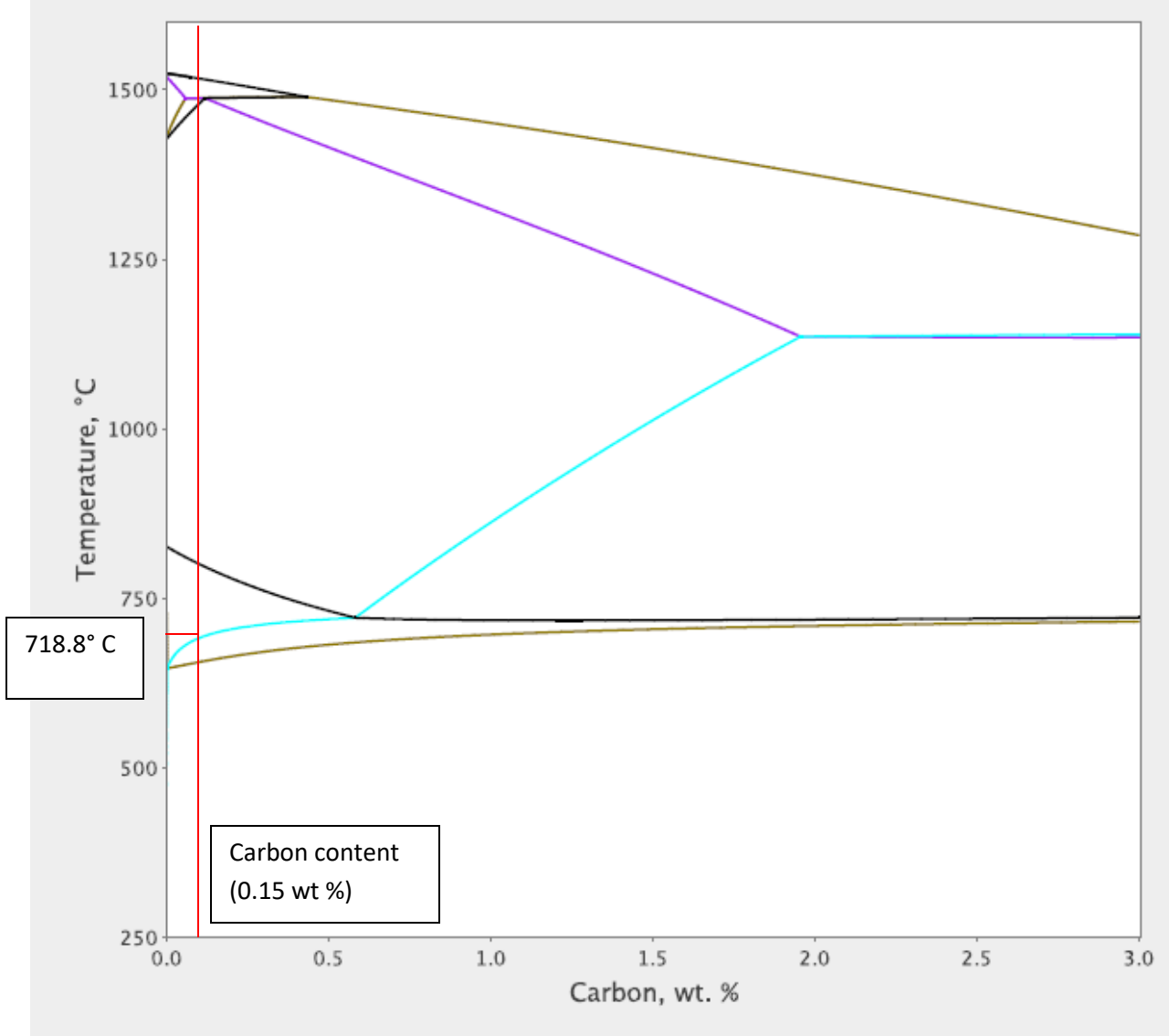

Figure 78 Continuous cooling transformation diagram for DP1000 steel

This decrease in load can be explained by decrease in volume during to cooling/contraction accompanying the martensite transformation [39].The hard phase martensite in DP steel has a high strength and low ductility. By contrast, the soft phase (retained austenite) has low yield strength (σ_y) and high ductility (ε_U). When the composite microstructure is stressed, the plastic strain is at first focussed in the more ductile soft phase. Eventually, the harder phase also deforms plastically. This composite deformation behaviour leads to intermediate combinations of yield strength (σ_y). The DP microstructure thus exploits the high strength of the hard phase, and the high ductility of the soft phase.

During the cooling stage, volume change due to the austenite to martensite transformation results in plastic deformation. Retained austenite is normally present together with martensite and is a much softer phase. Krauss has argued that it is plasticity within the austenite that occurs at low strains and stresses [48]. This has the effect of postponing further deformation and resulting in higher stresses in the remaining untransformed austenite, which will in turn also transform. The fact that the plastic strain is at first focused in the soft phase is advantageous (subsequently leading to reduction in applied tensile stress) since the hard phase can reserve its ductility until the later stages of overall deformation.

Similarly, variation in load for TRIP steel for spot weld made with a laser power of 1000 W and an applied load of 300 kg. The time where the slope of plot changes during contraction is. At that time instant, the temperature during cooling obtained from finite element model was 950.4° C. From CCT diagram, it is evident that the weld has obtained martensite start temperature and is in the region of retained austenite and martensite (α+γ) as shown in figure 79. Cooling rate was extracted from finite element model for TRIP steel as an approx. value of 55°C/s. Possible reason obtained from the analysis is that the amount of the phases present after martensite start temperature effect the extent to which load will reduce (indicating the strength of the welded sample). Therefore sharp reduction in load was observed for DP steel and not in TRIP steel

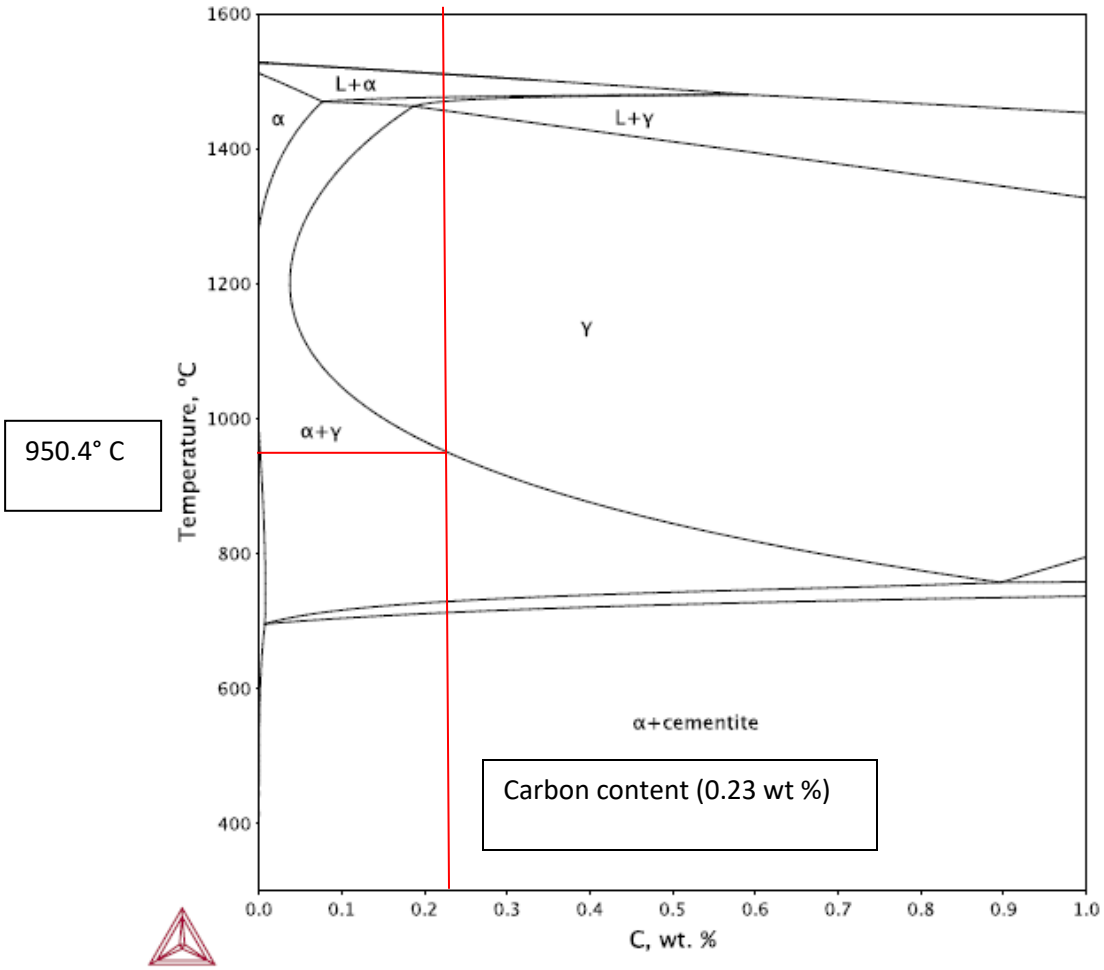

Figure 79 Continuous cooling transformation diagram for TRIP 700 steel

5.3. Solidification cracking behaviour

5.3.1. Transverse strain measurement

For mechanical analysis of the weld pool, the elastic stress–strain relationship of the material could be established by using isotropic Hooke's law. The plastic behaviour of the material could be described by Von Mises principle and isotropic hardening rule. The total strain increment can be expressed as the sum of increments due to elastic (ε^E), plastic (ε^P) (external load facilitates in reaching the plastic range) and thermal loading (ε^T), respectively, in the equation

$$\Delta\varepsilon = \Delta\varepsilon^E + \Delta\varepsilon^P + \Delta\varepsilon^T \quad (7)$$

Molten pool is generally deemed as the condition without stress/strain due to the stress release in liquid metal. Solidification shrinkage has a significant influence on the evolution of stress/strain fields near the molten pool [37]. Generally, rapid cooling rate in laser welding will produce larger undercooling. However, no additional cooling parameter was used in any of the experiments.

To investigate the solidification cracking behaviour, a cracking criterion or indicator, which reflects the driving force of solidification cracking initiation and propagation, is needed to identify. Up to date, parameters such as mechanical strain, plastic strain and plastic strain rate have been used to analyse the cracking behaviour. For this report, mechanical strain has been chosen as the criteria as mentioned in section 3.7. Figure 80 represent the mechanical transverse strain in cracked samples of TRIP and DP steel respectively. Figure 81 represent the transverse strains obtained at different locations. The anomaly in the measurements of transverse strains at different locations has already been mentioned in chapter 4.

Figure shows the change in mean transverse strain in the one of the cracked sample indicating a peak strain of 1.12 % at the cooling stage for TRIP steel at laser power of 1000 W and applied load of 600 kg. The strain does not vary much with time and is approximately in the range between 0.9-1.1 % in the cooling stage. For the cracked sample of DP steel, the observed peak strain was 0.91 % (figure 82).

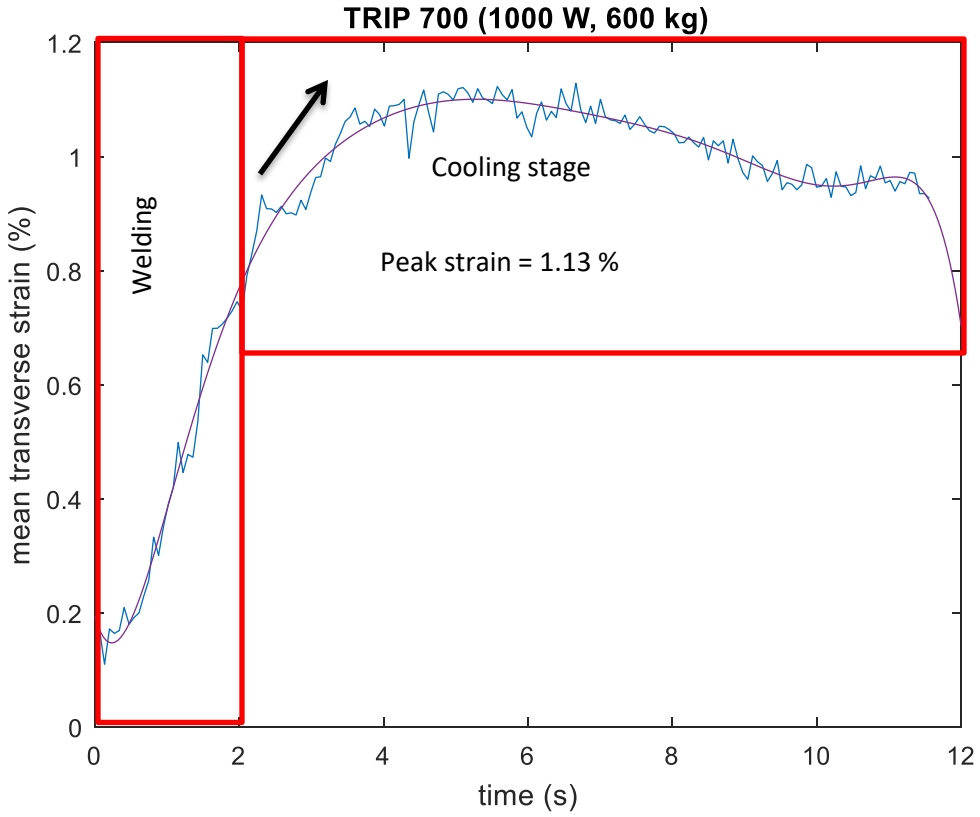

Figure 80 Mean transverse strain as the function of time near fusion boundary for TRIP 700 (1000 W, 600 kg)

Conventionally, the maximum strain for both TRIP and DP steel should have been observed at 2s where the welding stops after complete heating. However, in both the steels, where cracks were observed, the samples strained more during the cooling stage exhibiting maximum strains. This result could be attributed to the fact that there was an initiation of the crack and the further increase in strain is due to the crack growth for a certain period of time. Once the crack growth stops, no further increase in the transverse strain was observed. The strain measurements (now local strains) showed similar trends at different locations for TRIP and DP steel, although, with different peak strain. Therefore, mean strain value was considered for final quantification for rest of the welds.

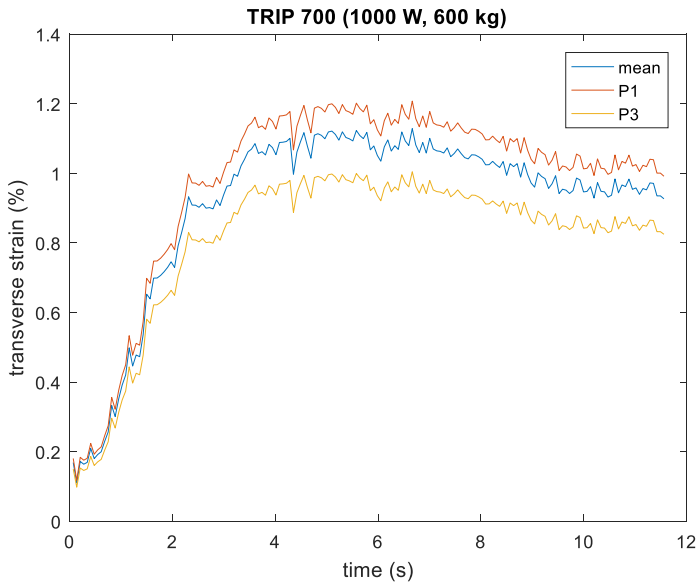

Figure 81 Local transverse strain at P1, P3 and mean boundary line as the function of time near fusion boundary for TRIP 700 (1000 W, 600 kg)

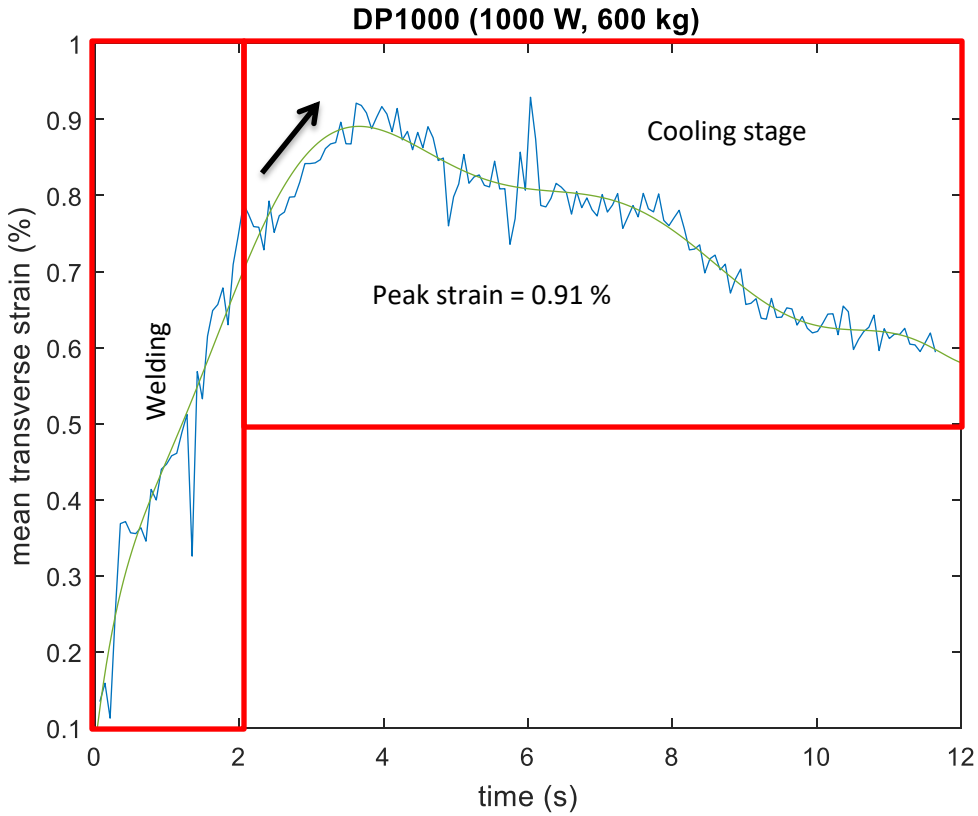

Figure 82 Mean transverse strain as the function of time near fusion boundary for DP 1000 (1000 W, 600 kg)

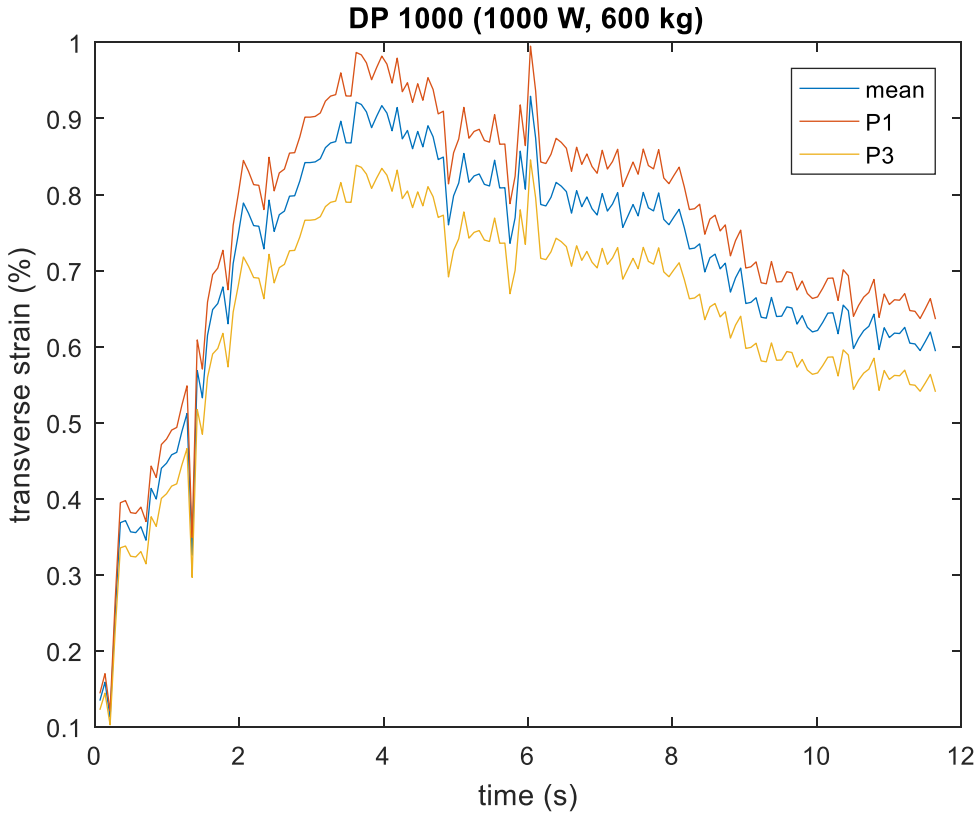

Figure 82 Local transverse strain at P1, P3 and mean boundary line as the function of time near fusion boundary for DP 1000 (1000 W, 600 kg)

Migayi et. al studied the possible cracking behaviour in spot welds [48]. Figure 83 shows the schematic representation for solidification and crack formation inside the vaporised surface of the spot weld. It also shows the schematic representation of the solidification process. The grain grew towards the center of the spot weld, which led to the formation of the columnar grain. In this study columnar grains were observed for the spot welds made. Figure 83 b shows the final solidified spot weld with possible equiaxed grains in the crater. It was mentioned by the author that at the terminal stage of the solidification process, the nucleation speed of crystal in the center of the spot weld was higher than the growth speed of the columnar grain, which led to the possibility of equiaxed grain in the center. Figure 83 c shows the crack at the initial stage. During the cooling process, molten films owing to microscopic segregation were produced at the grain boundaries inside the welded part, which made the boundaries the

weakest position in the spot weld. The spot weld zone had a trend to shrink during the cooling process, which would induced inner stresses in the spot weld zone. As a result, hot cracks propagated from inside the welded part to surface following the solidification process. Figure 83 d shows the final status of the cracked spot weld. Under the action of the stress, the crack propagated along the grain boundaries.

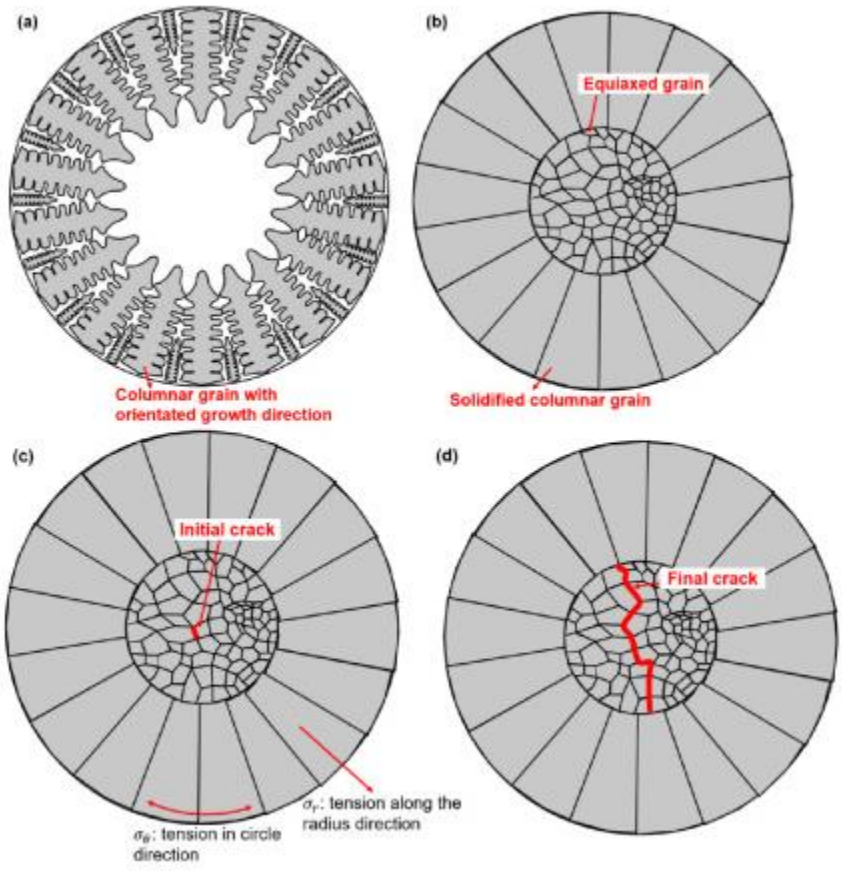

Figure 83 Schematic representation of solidification and crack formation in spot welds []

5.3.2. Brittle temperature range

Cracking occurs in brittle temperature range (BTR) where the columnar grains and liquid film coexist and the strength of grain boundaries is so weak that a small mechanical load may rupture the liquid film. Generally, the coherency point is deemed as the starting point of BTR where the dendrites arms begin to connect with each other and the thermal strain begins to form. The temperature at which the samples no longer exhibit any reduction of area and first grain boundary fusion occurs is referred to as nil ductility temperature (NDT). For the cooling phase, the temperature at which ductility is measurable again starts below NDT. This temperature is referred to as ductility recovery temperature (DRT).

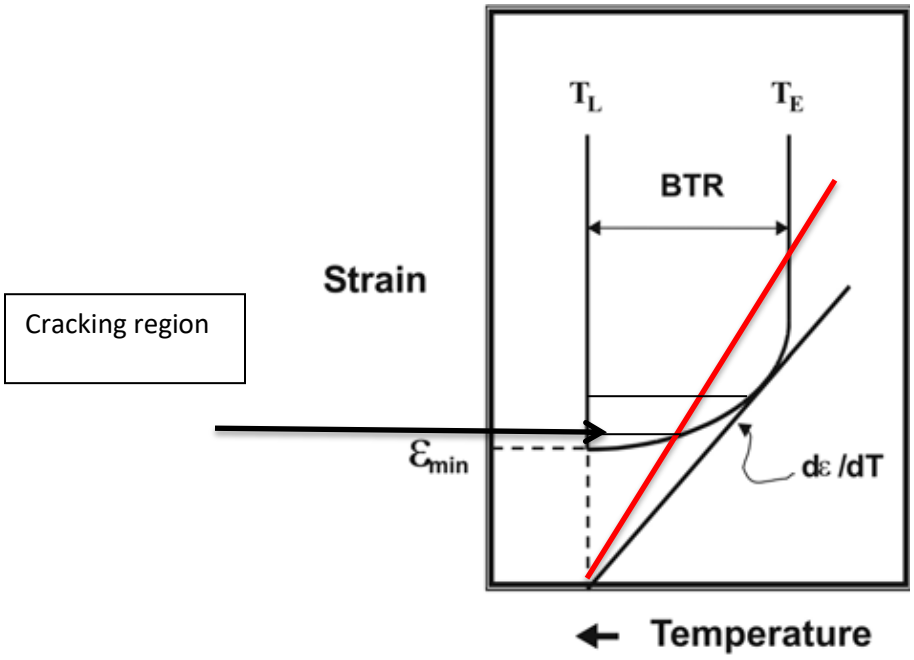

Figure 84 Schematic representation of Brittle Temperature range. Ductility recovery temperature (DRT) is denoted as T_E and Nil Strength temperature (NST) by T_L [50]

There are two key factors that can be used to instantaneously assess the general susceptibility of a material, i.e., the minimum strain required to initiate cracking, ε_{min} and a critical strain rate for temperature drop (slope of the tangent to the ductility curve) as shown in figure 84. Generally, the smaller the critical strain rate, the higher the susceptibility to solidification cracking. As an example the slope line showed in red intersects the ductility curve inside the BTR region and therefore, would be susceptible to hot cracking. At higher minimum strain

(ε_{min}), BTR would be larger and thus, the hot cracking susceptibility also increases. During experimentation, first cracks observed at the lowest possible value of strain were 0.91 % and 0.83 % for DP and TRIP steel respectively, however, these could not be treated as minimum strain value to initiate cracks as mentioned in section 4.5.

Consequently, a material can be characterized in terms of the width of its critical temperature interval (BTR) in conjunction with the minimum strain in the BTR (temperature dependant mechanical property). It becomes apparent that the determination of this temperature interval alone is generally not sufficient for characterizing the hot cracking resistance of a material. Therefore, the history and the absolute level of minimum strain need to be included in the BTR for hot cracking justification.

In conclusion, BTR plays an important role in the solidification cracking behavior. The transverse mechanical strain is always tensile, which tears the centre of the weld pool if material in the BTR is large enough. However, based on Prokhorov's theory, it is recommended to additionally qualify the minimum strain in the BTR in order to ensure comparability of the hot cracking criteria of different hot cracking procedures. This requires further development or modification, respectively, of testing techniques for hot cracking assessment.

As major influencing variables for hot cracking, especially under conditions of external stressing, the weld pool near direction-dependent minimum deformations and deformation rates need to be determined. With the help of such hot cracking criterion, it might in the future be possible to indicate a critical threshold value of parameters such as strain. It should be largely independent of other quantities, below which hot cracking does definitely not occur and which characterizes a material or a component quantitatively with respect to its hot cracking susceptibility.

Conclusion

Laser Spot welding experiments were conducted on advanced high strength steels namely, DP and TRIP steel. Based on thermo-mechanical aspects, theoretical background was used to justify the hot cracking behaviour. It was observed that application of tensile load had a significant effect on the cracking susceptibility. TRIP steel showed higher cracking susceptibility even though detection of crack macroscopically was challenging. DP steel was relatively resistant for low tensile loads. Overall, a good series of results were determined from the macroscopical, microscopical and in-situ transverse strain measurements.

Various factors are known that encourage or prevent hot cracking, it is normally not possible even with defined welding conditions to draw immediate conclusions about the hot cracking resistance of a material alone from a metallurgical composition. The causes of hot cracking can ultimately be attributed to the occurrence of metallurgical effects and to structural loads. Hot cracking is assessed mostly by drawing on empirical quantities, as, for example, on the total crack length or on the total number of cracks. In this context, it has however not been investigated yet to what extent the real differences in the hot cracking behavior of different materials can actually be measured with the help of such hot cracking parameters. Particularly in regard of increasing component safety requirements, empirical hot cracking parameters may, in certain circumstances, turn out to be insufficient.

In order to assure transferability of hot cracking tests to component welds, it is necessary to consider design-specific variables influencing hot cracking. Following aspects were the learning parameters throughout the project

- Quantitative analysis of the critical strain rate und of the ductility in the BTR
- Metallographic, analytical, and process-dynamic analyses of the weld pool geometry and of crystallization characteristics as a function of heat input
- FEM-simulation of the solidification front and of the dendrite growth direction
- Establishment of a reference base for hot cracking criteria from various externally loaded hot cracking tests
- Comparison of comparable evaluation parameters of hot cracking theories and deduction of verifiable comparison criteria
- Deduction of testing concepts incorporating the influence of welding process parameters and of process quantities into the hot cracking criterion
- Analyses of the influence of solidification morphologies (weld metal and BTR (mushy zone)) on the hot cracking susceptibility taking account of process-dynamic influencing variables as a function of heat input and other welding constraints

- Analyses of the complex influences exerted by the solidification morphology in the BTR (mushy zone) considering defined loading directions and weld pool shapes (function of the welding parameters)

The following major goals can be deduced for hot cracking test procedures

- Defined loading conditions
- Defined welding parameters
- Test parameter variation and experimental analysis of crack critical deformations and deformation rates
- Repeatability
- High sensitivity
- Qualitative transferability for materials classification
- Component transferability by assessment of weld pool near local strains and strain rates (in combination with numerical analyses).

Bibliography

1. High Growth Areas in Industrial Laser Processing & Monitoring, Laser Editorials, Brandon Kallooon, Craig Bratt & Rahul Patwa, November 14th, 2017.
2. https://www.gestamp.com/what-we-do/technologies/welding/laser-welded-blanks
3. Hall, J. Auto/Steel Partnership. (2011, May). Evolution of Advanced High Strength Steels in Automotive Applications [PowerPoint presentation at Great Designs in Steel]
4. Kim, C. H., Choi, J. K., Kang, M. J., & Park, Y. D. (2010). A study on the CO2 laser welding characteristics of high strength steel up to 1500 MPa for automotive applications. Journal of Achievement in Materials Manufacturing Engineering.
5. World Auto Steel. (2009). Advanced high strength steels application guidelines
6. Santillan Esquivel, A., Nayak, S. S., Xia, M. S., & Zhou, Y. (2012). Microstructure, hardness and tensile properties of fusion zone in laser welding of advanced high strength steels. Canadian Metallurgical Quarterly.
7. Kuziak R, Kawalla R, Waengler S, et al. Advanced high strength steels for automotive industry: a review. Arch Civ Mech Eng. 2008
8. Xia, M., Sreenivasan, N., Lawson, S., Zhou, Y., & Tian, Z. (2007). A comparative study of formability of diode laser welds in DP980 and HSLA steels.
9. Xia, M., Tian, Z., Zhao, L., & Zhou, Y. N. (2008b). Metallurgical and mechanical properties of fusion zones of TRIP steels in laser welding
10. Xu, W., Westerbaan, D., Nayak, S. S., Chen, D. L., Goodwin, F., & Zhou, Y. (2013). Tensile and fatigue properties of fiber laser welded high strength low alloy and DP980 dual-phase steel joints. Materials and Design
11. Böttger, B., et al., Relationship between solidification microstructure and hot cracking susceptibility for continuous casting of low-carbon and high-strength low-alloyed steels: A phase-field study. Metallurgical and Materials Transactions A, 2013.
12. Korojy, B., A Fredriksson, Hot crack formation during peritectic reaction in steels. J Ironmaking & steelmaking, 2010.
13. Prokhorov NN, Shirshov YV. Effect of welding conditions on character of crack-propagation and load carrying capacity of a welded joint during brittle-fracture of weld metal.Weld Prod . 1974
14. Shankar, V., Criteria for hot cracking evaluation in austenitic stainless steel welds using longitudinal varestraint and transvarestraint tests
15. Easterling, K., Introduction to the physical metallurgy of welding. 2nd ed. ed. 1992, Oxford: Butterworth-Heinemann Ltd.
16. Mathier, V., Coalescence of equiaxed grains during solidification. Modelling and Simulation in Materials Science and Engineering 2004

17. Kou, S., Fluid flow and solidification in welding: Three decades of fundametnal research at the University of Wisconsin. Supplement to the welding journal, 2012:
18. D. E. Swift-Hook and A. E. F. Gick: Weld. J., 1973, 52
19. W. Guo and A. Kar: Sci. Technol. Weld. Joining, 2000
20. Rossini M, Spena PR, Cortese L, et al. Investigation on dissimilar laser welding of advanced high strength steel sheets for the automotive industry. Mater Sci Eng A Struct. 2015
21. Yan F, Liu S, Hu C, et al. Liquation cracking behavior and control in the heat affected zone of GH909 alloy during Nd: YAG laser welding. J Mater Proc Technol. 2017
22. Rappaz M, Drezet JM, Gremaud M, et al. A new hot tearing criterion. Metall Mater Trans A. 1999
23. Pellini, W., Strain theory of hot tearing. Foundry, 1952. 80(11)
24. Borland, J., Generalized theory of super-solidus cracking in welds (and castings). British Welding Journal, 1960. 7(8)
25. Prokhorov, N., The technological strength of metals while crystallizing during welding. Welding Production, 1962. 9(4)
26. Matsuda, F., H. Nakagawa, and K. Sorada, Dynamic observation of solidification and solidification cracking during welding with optical microscope. Trans. JWRI, 1982. 11(2)
27. Pumphrey, W. and P. Jennings, A consideration of the nature of brittleness at temperatures above the solidus in castings and welds in aluminum alloys. J. Inst. Metals, 1948
28. Wang XJ, Lu FG, Wang H-P, et al. Micro-scale model based study of solidification cracking formation mechanism in Al fiber laser welds. J Mater Proc Techn 2016
29. Bleck W., Papaefthymiou S., Frehn A.: Microstructure and Tensile Properties of Dual Phase and TRIP Steels, Steel Reasearch. int., Vol. 75, No. 11, 2004
30. Agarwal G, Gao H, Amirthalingam M, et al. In situ strain investigation during laser welding using digital image correlation and finite-element-based numerical simulation. Sci Technol Weld Join. 2017
31. Gao H, Hermans MJM, Richardson IM, et al. Simulation of transient force and strain during thermal mechanical testing relevant to the HAZ in multi-pass welds. Sci Technol Weld Join. 2013
32. Drezet J-M, Allehaux D. Application of the rappaz drezet- gremaud hot tearing criterion to welding of aluminium alloys. In: Böllinghaus T, Herold H, Cross CE, Lippold JC, editors. Hot cracking phenomena in welds
33. Matlock, D. K. and Speer, J. G. (2010). “Processing Opportunities for New Advanced High-Strength Sheet Steels” Materials and Manufacturing Processes, 25 (1-3)
34. ULSAB-AVC Body Structure Materials, Technical Transfer Dispatch No. 6, May, 2001.

35. Lanzillotto C.A.N and Pickering F.B.: Structure-Property Relationships in Dual-Phase Steels, Met. Sci., Vol. 16, 1982
36. Korzekwa D.A., Lawson R.D., Matlock D.K., Krauss G.: A consideration of Models Describing the Strength and Ductility of Dual-Phase Steels, Scripta Metallurgica, Vol. 14, 1980
37. H. Gao, G. Agarwal, M. Amirthalingam & M. J. M. Hermans (2017): Hot cracking investigation during laser welding of high-strength steels with multi-scale modeling approach, Science and Technology of Welding and Joining
38. Chang P.H., Preban A.G.: The Effect of Ferrite Grain Size and Martensite Volume Fraction on the Tensile properties of Dual Phase Steel, Acta Metall., Vol. 33, No. 5, 1985
39. Bag A., Ray K.K.: Influence of Martensite Content and Morphology on Tensile and Impact Properties of High-Martensite Dual Phase Steels, Metall. Mat. Trans., Vol. 30A, 1999
40. Zackay V.F., Parker E.R, Fahr D., Bush R.: The Enhancement of Ductility in High-Strength Steels, Trans. Am. Soc. Met., Vol. 60, 1967
41. Bleck W., Phiu-On K.: Microalloying of Cold-Formable Multi Phase Steel Grades, Mat. Sc. Forum, Vols. 500–501, 2005
42. KIJAC, J.: High-temperature Processes of Steel Production. Emilena Košice 2006.
43. GEDEONOVÁ, Z.—JELČ, I.: Metallurgy of Cast iron.Košice, HF TU 2000
44. ŠMRHA, L.: Solidification and Crystallization of Steel Ingots. Praha, SNTL 1983.
45. ROESER, W. M.—WENSEL, H. T.: Journal of Research of the National Bureau of Standards, 26, 1941,
46. MYSLIVEC, T.: Physico-chemical Principles of Steel making. Praha, SNTL 1971.
47. A review of the effects of chemical and phase segregation on the mechanical behaviour of multi-phase steels
48. N. Blundell, J. Biffin, T. Johnson and C. Page, 1999, Proc. 5th International Conference (1998) – Trends in Welding Research. Ed. J.M. Vitek, S.A. David, J.A. Johnson, H.B. Smartt, T. DebRoy. Printed 1999 by ASM International
49. Rosenthal: Mathematical theory of heat distribution during welding and cutting, Welding Journal, 20(5), 1941
50. Brittleness temperature range of Fe-Al alloy J. Adamiec, M. Kalka Department of Materials Science, Silesian University of Technology, ul. Krasińskiego 8b, Katowice 40-019, Poland